

Jasper Rieser · Felix Endress ·
Alexander Horoschenkoff ·
Philipp Höfer · Tobias Dickhut ·
Markus Zimmermann *Editors*

Proceedings of the Munich Symposium on Lightweight Design 2022

Tagungsband zum Münchner
Leichtbauseminar 2022

Proceedings of the Munich Symposium on Lightweight Design 2022

Jasper Rieser · Felix Endress
Alexander Horoschenkoff · Philipp Höfer
Tobias Dickhut · Markus Zimmermann
Editors

Proceedings of the Munich Symposium on Lightweight Design 2022

Tagungsband zum Münchner
Leichtbauseminar 2022

Editors

Jasper Rieser 
TUM School of Engineering and Design
Laboratory for Product Development
and Lightweight Design
Technical University of Munich
Garching, Germany

Felix Endress 
TUM School of Engineering and Design
Laboratory for Product Development
and Lightweight Design
Technical University of Munich
Garching, Germany

Alexander Horoschenkoff
Munich University of Applied Sciences
München, Germany

Philipp Höfer
Universität der Bundeswehr München
Neubiberg, Germany

Tobias Dickhut
Universität der Bundeswehr München
Neubiberg, Germany

Markus Zimmermann
TUM School of Engineering and Design
Laboratory for Product Development
and Lightweight Design
Technical University of Munich
Garching, Germany

ISBN 978-3-031-33757-4 ISBN 978-3-031-33758-1 (eBook)

<https://doi.org/10.1007/978-3-031-33758-1>

© The Editor(s) (if applicable) and The Author(s), under exclusive license to Springer Nature Switzerland AG 2023

This work is subject to copyright. All rights are solely and exclusively licensed by the Publisher, whether the whole or part of the material is concerned, specifically the rights of translation, reprinting, reuse of illustrations, recitation, broadcasting, reproduction on microfilms or in any other physical way, and transmission or information storage and retrieval, electronic adaptation, computer software, or by similar or dissimilar methodology now known or hereafter developed.

The use of general descriptive names, registered names, trademarks, service marks, etc. in this publication does not imply, even in the absence of a specific statement, that such names are exempt from the relevant protective laws and regulations and therefore free for general use.

The publisher, the authors, and the editors are safe to assume that the advice and information in this book are believed to be true and accurate at the date of publication. Neither the publisher nor the authors or the editors give a warranty, expressed or implied, with respect to the material contained herein or for any errors or omissions that may have been made. The publisher remains neutral with regard to jurisdictional claims in published maps and institutional affiliations.

This Springer Vieweg imprint is published by the registered company Springer Nature Switzerland AG
The registered company address is: Gewerbestrasse 11, 6330 Cham, Switzerland

Preface

Dear reader,

We are happy that the third edition of the conference proceedings of the Munich Symposium on Lightweight Design is now published. Our conference developed into a melting pot of innovative applications and cutting-edge research on lightweight design and optimization within the last few years. To sustainably impact progress in lightweight design, contributions made their way into these proceedings.

A valuable exchange between industry and research has characterized the series of Symposia throughout the last years. To discuss the newest technologies, such as additive manufacturing and various optimization approaches, research institutes and companies of all sizes attended the Symposium in 2022.

We thank all the authors and presenters for their exciting contributions. Also, we thank the team of our publisher Springer for their cooperation and excellent support throughout the publication process.

June 2023

Best regards
Jasper Rieser
Felix Endress
Alexander Horoschenkoff
Philipp Höfer
Tobias Dickhut
Markus Zimmermann

Contents

Design and Investigation of a Thermoelastic Actuator with Tailored Unidirectional Thermal Expansion and Stiffness using Mechanical Metamaterials and Joule Heating Activation	1
<i>Erhard Buchmann, Isabel Prestes, Bruno Musil, and Philipp Höfer</i>	
Additive Manufacturing of Continuous Fiber-Reinforced Composites	15
<i>Anna Judenmann, Philipp Höfer, Jens Holtmannspötter, and Ingo Ehrlich</i>	
Insect Wing Inspired Design and Manufacturing of Multifunctional Automotive Applications Using Stereolithography and Subsequent Short Carbon Fiber Reinforcement.	28
<i>Felix Mesarosch, Tristan Schlotthauer, Peter Middendorf, Frieder Fink, Fabian Kopp, and Jan-Philipp Fuhr</i>	
Comparison of Different Material Systems for Filament Winding Based on the Split-Disk Experiment and Setup of a Digital Twin	40
<i>Ruben Krischler, Markus Blandl, Maike Kliewe, Stefan Carosella, and Peter Middendorf</i>	
Digital Approaches for Optimization of Composite Processing: Bayesian Optimization for Impregnation and Fibre Spreading In-Situ Monitoring	51
<i>Florian Schönl, Fabian Hübner, Marius Luik, Jeremias Thomas, Rodrigo de Albuquerque, and Holger Ruckdäschel</i>	
3D Material Characterization and Determination of Out-Of-Plane Properties Based on Digital Image Correlation	68
<i>Nikolas Korte, Jens Bold, Alexander Hüls, Sascha Ort, Bernd Westerhoff, Bruno Musil, and Philipp Höfer</i>	
Influence of Plasma Coating Pretreatment on the Adhesion of Thermoplastics to Metals	85
<i>Wikentij Koshukow, Alexander Liebsch, Jan Wippermann, Björn Kolbe, Robert Kupfer, Juliane Troschitz, Magnus Buske, Gerson Meschut, and Maik Gude</i>	
Differential Evolution Based Optimisation of Multi-layered Space Radiation Shielding for Satellite Electronics	97
<i>Nico Gerster and Tobias Dickhut</i>	

Integrating Geometric Metamodel-Assisted Process Assurance into Topology Optimization of Low-Pressure Die Castings 109
Tobias Rosnitschek, Maximilian Erber, Christoph Hartmann, Bettina Alber-Laukant, Wolfram Volk, and Stephan Tremmel

CAD Reconstruction of Watertight Surface Meshes Using Polycube Parameterization and Subdivision Surfaces 120
Moustafa Alsayed Ahmad, Majid Hojjat, and Kai-Uwe Bletzinger

Optimization of Lightweight Vehicle Components for Crashworthiness Using Solution Spaces 134
Ying Lin, Paolo Ascia and Fabian Duddeck

Author Index 145

The Editors

Every year, the **Technical University of Munich, the Universität der Bundeswehr München, and the University of Applied Sciences in Munich** invite researchers and practitioners to join the **Munich Symposium on Lightweight Design**. Experts from industry and academia discuss design tools, applications, and new developments. Topics include, e.g., composite structures, SHM, microstructures, material modelling, design for additive manufacturing, numerical optimization and in particular topology optimization in aerospace, automotive and other industries. The talks are summarized in short articles and presented in this volume.

Jasper Rieser's research is about topology optimization methods with a particular focus on the design for additive manufacturing. Currently, he is a research associate at the Laboratory for Product Development and Lightweight Design at the Technical University of Munich (TUM) from which he also obtained his bachelor's and master's degree in mechanical engineering.

Felix Endress is a research associate at the Laboratory for Product Development and Lightweight Design at the Technical University of Munich (TUM). He investigates product development approaches for metal additive manufacturing, with a special focus on optimization and validation of aerospace structures. Previously, he conducted research in the field of Engineering Design at the University of Cambridge and Friedrich-Alexander-Universität Erlangen-Nürnberg. He holds master's degrees in Mechanical Engineering and Engineering Management.

Alexander Horoschenkoff studied mechanical engineering at TUM and received his PhD from the mechanical engineering department. He started his career at the research center of Messerschmitt-Bölkow-Blohm (MBB) in Ottobrunn. Within the research core team of the DaimlerChrysler AG he was responsible for the mechanical technology field. Since 2001 he has been a professor at the Munich University of Applied Sciences, Department of Mechanical Engineering, Automotive and Aeronautics Engineering and head of the CC "Smart Composites".

Philipp Höfer is a full professor at the Institute of Lightweight Engineering within the Department of Aerospace Engineering at the Universität der Bundeswehr München. After obtaining his PhD in the field of material modelling and continuum mechanics, he has gained extensive experience in the development of aircraft structures at Airbus over many years. His research interests include the conceptual, functional and structural design of lightweight structures and the investigation of their static and dynamic characteristics by analysis and test.

Tobias Dickhut is a full professor of Composite Materials and Technical Mechanics at the Institute of Aeronautical Engineering within the Department of Mechanical Engineering at the Universität der Bundeswehr München. After obtaining his PhD in the field of lightweight construction and structures with fibre-reinforced plastics, he has gained extensive experience in the development of space structures at MT Aerospace over many years. His research interests include the scientific engineering research and design with composites, in particular the issues of lightweight (hybrid) force transmission into highly stressed structural components made of composite materials and the development of tank structures for cryogenic media.

Markus Zimmermann's research is about the design and optimization of complex mechanical systems, such as automobiles or robots. Before he became a professor at TUM, he spent 12 years at BMW designing vehicles for crash and vehicle dynamics. His academic training is in Mechanical Engineering with degrees from the Technical University of Berlin (Diplom), the University of Michigan (M.S.E.) and MIT (Ph.D.).



Design and Investigation of a Thermoelastic Actuator with Tailored Unidirectional Thermal Expansion and Stiffness using Mechanical Metamaterials and Joule Heating Activation

Erhard Buchmann¹(✉), Isabel Prestes², Bruno Musil¹, and Philipp Höfer¹

¹ Universität der Bundeswehr München, Institute of Lightweight Engineering, Neubiberg, Germany

{erhard.buchmann,bruno.musil,philipp.hoefer}@unibw.de

² Universität der Bundeswehr München, Institute of Materials Science, Neubiberg, Germany

isabel.prestes@unibw.de

Abstract. Mechanical metamaterials have become an emerging research field due to the advances in additive manufacturing technology in the last decade. Especially, materials with adjustable coefficient of thermal expansion (CTE)—thermoelastic metamaterials—are investigated because of their wide range of engineering applications. They span from the shape control of space structures to micro positioning systems. For designing the CTE of metamaterials, at least two materials with different CTEs have to be combined in complex lattice structures, which makes manufacturing difficult up to now. However, with the advent of multi-material additive manufacturing such metamaterials become available. Extensive research examined topological designs of passive thermoelastic unit cells. Regarding topological concepts for applications as actuator, mainly only homogeneous temperature differences and mechanical forces as activation have been addressed. However, the activation through joule heating is addressed rarely. In this work, the design of a bi-metallic thermoelastic actuator based on mechanical metamaterials with joule heating activation is presented. First, an efficient parameterization for the underlying triangular metamaterial cell with double-coned legs inspired by pentamode metamaterials is presented. The cell design concept is investigated using finite element method regarding stiffness and CTE as well as their coupling and the influence of the double cone shape of the legs. Second, two principal design options for the accommodation of foil heaters on the actuator cell are compared. By using a transient simulation of an actuator consisting of a tessellation of the designed cells, the thermoelastic functionality could be shown.

Keywords: Metamaterial · Smart materials · Thermal Expansion · Additive Manufacturing · Multi-Material · Actuator · Thermoelasticity

1 Introduction

Most of the natural materials expand with the rise of temperature and shrink by decreasing it, which characterizes them as materials with positive coefficient of thermal expansion (CTE). In contrast, near-zero CTEs and even negative CTEs are intrinsic properties of few materials for specific temperature ranges [1–3]. Also, these materials generally have a limited mechanical performance, which limits their engineering applications [2, 4].

These limitations of natural negative CTE materials can be overcome with mechanical metamaterials. Mechanical metamaterials show a rationally architected micro structure that results in a desired macroscopic behavior [5]. This includes auxetic metamaterials that present a negative Poisson’s ratio, pentamode metamaterials where arbitrary anisotropic stiffnesses can be obtained and thermoelastic metamaterials where a tunable CTE can be reached [2, 6–9]. Thermoelastic metamaterials with controllable CTE have been investigated for over 20 years [10, 11]. Structures with high unidirectional CTE are desired for actuators controlled by temperature, while structures with zero, minimal or even negative CTE are intended especially for applications that either involve high temperature variations or require high dimensional accuracy, or both [4, 12, 13]. Applications reach from high-precision spaceborne optical systems to microchip devices [4, 14–17]. For the sake of achieving these properties, these microstructures must have specific geometries and must be composed of at least two different materials with a CTE difference among them [18]. With the advent of metallic multi-material additive manufacturing they become available for structural applications [19–22].

Recent studies focus on the one hand on metamaterials that present a controllable CTE and yet are structurally efficient [12, 13, 23–27]. On the other hand, stimuli-responsive thermoelastic metamaterials called actuators [28], active metamaterials [29] and 4D thermomechanical metamaterials [30] are investigated. The underlying metamaterial ground structures usually work with flexure joints instead of applying structurally efficient double-cone struts of pentamode metamaterials [31–33]. Moreover, besides an activation via heating the whole actuator [24, 28, 31, 32, 34], only limited studies consider a local activation. In [35] a micro actuator activated by a laser with triangular displacement amplification is investigated. In [36] and [37] additively manufactured actuators that are activated by a standard foil heater are investigated. In the work, the thermoelastic functionality could be shown in simulations and experiments. However, no multi-metamaterial actuators are investigated there.

In this study, the design of a planar bi-metallic thermoelastic actuator cell applying mechanical metamaterials with joule heating activation is presented. For investigation, a parameterized geometry based on a bi-material triangle with double cone legs inspired by pentamode metamaterials is utilized. The parameters’ effect on the stiffness and the CTE as well as their coupling are evaluated. Moreover, two options for the joule heating activation with a standard foil heater that requires a minimal surface area are compared: by thickening the middle strut and by applying an additional out-of-plane accommodation structure.

2 Design of the Thermoelastic Actuator Cell

2.1 Negative Thermal Expansion Mechanism of the Actuator Cell

The negative thermal expansion (NTE) of the unit cells of thermoelastic metamaterials is based on a purposefully designed geometric structure using at least two different materials with a preferably large CTE-difference [18]. These geometric structures can be classified in bending-dominated and stretch-dominated according to the underlying expansion mechanism. In this work, a stretch-dominated structure is applied as it is structurally more efficient compared to a bending-dominated structure and therefore more suitable for engineering applications [38–40]. In Fig. 1, a scheme of the applied triangular deformation mechanism of the used planar unit cell for unidirectional expansion in y -direction is shown. When heated by the temperature ΔT , the thermal elongation in axial direction of the middle strut $a - a_0$ is higher than the elongation of the legs due to its higher CTE. This results in a rotation of the legs by the angle $\varphi_0 - \varphi$. Thus the height of the triangular structure h_0 decreases to h . The resulting elongation in y -direction will be henceforth called the structure's CTE, which is calculated by $CTE = (h_0 - h)/(h_0 \Delta T)$. Besides, the stiffness is defined with respect to a unit force F in y -direction. The CTE and the stiffness of this actuator cell are majorly determined by the edge length a and the angle φ . These properties are highly coupled. For instance, low angles lead to high NTEs and low stiffness in y -direction at the same time. Remarkably, actuators with high positive CTE can be built by reversing the high- and low-CTE material.

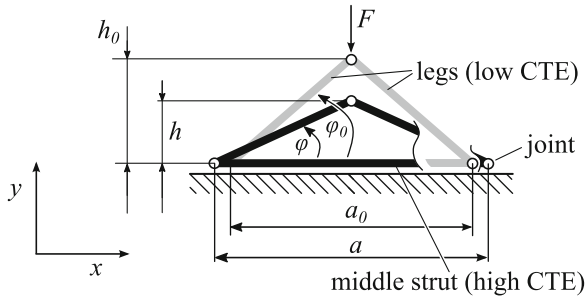


Fig. 1. Scheme of the underlying planar triangular mechanism with idealized rotational joints for a unidirectional negative thermal expansion in y -direction. When heated, the thermal elongation in axial direction of the middle strut $a - a_0$ is higher than the elongation of the legs due to its higher CTE. This leads to a rotation of the legs by the angle $\varphi_0 - \varphi$ resulting in a decrease in height from h_0 to h . The stiffness is defined with respect to a unit force F in y -direction.

2.2 Design Objectives and Parametrization of the Geometry of the Actuator Cell

In this work, a concept for an actuator for engineering applications, especially space applications, is presented. The process of 3D multi-material L-PBF is

particularly suitable to fabricate these structures. However, the metallic multi-material L-PBF is not yet a consolidated process. Consequently, there are some design restrictions and the choice for a simplified design, where no or minimal support structures are required, is convenient. The following design objectives are taken into account here:

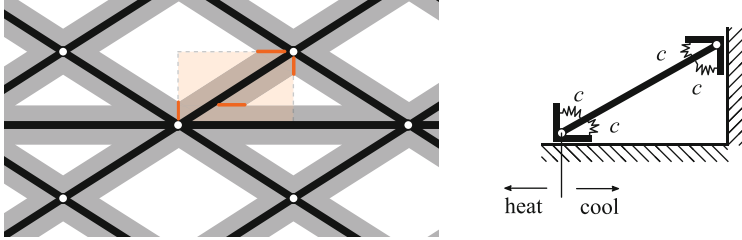
- High Stiffness in y -direction
- High NTE in y -direction
- Joule heating activation with a standard foil heater
- Good manufacturability with bi-material metallic additive manufacturing

When implementing the presented triangular mechanism, a certain wall thickness is required because of stiffness and process requirements. Moreover, in applications actuator cells are usually connected in series for higher NTEs or in parallel for higher stiffnesses. This results in an overlapping of the thicknesses of the struts at the joints as depicted in Fig. 2a. Accordingly, additional rotational stiffness arise (see Fig. 2b). This especially applies for very small angles.

However, the triangular mechanism creating the NTE requires a rotation in the joints. Accordingly, a geometric parametrization with double-coned legs is applied. The smaller thickness at the joints reduces rotational stiffness while in the middle of the strut a high bending resistance preventing buckling of the legs is kept (see Fig. 3) [7–9]. Due to the high complexity with manufacturing structurally more efficient tubular structures are not considered here. The middle strut is not tapered since there the foil heater is attached. The overall thickness t_1 is applied. In order to provide enough space for the accommodation of a foil heater, the middle strut can be thickened (m). For the legs, the thickness t_1 is reached only in the middle of the strut while the ends are tapered. At the ends of the legs, the thicknesses t_2 and $t_2/2$ are applied. The $t_2/2$ -offset at the left corner is important for the avoidance of overlapping of the legs with the middle strut at very small angles. The angle φ is defined from the middle strut middle axis to the leg middle axis.

When considering wall thicknesses, there are two main mechanisms of thermal expansion that counteract when aiming for high NTEs:

- Geometric nonlinear triangular thermal expansion mechanism
- Thermal expansion of the structure in y -direction defined by the geometric expansion in y -direction h_l and h_h .



(a) Tesselation of the actuator cell. Idealized lattice model with rotational pin joints (black). Compliant mechanism considering the wall thickness (grey). Arise of additional rotational stiffnesses (orange) illustrated in a quarter cell (dotted).

(b) Illustration of the arising rotational stiffnesses c when considering the wall thickness using a quarter model.

Fig. 2. Arising rotational stiffness of the actuator cell when taking wall thickness into account.

2.3 Joule Heating Activation

For the joule heating activation, commercially available foil heaters are utilized. This is especially applicable for space application where space-qualified heaters are preferred. Therefore, multi-hierarchically and small-scale structures are not suitable as an activation with standard heaters is difficult. For foil heaters, a minimum space for accommodation is required due to the maximum power intensity (approx. $0.5 \frac{\text{W}}{\text{cm}^2}$ [41]) and the minimum width. Consequently, for the accommodation of the foil heaters the middle strut is preferable over the legs since it is longer. Moreover, activating the middle strut instead of the legs makes the actuator more efficient because it results in a higher temperature in the middle strut than in the legs. This results in a higher decrease in height due to the higher difference in thermal elongation.

For the increase in width two options are investigated here:

- Joule heating activation by thickening the middle strut (see Fig. 4a)
- Joule heating activation with an additional accommodation structure attached to the middle strut (see Figs. 4b and 4c)

In the first option, not only a foil heater could be directly attached to the middle strut, but also a heating cartridge could be accommodated inside it, as depicted in Fig. 4a. However, the thickening of the middle strut leads to lower NTE. Due to its higher and isotropic CTE, the elongation of the middle strut would cause a higher elongation in the y -direction as well. Therefore, an out-of-plane structural enlargement for the accommodation is applied in the second option. Here, an exemplary double cone and a plate are depicted, whereby other geometries could be utilized. The plate is not suitable for low edge lengths.

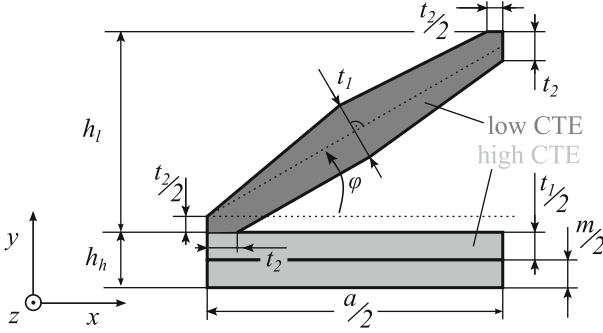
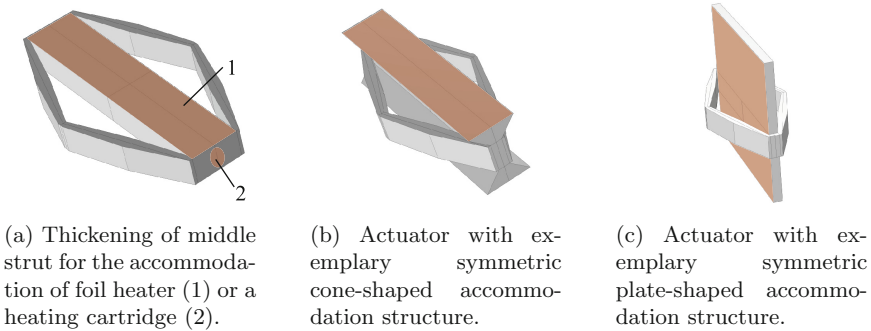


Fig. 3. Quarter model of the parametrization of the geometry with double cone legs and with a thickening of the middle strut (m) for the accommodation of a foil heater.



(a) Thickening of middle strut for the accommodation of foil heater (1) or a heating cartridge (2). (b) Actuator with exemplary symmetric cone-shaped accommodation structure. (c) Actuator with exemplary symmetric plate-shaped accommodation structure.

Fig. 4. Options for the accommodation of a foil heater (orange).

3 Investigation of the CTE and the Stiffness of the Actuator Cell

For the evaluation of the actuator cell, CTE, stiffness and their coupling as well as the efficiency of both joule heating activation options are investigated using finite element method. To this, different sets of parameters were investigated in Sect. 3.1, 3.2, 3.3, 3.4 and 4. An overview of the applied parameter sets and the materials can be found in Tables 1 and 2. Steel was applied as the high CTE material and Invar as the low CTE material. Both are structurally efficient while having a considerably large CTE gap. Moreover, bi-material powder bed fusion is feasible using them because of the good weldability of both materials [42, 43]. All investigations are done under the variation of the angle φ in an interval of $[6^\circ; 60^\circ]$ using a 2.5 mm thick model. First, the influence of the main parameters a , φ and t is studied. Then, the influence of the double cone shape of the legs and the influence of the thickening of the middle strut is investigated.

Table 1. Overview over parameters applied for the investigations.

Section	t_1 [mm]	t_2 [mm]	m [mm]	a [mm]	φ [°]
3.1		[0.5; 1.5]	0	[10; 20]	
3.2	1	[0.5; 1]	0		
3.3	1	1	0	20	[6; 60]
	1	0.5	0		
3.4	1	0.5	[0; 10]		
4	1	0.5	0	20	20
	1	0.5	3		

Table 2. Material parameters and thickness in z -direction.

Parameter	Unit	Steel	Invar
Young's modulus	GPa	200	140
Poisson's ratio	–	0.3	0.3
CTE	$10^{-6}1/K$	18	1
Thermal conductivity	$\frac{W}{m \cdot K}$	15	13.5
Heat capacity	$\frac{J}{kg \cdot K}$	510	515
Density	$\frac{kg}{m^3}$	7900	8100
Thickness in z -direction	mm		2.5

3.1 Influence of the Edge Length a and the Overall Thickness $t_{1,2}$

The influence of the edge length a and the overall thickness under different angles was investigated (see Fig. 5). Both parameters greatly influence the CTE and the stiffness: A higher NTE is generated by lower angles, smaller thicknesses and higher edge lengths (see Fig. 5a). By contrast, a higher stiffness results from higher angles, higher thicknesses and lower edge lengths (see Fig. 5b). Consequently, as a rule of thumb, the stiffness and CTE are of competing interest (see Table 3).

However, regarding the CTE, only for angles smaller than approx. 20° a considerable strong effect for the NTE can be observed. In this course, an increase in thickness reduces this effect.

Regarding the stiffness, there is a decrease for angles greater than approx. 50° due to the activation of bending deformation in the legs. This effect is also stronger for shorter edge lengths and could be hindered by using higher thicknesses in the middle of the legs. However, this effect is not considered any further as the focus of this work is on structures with high NTE that require long edges and small angles.

Table 3. Contradicting influence of the geometric parameters $\varphi, a, t_{1,2}$ on stiffness and NTE.

Design objective	Parameter		
	φ	$t_{1,2}$	a
Stiffness	↑	↑	↓
NTE	↓	↓	↑

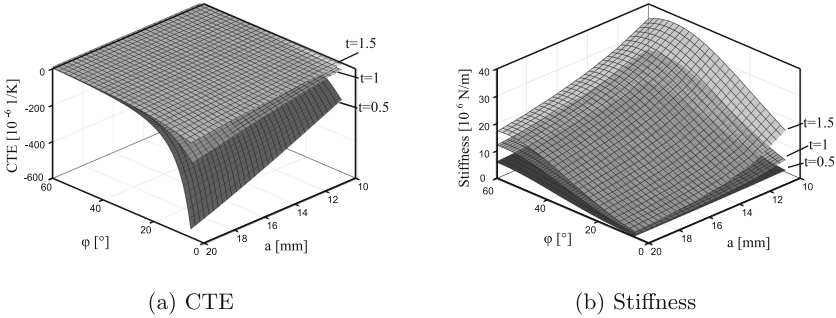


Fig. 5. Influence of the edge length a and the overall thickness t on the stiffness and CTE of the actuator cell under variation of the angle φ .

3.2 Influence of the Double Cone Shape of the Legs

In a second step, the influence of the double cone shape of the legs under different angles was investigated (see Fig. 6). To do this, a reduction of t_2 from 1 mm to 0.5 mm was considered while keeping $t_1 = 1$ mm and $a = 20$ mm. It was observed, that a higher tapering results in a much higher NTE while having a minor effect on the stiffness. This especially applies for smaller angles φ . Consequently, tapering the legs is well suited to improve the actuator geometry when taking the design objectives stiffness and CTE into account at the same time. Due to the definition of the CTE-stiffness-relationship using only two variables, this parametrization is well suited for a fast preliminary design of components with many coupled cells followed by a topology optimization for detailed design.

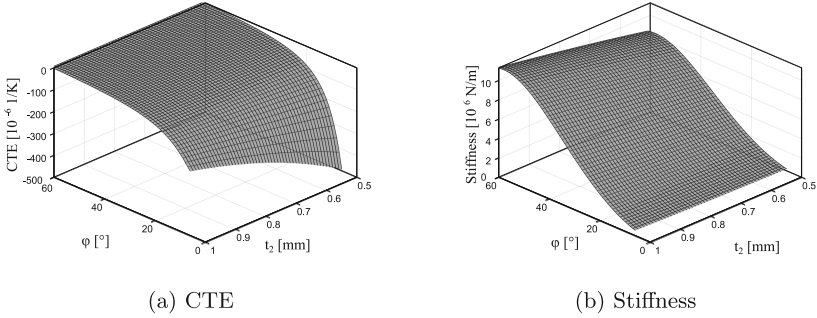


Fig. 6. Influence of the tapering of the legs (defined by t_2) on the stiffness and CTE of the actuator cell under variation of the angle φ . A constant thickness $t_1 = 1$ mm and a constant edge length $a = 20$ mm is applied.

3.3 Comparison of Actuator Cells with Tapered and Non-Tapered Legs

Third, a tapered ($t_2 = 0.5$ mm) and a non-tapered ($t_2 = 1$ mm) actuator cell with a constant edge length $a = 20$ mm and a constant width of $t_1 = 1$ mm were comparatively examined under the variation of the angle φ (see Fig. 7). The influence of the tapering varies under different angles φ : For decreasing angles the effect on the NTE rises while the impact on the stiffness decreases. This is due to the higher overlapping of the legs with the middle strut when considering thicknesses which can be overcome by the tapering (see Fig. 7). Thus, the double cone shape of the legs is beneficial for the actuator design where high NTEs that require low angles and high stiffnesses are to be reached simultaneously. Nevertheless, only pareto-optimal solutions can be achieved in terms of stiffness and NTE. The decrease in stiffness for angles higher than approx. 55° depicted in Fig. 5b can also be seen here.

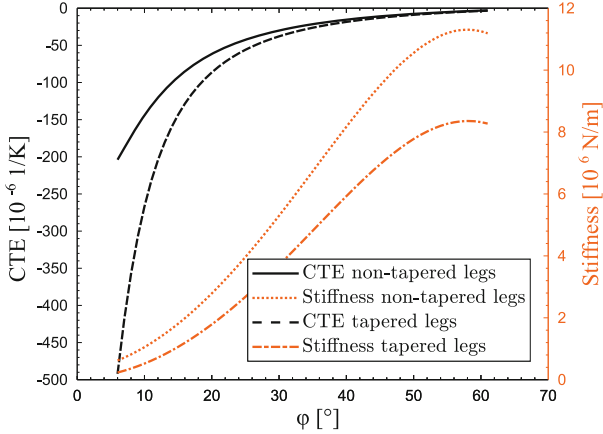


Fig. 7. Comparison of an actuator cell with tapered and non-tapered legs under the variation of the angle φ . A constant thickness $t_1 = 1$ mm and a constant edge length $a = 20$ mm is applied.

3.4 Influence of the Thickening of the Middle Strut on the CTE

Fourth, the influence of thickening of the middle strut (defined by m) on the CTE is investigated (see Fig. 8). To do this, an actuator cell with tapered legs ($t_2 = 0.5$ mm) with a constant edge length $a = 20$ mm and a constant width of $t_1 = 1$ mm was studied under the variation of the angle φ . It can be observed that higher thicknesses of the middle strut result in significantly lower NTEs. This effect is due the higher geometric expansion in y -direction (h_h) resulting in a higher thermal expansion in y -direction which counteracts the triangular expansion mechanism (see Fig. 3). Thus, for example, at an angle $\varphi = 20^\circ$, the actuator cell has a CTE of approx. $-9 \cdot 10^{-6}$ 1/K with no thickening of the middle strut ($m = 0$ mm) while there is a CTE of approx. $-3 \cdot 10^{-6}$ 1/K for $m = 10$ mm. As a consequence, the thickening of the middle strut is only suitable for the joule heating activation when small NTEs are sufficient. However, it is advantageous that no support structures are needed at additive manufacturing using this type of activation.

4 Investigation of the Transient Thermal Expansion Applying Joule Heating Activation

For the investigation of the transient thermal expansion an actuator cell tessellation comparing both joule heating activation options is considered (see Figs. 9a and 9b). By applying a tessellation, a higher overall negative expansion can be achieved. Moreover, by using two rows of cells next to each other, the actuator is stiffer, in particular regarding multiaxial loads. The same size of activation surface with a watt density of $0.5 \frac{W}{cm^2}$ is applied on front- and backside for

both options and the displacement u after 10s is evaluated. The scale of the displacements is in μm -scale for both options which is suitable for spaceborne (see Fig. 9c). However, when applying a double cone as accommodation structure for the foil heater far higher negative displacements can be reached especially at small angles.

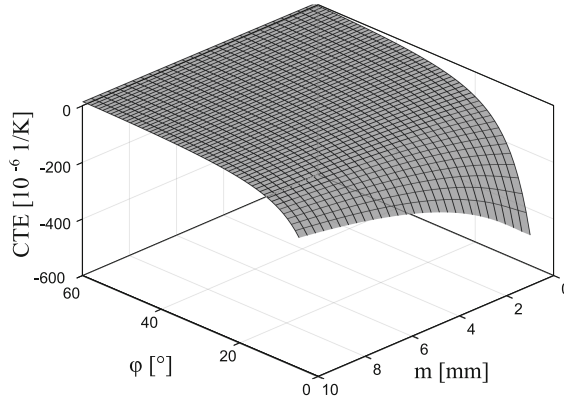
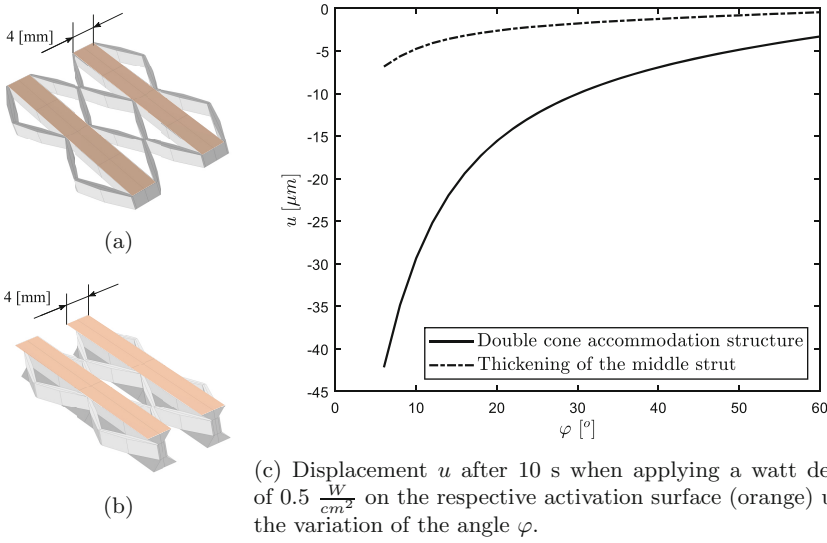


Fig. 8. Influence of the thickening of the middle strut on the CTE under the variation of the angle φ .



(c) Displacement u after 10 s when applying a watt density of $0.5 \frac{\text{W}}{\text{cm}^2}$ on the respective activation surface (orange) under the variation of the angle φ .

Fig. 9. Comparison of the transient thermal expansion of an actuator cell tessellation with joule heating activation using a thickening of the middle strut (9a) and a double cone (9b).

5 Conclusion

In this work, the design of a bi-metallic thermoelastic actuator with negative thermal expansion (NTE) based on mechanical metamaterial with joule heating activation was presented. First, an efficient parametrization of the actuator cell based on a triangular geometry where double-cone-shaped legs can be considered, is presented. The stiffness and CTE were then investigated and it was observed that both are highly coupled, but contradict design objectives regarding the geometric parameters $\varphi, a, t_{1,2}$. This contradiction, however, can be overcome using tapered legs. At the end, two options for the joule heating activation which requires a certain width were investigated: by thickening the middle strut and by applying an out-of-plane structural enlargement. It was shown that the latter is suitable to reach higher negative displacements. On the other hand, the AM of these structures would require support structures. In future work, the thickness at the bi-material interface could be studied taking in consideration the strength of the weld seam. Moreover, the stiffnesses and CTEs in arbitrary directions can be taken into account as design objectives. The presented actuator has a high potential for applications in actively controlled satellite structures [44].

Acknowledgements. This work within the project SeRANIS is funded by dtcc.bw—Digitalization and Technology Research Center of the Bundeswehr which we gratefully acknowledge. dtcc.bw is funded by the European Union—NextGenerationEU.

References

1. Miller, W., Smith, C., Mackenzie, D., Evans, K.: Negative thermal expansion: a review. *J. Mater. Sci.* **44**(20), 5441–5451 (2009)
2. Takenaka, K.: Negative thermal expansion materials: Technological key for control of thermal expansion. *Sci. Technol. Adv. Mater.* (2012)
3. Barrera, G.D., Bruno, J.A.O., Barron, T., Allan, N.: Negative thermal expansion. *J. Phys. Condens. Matter.* **17**(4), R217 (2005)
4. Jefferson, G., Parthasarathy, T.A., Kerans, R.J.: Tailorable thermal expansion hybrid structures. *Int. J. Solids Struct.* **46**(11–12), 2372–2387 (2009)
5. Zadpoor, A.A.: Mechanical meta-materials. *Mater. Horiz.* **3**(5), 371–381 (2016)
6. Joseph, A., Mahesh, V., Harursampath, D.: On the application of additive manufacturing methods for auxetic structures: a review. *Adv. Manuf.* **9**(3), 342–368 (2021)
7. Milton, G.W., Cherkaev, A.: Which elasticity tensors are realizable. *J. Eng. Mater. Technol. Trans. Asme* **117**, 483–493 (1995)
8. Kadic, M., Bückmann, T., Stenger, N., Thiel, M., Wegener, M.: On the practicality of pentamode mechanical metamaterials. *Appl. Phys. Lett.* **100**(19), 191901 (2012)
9. Akbari, M., Mirabolghasemi, A., Bolhassani, M., Akbarzadeh, A., Akbarzadeh, M.: Strut-based cellular to shellular funicular materials. *Adv. Funct. Mater.* **32**(14), 2109725 (2022)
10. Lakes, R.: Cellular solid structures with unbounded thermal expansion. *J. Mater. Sci. Lett.* **15**(6), 475–477 (1996)

11. Sigmund, O., Torquato, S.: Composites with extremal thermal expansion coefficients. *Appl. Phys. Lett.* **69**(21), 3203–3205 (1996)
12. Lakes, R.: Cellular solids with tunable positive or negative thermal expansion of unbounded magnitude. *Appl. Phys. Lett.* **90**(22), 221905 (2007)
13. Lehman, J., Lakes, R.S.: Stiff, strong, zero thermal expansion lattices via material hierarchy. *Compos. Struct.* **107**, 654–663 (2014)
14. Guo, X., Ni, X., Li, J., Zhang, H., Zhang, F., Yu, H., Wu, J., Bai, Y., Lei, H., Huang, Y., et al.: Designing mechanical metamaterials with kirigami-inspired, hierarchical constructions for giant positive and negative thermal expansion. *Adv. Mater.* **33**(3), 2004919 (2021)
15. Li, X., Gao, L., Zhou, W., Wang, Y., Lu, Y.: Novel 2d metamaterials with negative poisson's ratio and negative thermal expansion. *Extreme Mech. Lett.* **30**, 100498 (2019)
16. Lim, T.C.: Negative thermal expansion structures constructed from positive thermal expansion trusses. *J. Mater. Sci.* **47**(1), 368–373 (2012)
17. Raminhos, J., Borges, J., Velinho, A.: Development of polymeric anepctic meshes: Auxetic metamaterials with negative thermal expansion. *Smart Mater. Struct.* **28**(4), 045010 (2019)
18. Kalamkarov, A.L., Kolpakov, A.G.: Analysis, design and optimization of composite structures, vol. 1. Wiley, New York (1997)
19. Anstaett, C., Seidel, C., Reinhart, G.: Fabrication of 3d multi-material parts using laser-based powder bed fusion. In: 2017 International Solid Freeform Fabrication Symposium. University of Texas at Austin (2017)
20. Girth, S., Koopmann, J., Klawitter, G., Waldt, N., Niendorf, T.: 3d hybrid-material processing in selective laser melting: Implementation of a selective coating system. *Prog. Addit. Manuf.* **4**(4), 399–409 (2019)
21. Schneck, M., Horn, M., Schmitt, M., Seidel, C., Schlick, G., Reinhart, G.: Review on additive hybrid-and multi-material-manufacturing of metals by powder bed fusion: State of technology and development potential. *Progress in Additive Manufacturing* pp. 1–14 (2021)
22. Neirinck, B., Li, X., Hick, M.: Powder deposition systems used in powder bed-based multimetal additive manufacturing. *Acc. Mater. Res.* **2**(6), 387–393 (2021)
23. Ai, L.: Micro-architected Metamaterials: Design and Analysis. Ph.D. thesis, Southern Methodist University (2017)
24. Wei, K., Chen, H., Pei, Y., Fang, D.: Planar lattices with tailorable coefficient of thermal expansion and high stiffness based on dual-material triangle unit. *J. Mech. Phys. Solids* **86**, 173–191 (2016)
25. Xu, H., Pasini, D.: Structurally efficient three-dimensional metamaterials with controllable thermal expansion. *Sci. Rep.* **6**(1), 1–8 (2016)
26. Li, J., Liu, H.T., Zhang, Z.Y.: Stiffness characteristics for bi-directional tunable thermal expansion metamaterial based on bi-material triangular unit. *Int. J. Mech. Sci.* **241**, 107983 (2023)
27. Xu, M., Zhao, Z., Wang, P., Zhang, Y., Guo, X., Lei, H., Fang, D.: Planar bi-metallic lattice with tailorable coefficient of thermal expansion. *Acta Mech. Sinica* **38**(7), 1–9 (2022)
28. Sigmund, O.: Design of multiphysics actuators using topology optimization-part ii: Two-material structures. *Comput. Methods Appl. Mech. Eng.* **190**(49–50), 6605–6627 (2001)
29. Qi, J., Chen, Z., Jiang, P., Hu, W., Wang, Y., Zhao, Z., Cao, X., Zhang, S., Tao, R., Li, Y., et al.: Recent progress in active mechanical metamaterials and construction principles. *Adv. Sci.* **9**(1), 2102662 (2022)

30. Ji, Q., Moughames, J., Chen, X., Fang, G., Huaroto, J.J., Laude, V., Martínez, J.A.I., Ulliac, G., Clévy, C., Lutz, P., et al.: 4d thermomechanical metamaterials for soft microrobotics. *Commun. Mater.* **2**(1), 1–6 (2021)
31. Taniker, S., Celli, P., Pasini, D., Hofmann, D., Daraio, C.: Temperature-induced shape morphing of bi-metallic structures. *Int. J. Solids Struct.* **190**, 22–32 (2020)
32. Xu, H., Farag, A., Ma, R., Pasini, D.: Thermally actuated hierarchical lattices with large linear and rotational expansion. *J. Appl. Mech.* **86**(11) (2019)
33. Song, C., Li, S., Bao, H., Ju, J.: Design of thermal diodes using asymmetric thermal deformation of a kirigami structure. *Materials & Design* **193**, 108734 (2020)
34. Buchmann, E., Hadwiger, F., Petroll, C., Zauner, C., Horoschenkoff, A., Höfer, P.: A unit cell with tailorable negative thermal expansion based on a bolted additively manufactured auxetic mechanical metamaterial structure: Development and investigation. In: *Proceedings of the Munich Symposium on Lightweight Design 2021*. pp. 198–211. Springer (2023)
35. Parreira, R., Özelçi, E., Sakar, M.S.: Investigating tissue mechanics in vitro using untethered soft robotic microdevices. *Front. Robot. AI* **8**, 649765 (2021)
36. Cho, Y., Lee, E., Kim, Y.: Design and performance evaluation of retraction-type actuators with displacement amplification mechanism based on thermomechanical metamaterial. *J. Aerosp. Sys. Eng.* **14**(2), 28–35 (2020)
37. Jo, Y., Lee, E., Kim, Y.: Design and performance evaluation of extension-type actuators with a displacement amplification mechanism based on chevron beam. *J. Aerosp. Sys. Eng.* **15**(6), 1–9 (2021)
38. Xu, H., Farag, A., Pasini, D.: Routes to program thermal expansion in three-dimensional lattice metamaterials built from tetrahedral building blocks. *J. Mech. Phys. Solids* **117**, 54–87 (2018)
39. Steeves, C.A., e Lucato, S.L.d.S., He, M., Antinucci, E., Hutchinson, J.W., Evans, A.G.: Concepts for structurally robust materials that combine low thermal expansion with high stiffness. *J. Mech. Phys. Solids* **55**(9), 1803–1822 (2007)
40. Cardoso, J.O., Borges, J.P., Velinho, A.: Structural metamaterials with negative mechanical/thermomechanical indices: A review. *Prog. Nat. Sci.: Mater. Int.* (2021)
41. Schlitt, R., Kuhlmann, S., Sander, B., Neustadt, S.: Assessment of the rules on heater de-rating. *ESA Space Passive Component Days* (2016)
42. Arbogast, A., Roy, S., Nycz, A., Noakes, M.W., Masuo, C., Babu, S.S.: Investigating the linear thermal expansion of additively manufactured multi-material joining between invar and steel. *Materials* **13**(24), 5683 (2020)
43. Zhan, X., Zhu, Z., Yan, T., Gao, Q., Liu, Z.: The influences of different filler metals on the microstructure of invar fe-36ni alloy multi-layer multi-pass mig welding. *Mater. Res. Express* **6**(2), 026555 (2018)
44. Möller, F., Essig, T., Holzhauer, S., Förstner, R.: Experimental demonstration of a method to actively stabilize satellite structures against random perturbations of thermal boundary conditions using a closed-loop filter and controller approach. *CEAS Space Journal* pp. 1–18 (2023)



Additive Manufacturing of Continuous Fiber-Reinforced Composites

Anna Judenmann¹(✉), Philipp Höfer², Jens Holtmannspötter³,
and Ingo Ehrlich¹

¹ Faculty of Mechanical Engineering, Ostbayerische Technische Hochschule
Regensburg, 93053 Regensburg, Germany

{anna.judenmann,ingo.ehrlich}@oth-regensburg.de

² Institute of Lightweight Engineering, Universität der Bundeswehr München, 85577
Neubiberg, Germany

philipp.hoefer@unibw.de

³ Bundeswehr Research Institute for Materials, Fuels and Lubricants (WIWeB),
85435 Erding, Germany

JensHoltmannspoetter@bundeswehr.org

Abstract. The mechanical properties of additively manufactured plastic components, i. e. strength and stiffness, can limit their use as load-bearing structures. In particular, the use of continuous reinforcing fibers can significantly improve the mechanical properties of additively manufactured components and enable the production of load-bearing fiber composite structures. In this context, it seems reasonable to develop the required equipment and process workflows, but also procedures for the load-optimized positioning of fiber paths inside the component and its design. In this paper, the current challenges in the field of technology development of continuous-fiber reinforced 3D printing are highlighted. Possible solutions for the development of a 3D printing system and the generation of necessary toolpaths are presented on the basis of the FIBER-PRINT 3 project. Contents from a subsequent project present a design strategy for a load-optimized positioning of the continuous fiber reinforcement within the component and the implemented calculation of principal stress trajectories as a step towards optimization of the fiber positioning.

Keywords: Additive manufacturing · 3D printed composites · Continuous fiber reinforcement · Toolpath generation

1 Introduction

Fiber-reinforced composites have high specific stiffnesses and strengths, so the overall mass of a component can be significantly reduced. The possibility for individual fiber orientations allows load adapted design of the composite component. In many different areas, customized fiber composite solutions are increasingly in demand. When using conventional composites manufacturing processes, individualization of fiber composite structures is associated with high costs or may not even be possible due to certain restrictions in terms of design or manufacturing options. Due to the possibility of direct, tool-less manufacturing of complex shaped structures, the additive manufacturing process offers new solution possibilities with regard to product design, individualization and functional integration. By using continuous fiber-reinforced base materials in additive manufacturing, highly stressable components can be designed and directly manufactured according to the requirements. In this way, the advantages of additive manufacturing can be combined with the advantages of fiber composite structures. By using continuous fiber reinforcement, higher stiffnesses and strengths of a component can be achieved. However, the use of continuous fiber reinforcement in the additive manufacturing process presents several challenges. In addition to develop new equipment for the manufacturing process, the workflow of the process must be extended. This includes the combination of materials, as well as the design of fiber positioning paths within the component geometry and process control for component manufacturing. Different factors from these areas influence each other and must be taken into account during the development of the technology in order to improve the performance of the entire component and make it producible. In order to specifically influence the factors as well as their dependencies and ensure repeatability, a full control over the 3D printing system, material and process seems sensible. For this, flexible and open solutions are required on both the software and hardware sides.

2 Continuous Fiber Reinforcement in 3D Printing

The development of continuous fiber 3D printing technology has been driven by research institutes and industry in recent years. In particular, this includes the development of materials, equipment and associated processes. Some examples of equipment, process workflow and load-optimized component design are given below. Although commercially available equipment and process workflows for additive manufacturing of continuous fiber reinforced composites already exist, however they are subject to numerous limitations. The limitations in material selection, material placement and positioning of the fiber reinforcement mean that the full potential of combining additive manufacturing and fiber composite technology can only be exploited to a limited extent.

2.1 3D Printing Systems

Figure 1 shows some examples of various devices and impregnation concepts according to matrix materials used in continuous 3D printing process adapted from [6]. Examples include MARKFORGED MARK TWO [10] or ANISOPRINT COMPOSER [2]. These are desktop-based 3D printing systems that enable layer-by-layer production of the fiber composite and access manufacturer-specific semi-finished products for manufacturing. MARKFORGED MARK TWO processes a manufacturer-specific filament with thermoplastic matrix. ANISOPRINT COMPOSER works with a dual-matrix system, whereby fibers previously impregnated with thermoset matrix are embedded in a thermoplastic matrix material. In addition, various robot-based systems exist, for example the CF3D system from CONTINUOUS COMPOSITES [5]. These have a decisive advantage over desktop systems: the fiber reinforcement can be positioned spatially, which brings advantages over conventional 3D printing process, where the parts are created layer by layer. CONTINUOUS COMPOSITES deals with direct impregnation by using thermoset matrix system. In summary, the range of processes, components and applications is in steady growth. Desktop systems in particular are increasingly gaining acceptance and are already available to industry. A major part of the equipment operates on the basis of the FFF (Fused Filament Fabrication) process and uses pre-impregnated semi-finished products with thermoplastic matrix material. For larger components or special applications, robot-based or hybrid systems shall be used. A disadvantage in the accessibility to the robot-based technology is that in most cases these are systems with very high investment requirements, which cannot be provided to the industry as a ready-made solution, but require customer-specific adaptation and further development. Thus, there is still a need for further development of continuous fiber 3D printing technology.

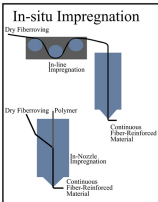
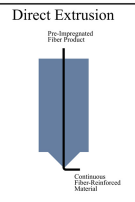
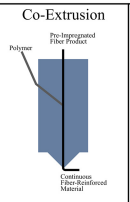
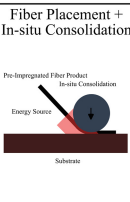
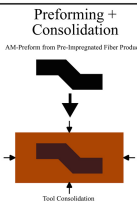
	In-situ Impregnation	Direct Extrusion	Co-Extrusion	Fiber Placement + In-situ Consolidation	Preforming + Consolidation
					
Thermoset	Continuous Composites Moi Composites				
Thermoplastic	Orbital Composites	aps.techsolutions INGERSOLL MANTIS COMPOSITES Markforged	anisoprint CEAD	AREVO AFPT ELECTROIMPACT Desktop Metal	ARRIS COMPOSITES 9T LABS
Fiber Feedstock	Dry Fiber	Filament	Filament	Filament/Slit Tape	Filament/Slit Tape

Fig. 1. Concepts of fiber impregnation according to types of matrix material used in additive manufacturing processes and equipment, adapted from [6]

2.2 Toolpath Generation

Fiber path deposition is currently mainly limited to layer-by-layer positioning, e. g. MARKFORGED EIGER [11], ANISOPRINT AURA [3] or 9T LABS FIBRIFY DESIGN SUITE [17]. Fiber positioning is performed according to predefined patterns or along a main load path within a previously topology-optimized geometry. Although there are already solutions that deposit the material spatially or on curved geometries, e.g. AI BUILD AiSYNC [1]. Further possibilities are offered, for example, by the SIEMENS NX CAM module MULTI AXIS DEPOSITION [15]. Here, multi-axis additive manufacturing as well as combination of additive and subtractive manufacturing processes are supported. A similar approach would be required for the CAESA TAPE STATION software from SWMS [16]. A fully automated generation of machine code for depositing continuous fiber reinforced material based on the component loads is still open. Reinforcing a component with continuous fibers offers advantages if the constraints and component loads are taken into account in such a way that the local fiber longitudinal direction can be oriented to the resulting load. Rigid filling patterns, as known from classic FFF (Fused Filament Fabrication) 3D printing, cannot be used in this case. However, it is important to determine the necessary fiber positioning in the component based on data, so that the loads can be optimally beared and linked by the fiber reinforcement.

2.3 Component Design

Before any generation of machine code can take place, the component design needs to be performed according to the constraints and loads. By identifying highly stressed areas in the component in advance, the reinforcing fibers can be optimally introduced, thus significantly improving the mechanical properties. There are many different approaches which deal with the design of parts to print in continuous 3D printing process and also with suitable fiber control. LIU et al. [9] summarize some current design opportunities and novel applications. A distinction can be made between monoscale and multiscale approaches. While the monoscale approach only deals with the design of the component, the multiscale approach includes both the part design and the fiber positioning inside the part. In their work, HUANG et al. [7] considered with macro- and microscale optimization and showed how critical the fiber trajectory planning is. The topology of the component was optimized first and in a second step also the fiber positioning within the component. Test specimens were manufactured using an in-house developed 3D printing system. The researchers compared components in which only the topology was optimized and filled with fibers and the multiscale optimized geometries: it has been found that indeed a 36.27% improvement in structural stiffness can be achieved by refined positioning of the reinforcing fibers. This investigation is just one of the examples that show the important role played by selective fiber positioning within the component. The studies for optimized filament patterns within a 3D printed component were also performed by MURUGAN et al. [12]. Here, an algorithm for customized filament layouts was

developed. Using an orientation field specified by the principal stress directions of the component, the software generates optimized filament paths considering printing parameters and boundary conditions as well as performing g-code generation. After adapting the output to machine-specific boundary conditions, such as handling continuous fiber curvatures, the algorithm can also be used for the machine code generation for the production of fiber composites in the Continuous Filament Fabrication (CFF) process.

3 Design of the 3D Printing System

To avoid constraints such as limited material selection or rigid infill patterns created by standard slicer software, it is important to use systems that are as open and flexible as possible in terms of 3D printing system operation, process path generation and availability of interfaces. By taking a step in the direction of a flexible solution, different subject areas and design domains with need of operation are opened up. The interaction between material, 3D system components, toolpath generation based on fiber-optimized component design, and the 3D printing process should be considered. For spatial freedom in positioning the print paths, industrial robot-based system is used in order to fully exploit the potential of directional design of fiber composite structures in the additive manufacturing process. In the following, different aspects of the technology development of a robot-based 3D printing system are addressed and their challenges are explained based on the FIBER-PRINT 3 project.

3.1 3D Printing Head

In the development of the 3D printing system in the FIBER-PRINT 3 project, the aim is to create a system that is as open as possible in terms of material selection and processing, i. e. no pre-impregnated material needs to be used. A special feature of the developed system is the UV polymer-based in-situ impregnation, which offers the possibility to select the UV polymer and the fiber reinforcement depending on the application requirements. For the consideration of impregnation parameters and quality a calculation method was implemented in MATLAB that takes into account fiber parameters (fiber diameter, number of fibers, etc.), matrix material parameters (dynamic viscosity, sliding friction, etc.) and impregnation parameters (process speed, fiber pretension, deflection radii, etc.). Due to the modular design, the impregnation module can be adapted to the process and material requirements. As shown in Fig. 2, the robot-based 3D printing system includes the impregnation module with respective material feed and the 3D printing head. Roving and UV resin are fed into the metering unit via material feed systems. The roving is pushed out of the 3D printing system by the conveyor module. It passes through a material pre-cure where the resin is pre-cured to ensure better conveyability. Instead of an anchor-point-method, a push-based approach is performed for a better process control and to avoid the need for an anchor point outside the component. Unlike thermoplastic matrix

materials, reattachment in the right place in continuous fiber 3D printing is a challenge because the material must form a bond with the previously deposited layer but not yet be completely cured. Pushing the roving has a supporting effect here, so that the curing process does not have to take place completely and the subsequent layer experiences a good bonding. The material can be deposited on the print bed or previously deposited layer. The final curing module hardens the material in the depositing process in the quantity required. If necessary, a cutting process can take place by using the cutting module. Again, there are numerous challenges, such as stabilizing the roving strand sufficiently to ensure a proper cut or reintroducing the severed strand into the nozzle. Each of the modules requires independent development and must also function as a complete system in the process.

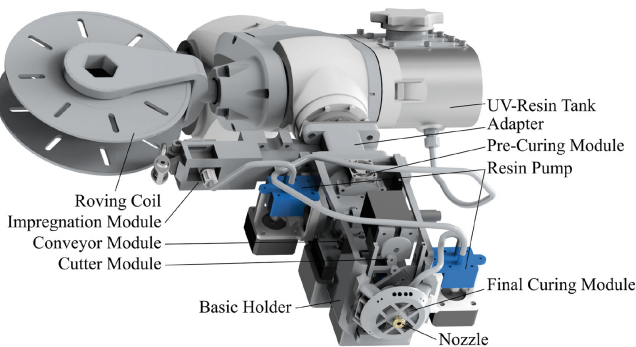


Fig. 2. CAD model of the printing system from the FIBER-PRINT 3 project

3.2 3D Printing System Control and Toolpath Generation

For the 3D printing head and robot control, a process chain consisting of several programming tools is used, which will be briefly highlighted. This includes applications for processing the robot and printing head signals as well as tools for generating machine code for the KUKA robot and the 3D printing head controller. For the control of the 3D printing system, the main control unit of the KUKA robot system was extended by additional BECKHOFF components which control the individual stepper motors, the LEDs for UV resin curing and the cooling fans. The robot controller communicates with the printhead controller via the ETHERCAT bridge, synchronizing the control of the stepper motors with the speed of the robot. A TWINCAT program interprets the commands within the machine code and uses them to control the stepper motors with the required settings. The machine code is created using a combination of the RHINOCEROS 7 [13] software package and the included GRASSHOPPER algorithm editor. The advantage here is that the software packages have numerous programming interfaces and plug-ins. Existing functions and routines can be used in GRASSHOPPER or

program blocks can be programmed individually by using PYTHON. For example, reference points for the process paths can be imported as basis for the generation of the tool paths. The KUKA|PRC interface is used to generate the machine code [14]. The KUKA|PRC interface provides the robot kinematics and the post-processor for translating generated travel paths into KUKA ROBOT LANGUAGE (KRL), as well as other additional tools, such as the KUKA CUSTOM KRL function, in which defined KRL blocks can be automatically included in the created KRL program. The predefined code blocks can be used to transmit commands to the robot control unit for controlling the stepper motors of the 3D printing head.

3.3 Printing Results

Different test specimens were produced by using the developed 3D printing system (Fig. 3). First, single rods were printed for microscopic examination of the impregnation quality. The developed impregnation module was considered suitable, since the microscopic examination showed that the fibers were impregnated.

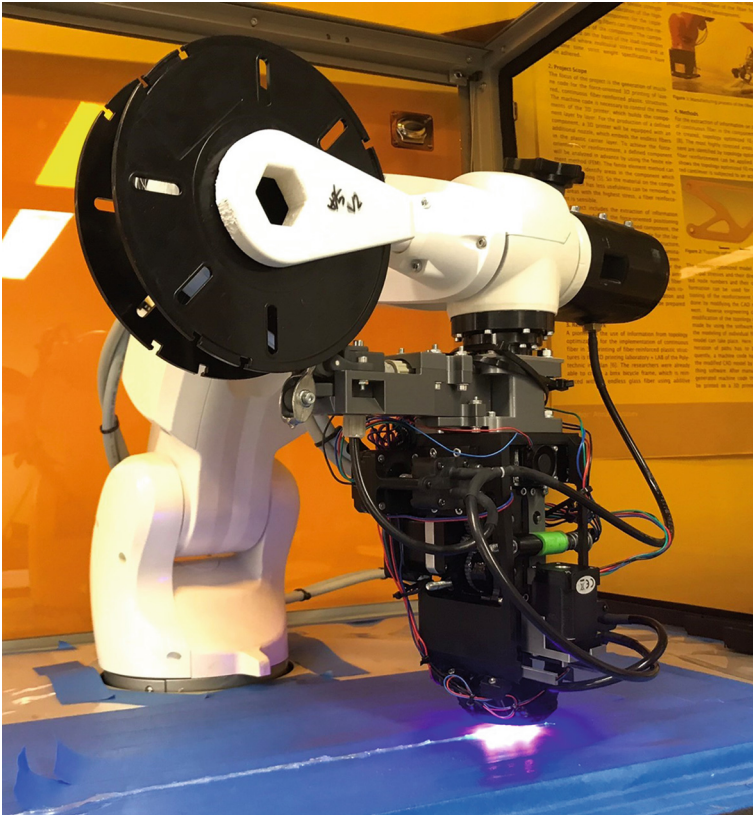


Fig. 3. Robot-based 3D printing system of FIBER-PRINT 3 project

Some specimens had voids or smaller fiber accumulations. In addition, different geometries were printed (Fig. 4) to investigate the functionality of the system and performance of the prepared programs. By manufacturing the curved geometries, as shown in Fig. 4a and 4c, the reliable operation of the conveyor module has been validated. The spatial deposition of impregnated roving (Fig. 4b) was performed without the use of support material. Multilayer rods (Fig. 4d) are of interest for the investigation of layer adhesion and the determination of required nozzle distance.

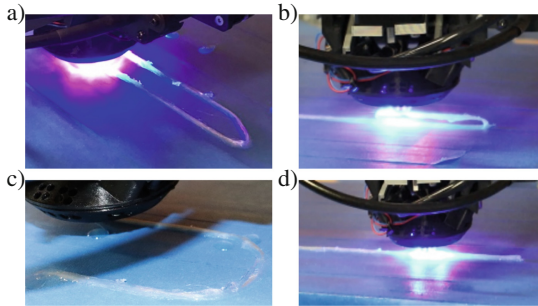


Fig. 4. Printed geometries: **a)** manufacturing of a topology optimized 3PBB, **b)** spatial curve, **c)** curve geometry, **d)** multilayer rod

4 Load-Optimized Component Design

A load-optimized, data-based design of fiber reinforcement with simultaneous consideration of process- and material-specific parameters has the potential to enable the production of innovative lightweight components using the 3D printing process. For this purpose, it seems sensible to analyze the load conditions of the component and to use the information obtained for the implementation of the reinforcing fiber paths in the 3D-printed component. It is also crucial that, in addition to the general path geometry and spacing of the deposited paths, the crossing points, reversal points and printing sequence are taken into account when calculating the travel paths, so that boundary conditions of the manufacturing process are also included in the process path generation.

4.1 Design Strategy for Load-Optimized Component Design

The goal pursued in the presented approach is the development of a computer-aided design methodology that enables systematic design and 3D printing of load-optimized continuous fiber-reinforced plastic structures, so that a complex fiber orientation that adapts to different boundary conditions can be ensured. Only the data in neutral format from a previous FE analysis should be used to calculate the fiber paths. For example, principal stress trajectories determined

on the basis of an FE simulation can be used as the basis for calculating the fiber position. Principal stress trajectories are defined by contours that follow the principal stress direction. Oriented along the principal stress trajectories, fibers can be positioned in the component so that the local longitudinal fiber direction is oriented to the resulting load. The Fig. 5 shows the design strategy for the planned examinations with associated optimization steps. It is intended to start at any component with appropriate constraints. After meshing and setting up the constraints, a load can be applied. The resulting normal and shear stresses should be used to calculate the principal stress trajectories. Based on the material and process specifications, constraints and the component load, a fiber model, more respectively a component fiber network pattern, has to be generated by using different optimization steps. This fiber network can now be used for generating the toolpaths on the one hand and its geometry for subsequent simulations on the other. For the generation of the toolpaths, a further optimization step is required. Contents such as print sequence or minimum fiber radii must be taken into account so that the part can be manufactured. The calculated fiber positions can be transferred into the respective machine language and finally a component can be manufactured. The manufactured component is to be tested so that the component properties can be determined. By using the geometry of the created fiber network, a realistically simulation can be performed, which can be of particular interest for spatial designs. The results from the simulation and the experiments can be compared in order to provide a statement about the accuracy of a prediction. As a first step, an FE model of a simple cantilever with constraints and load was created (Fig. 6a). The Vector Principle Plot analysis option in ANSYS MECHANICAL, as shown in Fig. 6b provides information about the stresses at individual element nodes. It provides the relative magnitudes of the principal quantities as well as their directions. The vector principles provide the directions of the highest normal stresses or elastic strains in response to a load condition for previously defined body points. By processing the data with MATLAB software (Fig. 6c), the information can be used as the basis for generating the fiber trajectories in the component.

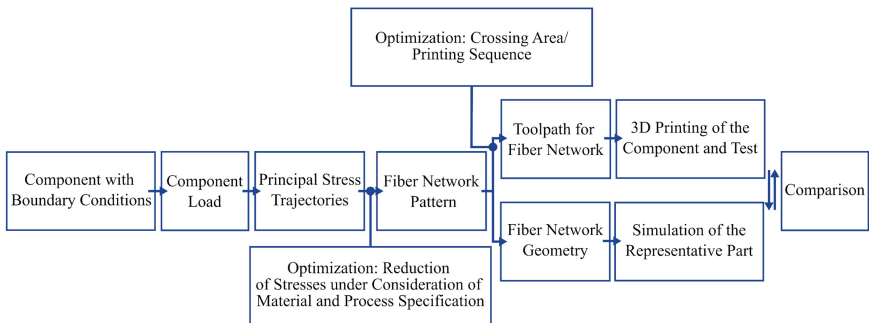


Fig. 5. Design strategy for load-optimized component design

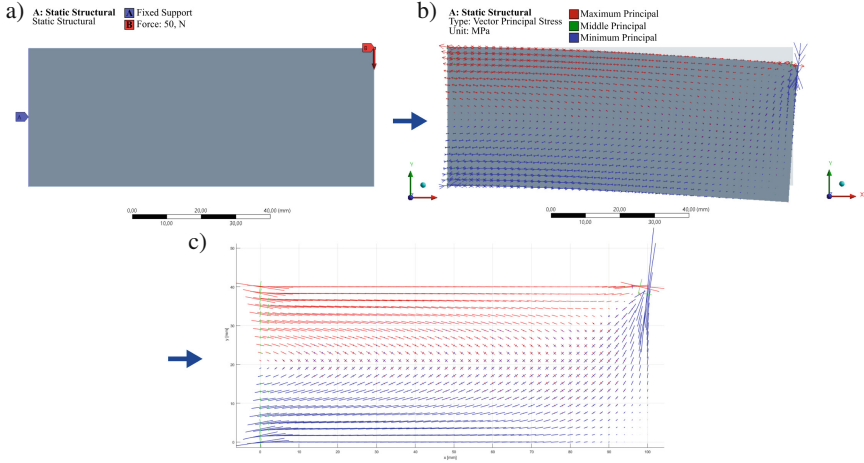


Fig. 6. FE analysis of a cantilever, **a)** cantilever with boundary conditions, **b)** vector principal, **c)** plot of vector principal stress in MATLAB

4.2 Current Results

A method by BEYER [4] which is shown in Fig. 7 is used to calculate the principal stress trajectories. At the beginning, information in a neutral data format is taken from the FE analysis. This includes nodal coordinates, the normal and shear stresses at each node, and the component boundary as a set of tuples. At discrete points, the information about the stress state present there is available. However, an interpolation procedure can be used to approximate the stress state at any point. A searching algorithm is used to calculate the trajectories. The procedure starts at a specified starting point. Beginning from this starting point, a second, preliminary point is determined in a defined radius. In this preliminary point, the stress state is approximated by using a multiquadratic analysis [8]. From the approximated normal and shear stresses, the principal stress and its direction can be calculated. Subsequently, the deviation of the angle of the principal stress from that at the starting point is compared. If it exceeds a set limitation, the search is continued within an arc until a point with the smallest allowed deviation of the principal stress direction is determined. So it becomes the actually searched point P_1 , and therefore the new starting point. The search algorithm continues until it reaches a termination criterion, for example the component edge. The path of the principal stress trajectories provides no information about the stress state present there. It only characterizes the directional trend of a principal stress, as shown in Fig. 8a. Therefore, the individual areas of the trajectories can be weighted with the corresponding principal stress and the stress can be quantified with a colored representation so that the amount of stress becomes visible (Fig. 8b). If the calculated principal stress trajectories are plotted together with the principal stresses acting at the nodes

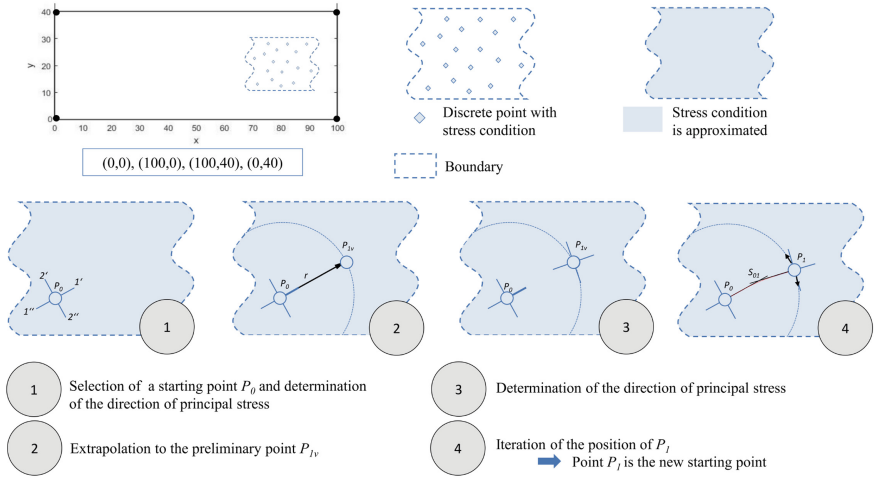


Fig. 7. Calculation of principal stress trajectories

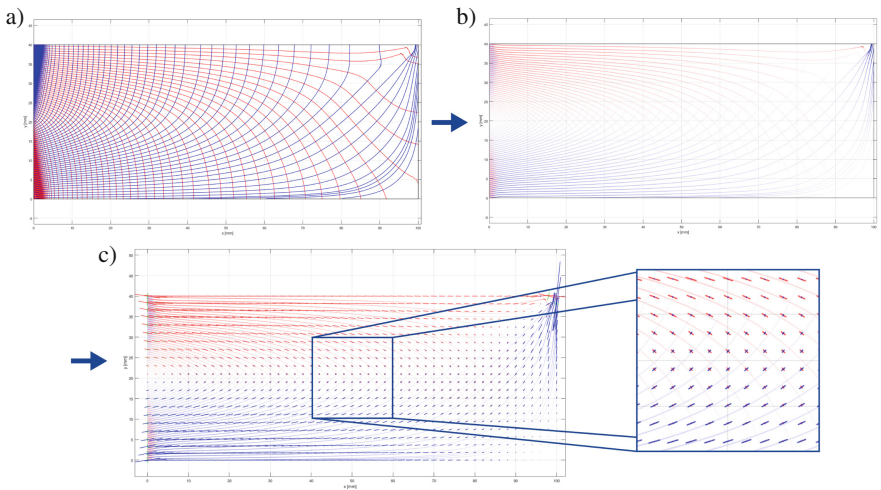


Fig. 8. Plot of principal stress trajectories in MATLAB, a) trajectories, b) quantified trajectories, c) quantified trajectories and principal stress result from the FE-analysis

from the FE analysis (Fig. 8c), it can be seen that both the trajectory directions and the color scaling are based on the respective principal stress quantities. A similar procedure can be performed when determining the locally required fiber volume content. As the principal stress trajectories are calculated step-by-step using the data from the FE analysis, attributes can be assigned to specific areas that control the necessary fiber volume content based on the principal stress variable prevailing there.

5 Summary and Outlook

The established manufacturing technologies have recently been extended by additive manufacturing technology. Commercial equipment for continuous fiber-reinforced additive manufacturing process comes with some limitations in terms of material selection and path generation. Fiber-optimized component design is another outstanding topic that is currently being addressed by research institutions in particular. As part of the FIBER-PRINT 3 project, an open, modular, robot-based 3D printing system with in-situ impregnation and associated process control were developed. Different geometries were printed to investigate the impregnation quality as well as the functionality of the system and the performance of the created programs. In the next step, the interaction of individual modules in the overall system and printing parameters will be further optimized to enable a stable 3D printing process. Furthermore, test specimens will be manufactured and tested in order to perform a material characterization.

While in the contest of FIBER-PRINT 3 research project only the 3D printing system has been developed, it is also reasonable to conduct further thoughts towards the component design and fiber positioning. For this purpose, first investigations have already been carried out and a design strategy for the generation of a fiber network model and subsequent manufacturing approaches have been developed. Based of data from the FE analysis, the main stress trajectories were generated and now provide a basis for positioning the continuous fiber reinforcement. In the next step, a fiber network model is to be created on basis of calculated trajectories. The required optimization steps include, for example, the required local fiber volume content, consideration of overlaps and constrictions.

Not all composite manufacturing processes can be substituted with the additive manufacturing, but it is an important enhancement to the conventional technologies. Continuous fiber-reinforced 3D printing offers good opportunities for sustainable material use: the fibers are only positioned where they are required and no material pre-cuts are necessary. This not only saves resources for the production of molds, but also valuable semi-finished products. If high-performance thermoplastics are used for the matrix material, the fiber and matrix components can also be separated and recycled. The topic of sustainability and recyclability becomes increasingly important, so that possibilities for material savings and material substitution should already be developed now.

References

1. AiBuild, AiSync. <https://ai-build.com/>. Accessed: 23. Nov 2022
2. Anisoprint, Solutions. <https://anisoprint.com/>. Accessed: 15. Nov 2022
3. Anisoprint, Aura. <https://anisoprint.com/aura/>. Accessed: 21. Nov 2022
4. Beyer, F. R.: Hauptspannungstrajektorien in der numerischen Festkörpermechanik. Dissertation, Fakultät Bauingenieurwesen, Technische Universität Dresden, Dresden (2015)
5. Continuous Composites, CF3D A Breakthrough in Composites. <https://www.continuouscomposites.com/technology>. Accessed: 15. Nov. 2022
6. DLR Institut für Faserverbundleichtbau und Adaptronik, How can 3D printing technologies for processing endless fibre reinforced materials be assessed in practice? <https://www.dlr.de/fa/>. Accessed: 7. Sept 2022
7. Huang, Y.; Tian, X.; Zheng, Z.; Li, D.; Malakhov, A.; Polilov, A. N.: Multiscale concurrent design and 3D printing of continuous fiber reinforced thermoplastic composites with optimized fiber trajectory and topological structure. *Composite Structures* **285** (2022) <https://doi.org/10.1016/j.compstruct.2022.115241>
8. Kraus, K.: Photogrammetrie, Band 3: Topographische Informationssysteme, Dümmler Verlag, Köln, 2000, ISBN: 3-427-78751-6
9. Liu, G.; Xiong, Y.; Zhou, L.: Additive manufacturing of continuous fiber reinforced polymer composites: Design opportunities and novel applications. *Compos. Commun.* **27** (2021). <https://doi.org/10.1016/j.coco.2021.100907>
10. Markforged, Mark Two. <https://markforged.com/de/3d-printers/mark-two>. Accessed: 5. Nov. 2022
11. Markforged, EigerTM 3D Printing Software. <https://markforged.com/de/software>. Accessed: 15. Nov. 2022
12. Murugan, V.; Alaimo, G.; Auricchio F.; Marconi, S.: An orientation-field based algorithm for free-form material extrusion. *Additive Manufacturing*, **59**, Part A, (2022). <https://doi.org/10.1016/j.addma.2022.103064>
13. Robert McNeel & Associates, Rhino 7. <https://www.rhino3d.com/>. Accessed: 30. Nov. 2022
14. Robots in Architecture, KUKA|prc Parametric Robot Control. <https://www.robotsinarchitecture.org/kukaprc>. Accessed 30. Nov 2022
15. Siemens NX, Machine Connectivity - Maximize your 3D printing hardware investment with direct printing. <https://www.plm.automation.siemens.com/global/en/products/manufacturing-planning/machine-connectivity.html>. Accessed: 12. Oct 2022
16. Tiemann, L.: Slicing methods and resulting layers for 3d printing. <https://www.swms.de/caesa/layers-and-slicing/>. Accessed 12. Oct. 2022
17. 9T Labs, Homepage 9T Labs – Software. <https://www.9tlabs.com/technology/software>. Accessed: 15. Nov. 2022



Insect Wing Inspired Design and Manufacturing of Multifunctional Automotive Applications Using Stereolithography and Subsequent Short Carbon Fiber Reinforcement

Felix Mesarosch¹(✉), Tristan Schlotthauer¹, Peter Middendorf¹, Frieder Fink², Fabian Kopp², and Jan-Philipp Fuhr²

¹ Institute of Aircraft Design, University of Stuttgart, Pfaffenwaldring 31, 70569 Stuttgart, Germany

{mesarosch,middendorf}@ifb.uni-stuttgart.de
<https://www.ifb.uni-stuttgart.de>

² Cikoni GmbH, Nobelstraße 15, 70569 Stuttgart, Germany

{fink,kopp,fuhr}@cikoni.com
<https://www.cikoni.com>

Abstract. An insect wing is characterized by an extremely lightweight but nevertheless strong cellular structure and represents a recurring and widespread solution in nature. In addition to its lightweight design, the vein-like structure is also responsible for the control and nutrient supply. A transfer of this multifunctional approach from nature offers new possibilities in the design, construction and production of extremely lightweight, yet fault-tolerant structures. To realize this principle for technical applications, additive manufacturing via the stereolithography process (SLA) and subsequent infusion with a suspension of epoxy resin and carbon short fibers is used. In order to obtain reproducible production results, the infusion takes place on a therefore developed test rig. To demonstrate the potential of this process, a conventional automotive side exterior mirror is topology-optimized based on the insect wing design rules. During the experiments, 30 wt% carbon fibers (CF) with a mean length of 80 μm can be processed, which results in an increase in stiffness at the same tensile strength compared to a solid polymer structure. In order to achieve electrical conductivity of the structural framework, carbon nanotubes are added to the infusion suspension. As a result, a reduction in weight and assembly effort is achieved by the multifunctional insect wing design.

Keywords: Additive manufacturing · Stereolithography · Short fiber reinforcement · Topology optimization · Bionics

1 Background and Motivation

In this approach, biological principles are used and transferred to technical applications in order to realize multifunctional lightweight constructions.

The insect wing is chosen as a model from nature, as it represents a very common solution in the insect world.

In this project, the structure and functions of the insect wing are to be transferred to an automobile side exterior mirror. An exterior mirror consists of a large number of individual components and must comply with a wide range of requirements such as aerodynamics, structural rigidity and assembly effort.

1.1 Multifunctional Insect Wing

An insect wing is characterized by an extremely lightweight but nevertheless strong cellular structure and represents a recurring and widespread solution in nature. The typical structure is shown in Fig. 1. It is characterized by struts in the longitudinal direction and transversal stiffeners. A thin membrane of approx. $1\ \mu\text{m}$ thickness is stretched between the resulting cells, forming the aerodynamic surface. In addition to its lightweight design, the vein-like structure is also responsible for the control and nutrient supply. For example, the trim tank on the outside of the wing can be controlled via the structure.

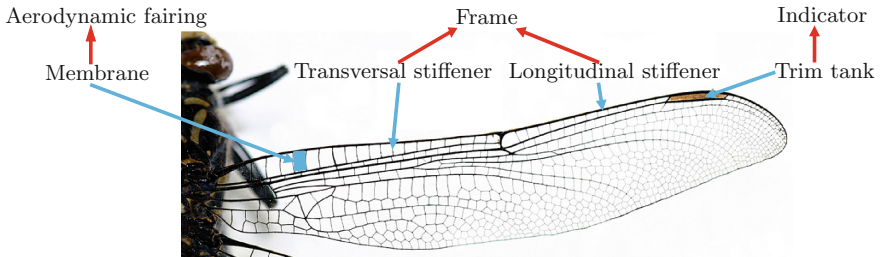


Fig. 1. Insect wing functions (adapted from [1])

These elements and properties of the insect wing are then transferred to the automobile exterior mirror. The frame will be represented by the transversal and longitudinal stiffeners. The membrane between the cells provides the aerodynamic fairing around the structure. The structure itself is to be made electrically conductive in order to contact an indicator.

1.2 Goal

The problem with bionic structures is that they usually have a complex geometry that is difficult or impossible to produce by conventional manufacturing technologies. Additive manufacturing processes can solve this problem. However, the mechanical properties of polymer-based processes are limited and metal-based processes are expensive.

Therefore, a novel hybrid manufacturing process is used and further developed in the following [2]. In this manufacturing process, Stereolithography (SLA) is used to produce the outer shell structure of the part. The resulting hollow structure is then infiltrated with a carbon fiber (CF) thermoset suspension in order to improve the mechanical properties.

The goal of this project is to achieve aerodynamic, mechanical and electrical properties simultaneously, in the sense of a multifunctional insect wing.

2 Topology Optimization and Design

Topology optimization is used here to generate load-appropriate bionic structures as a basis for the design. This is a numerical method based on the FEM for generating design proposals in the early stage. The starting point is the available design space of a component as well as various structural, but also manufacturing constraints. The result of the topology optimization is an optimal material distribution within the design space. Typically, these are truss-like structures as required for the manufacturing process.

The process of the mirror design is shown in Fig. 2. The design space of the mirror is created by filling the outer geometry and then removing the various functional parts such as the mirror glass and adjustment motors. Areas of the exterior mirror that serve as functional surfaces or to mount screws are separated as nondesign space so that no material can be removed here during optimization. The 0.1 mm thick outer cover made of PETG is modelled with shell elements and bonded to the outer surface of the design space. Mirror glass and adjustment motors are represented in the model in a simplified way with mass elements.

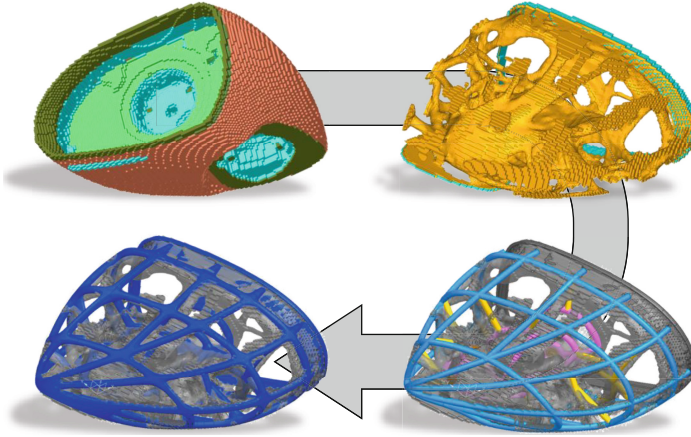


Fig. 2. Design process

The novel manufacturing process discussed here leads to a hybrid material consisting of structures with a fibre-reinforced and thus anisotropic material in the core, and a shell structure made of isotropic material. Since the load paths are not known at the beginning of the topology optimization, the orientation of the fibres and the material distribution between the core and the shell structure cannot be determined. This circumstance makes it necessary to represent the design space with a homogenized isotropic equivalent material model. The material properties are estimated with a representative circular cross-section of $d = 4$ mm inner and $D = 6$ mm outer diameter and thus 55% photopolymer and 45% carbon fiber thermoset suspension consisting of 30 wt% CF via a mixing rule.

Different load cases are considered in the topology optimization. These are subdivided into operating loads like various accelerations, the aerodynamic pressure distribution on the outer surface and other misuse loads and substitute loads for consideration of the crack stop function. A direct consideration of the desired crack stop function is not possible with common topology optimization methods, as it is a component behaviour after initial failure. However, the topology optimization is based on a linear static simulation without failure. As a substitute, a dummy load case is therefore introduced in the form of individual forces acting normal to the outer surface in a 50 mm grid. This load case provides regular, redundant load paths to the cover of the mirror, which can stop cracks.

The manufacturing process has some fundamental constraints, especially with regard to the infusion of the suspension, which can only be taken into account to a very limited extent in the topology optimization. The minimum wall thickness of the structure can be specified in the topology optimization. However, as already mentioned, no distinction can be made between suspension and shell structure. Furthermore, no influence can be exerted on the cross-sectional shape of the channels or their connecting nodes to each other. Such process-

related restrictions must then be considered when transferring the result of the topology optimization into a CAD design.

Bionic, free-form structures often prove challenging to classical CAD design approaches. In most cases, the main goal is to create one or more geometrical bodies that meet all structural, functionality, package and manufacturability requirements they are presented with. Since manufacturability highly depends on the chosen process, the novel hybrid manufacturing method plays an integral part in the decision making. The end product of the design process for a hybrid structure, as discussed in this paper, has to meet the following requirements:

- Hollow base structure with a dual function as an injection mold
- Channel cross section primarily circular for stability during the injection process
- Minimum channel cross section diameter to allow suspension flow during the injection process
- Maintain minimum wall thickness for stability during the injection process
- Smooth transitions and node areas for unobstructed suspension flow
- Provide multiple cavities for galvanic isolation

To meet all goals a hybrid design approach is chosen, which combines the classical CAD design tools with a non-uniform rational basis spline (NURBS) surface based method.

Widely used for 3D design in the entertainment industry, as well as for interpreting topology optimization results for additive manufacturing, NURBS based design is highly efficient in the creation of smooth surfaces and organic structures, but proves challenging when hard targets, such as exact wall thicknesses or cross section diameters have to be met.

At first, all attachment surfaces, including the outer shell geometry are designed with a classical approach. Then, a network of splines and tubular sections is created in accordance with the final topology optimization result, which serves as a temporary reference structure for the next design phase. The diameters of the tubes are determined by the target cross section dimensions and can still be modified easily. In the second design phase, the reference structure is manually translated into several NURBS-based solid bodies. The primary body represents the filled geometry, while the secondary bodies represent the suspension in two galvanically isolated cavities. In the final step of the hybrid design approach, all previously created interface and attachment areas are combined with the primary NURBS-based body and the suspension bodies are subtracted to create the hollow base structure, before sprue positions are determined and added. The step from reference structure to final structure is illustrated in the bottom half of Fig. 2.

The used hybrid design approach combines the efficiency of NURBS-based surfaces with the dimensional stability and reliability of classical CAD modeling methods and proves to be suitable to design hybrid structured parts, as presented. To increase design efficiency and allow for a more widespread use, improvements to the software capabilities are required. Especially the separate

creation of the suspension bodies is one of the key hurdles in efficiently creating NURBS-based, hollow structures.

A simulative validation of the final design has not been carried out here. Especially for the prediction of the strength, much more complex material models with corresponding underlying material tests are necessary. The local material properties strongly depend on the distribution and orientation of the fibres of the suspension. For an accurate prediction of the component properties, a coupled filling and structure simulation would therefore be necessary. There are similar process chains that could be built on in the field of fibre-reinforced thermoplastic injection moulding.

3 Manufacturing Technology

The process to be carried out for subsequent short fiber reinforcement is shown in Fig. 3.

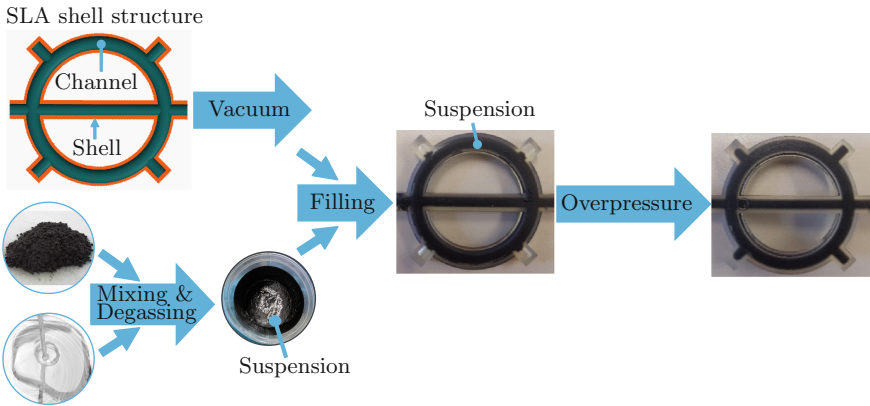


Fig. 3. Process to execute

The baseline is the topology-optimized shell structure, which is produced with the SLA process. This structure needs to be evacuated. The second step is the mixing of the carbon short fibers with the infiltration resin with simultaneous degassing. To achieve high mechanical properties, a homogeneous, void-free suspension is essential. The suspension is then infiltrated into the evacuated shell structure. Pressure is applied to completely fill undercuts. The suspension then cures in the structure.

In order to carry out this process as reproducibly, error-free and semi-automated as possible, a test rig developed for this purpose is used. It is shown in Fig. 4.

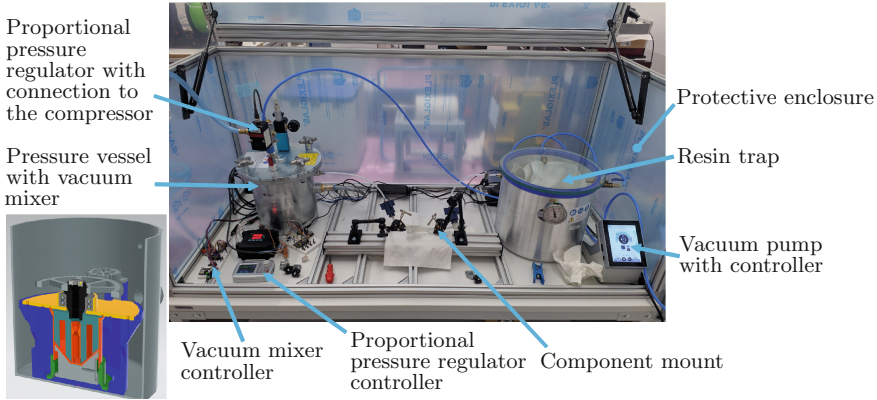


Fig. 4. Test rig for component infiltration

The central part of the system is a pressure vessel, in which there is an apparatus for mixing and degassing the suspension. The pressure inside the vessel can be controlled via a proportional pressure regulator. From the mixer, the suspension can be conveyed directly out of the vessel by pressure differences through hoses. This avoids decanting, which would cause air to get into the suspension. The component to be infiltrated is mounted on the test bed and the hoses are connected to it via sprues. From the left side the hose with the suspension supply comes from the pressure vessel and on the right side the hose goes to the vacuum chamber.

For the infiltration of the parts, the low-viscosity epoxy resin Epikote RIMR 135 is used with the hardener RIMH 137 in a ratio of 100 to 30 parts by weight. The fibers chosen are Sigrafil C M80-4.0/240-UN (SGL Carbon SE) with a mean length of $80\ \mu\text{m}$ and no sizing.

With this process technology in combination with this resin system and these fibers, fiber contents of up to 30 wt% can be reliably mixed and conveyed.

For the side exterior mirror topology optimized in Sect. 2, the hollow structure fabricated with SLA is shown in Fig. 5a. This part is infiltrated with a suspension consisting of 30wt% carbon fibers. A thermoformed PETG cover is then bonded to the structure, which serves as an aerodynamic fairing. The finished side exterior mirror can be seen in Fig. 5b.

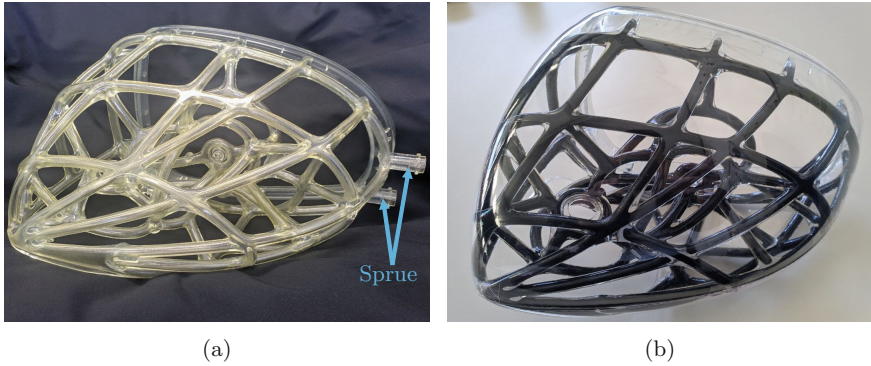


Fig. 5. Production and infiltration of the side exterior mirror. (a) Hollow structure, (b) Finished part

4 Results

In order to determine if the structural requirements are met, the following mechanical and electrical tests are carried out.

4.1 Mechanical Properties

In order to verify the mechanical properties, tensile specimens are produced via SLA in accordance with DIN EN ISO 3167. The cross-sectional area of the test area is round with a diameter of 6 mm. These specimens are made both solid from the photopolymer BASF RG35 and hollow with a channel diameter of 4 mm. This diameter corresponds to the smallest cross-section that can be infiltrated reliably, and a wall thickness of 1 mm is minimally required to safely withstand the pressure differences during the filling process. These values also serve as boundary conditions for the topology optimization in Sect. 2.

Figure 6 compares the results of the tensile tests with solid material and 30 wt % carbon fiber filling. It shows that the short fiber reinforcement increases both the Young's modulus by 189% and the tensile strength by 16%. The elongation at break, on the other hand, decreases by 79% due to the higher stiffness of the carbon fibers. The numerical values can be found in the average in Table 1.

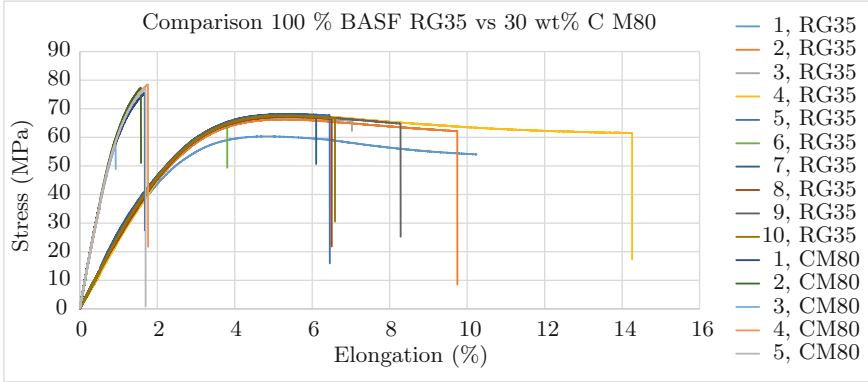


Fig. 6. Comparison of mechanical properties

Table 1. Comparison of mechanical properties

Parameter	BASF RG35	BASF RG35 + 30 wt% C-fibers	Comparison
Young's modulus	2.53 GPa	7.33 GPa	Increase by 189%
Tensile strength	66.5 MPa	77.12 MPa	Increase by 16%
Elongation at break	7.9%	1.67%	Decrease by 79%

4.2 Electrical Conductivity

In the sense of a multifunctional approach, the structure should fulfill not only mechanical but also electrical tasks. Therefore, LEDs shall be contacted directly via the structure. According to [3] the percolation threshold depends on the aspect ratio of the short carbon fibers. The fibers used have a diameter of 7 μm , resulting in an aspect ratio (AR) of 11.43. This is too low for the formation of a sufficiently conductive network with the maximum fiber weight fractions that can be processed. Therefore, it is necessary to add carbon nanotubes (CNTs) as conducting filler. These have according to the technical data sheet an AR of 2000–10000. Although the addition of CNTs significantly improves the electrical conductivity, the high AR also causes the viscosity of the suspension to increase very fast. As a compromise between processability, mechanical and electrical properties, a content of 20 wt% carbon fibers and 2 wt% CNTs is therefore chosen.

For the exterior mirror demonstrator, two channels are separated from the rest of the structure. These channels are filled with the CNT modified suspension. The contacts of the LEDs and the power supply are glued directly into the structure with silver epoxy glue. The positions of the conductive channels and connections are shown in Fig. 7.

The contacting and power supply of the LEDs through the structure works in principle with this method, but the resistance in the range of $30\text{ K}\Omega$ is very high, so that the luminosity would be insufficient for traffic applications.

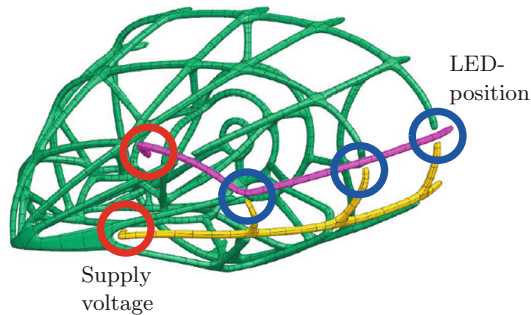


Fig. 7. Path of the electrically conductive structure

4.3 Crack Stop Function

For an insect, the cellular structure of the wing is of great importance, since damages and cracks in the membrane remain restricted to one cell, thus ensuring the ability to fly [4]. As a transfer of this principle into the technical application, a part of the exterior mirror is used and the surface of the structure is covered with a thin adhesive foil. In addition, an initial crack is added in the middle of this part. Via an SLA printed individual connection, this build-up is clamped into a tensile testing machine and then pulled apart. The experimental setup is shown in Fig. 8a. for an insect wing and in Fig. 8b for the exterior mirror section.

As result, the technical replica behaves in principle similar to the insect wing. The crack grows over the cell and remains locally confined to it. However, due to the significantly higher stiffness of the carbon fiber-reinforced struts respectively the resulting lower elongation at break, the structure fails before the crack reaches the end of the cell. For technical applications such as the side exterior mirror, this characteristic can be used, for example, that in the event of a stone impact, only a hole appears in one cell, but the overall function of the mirror is still maintained.

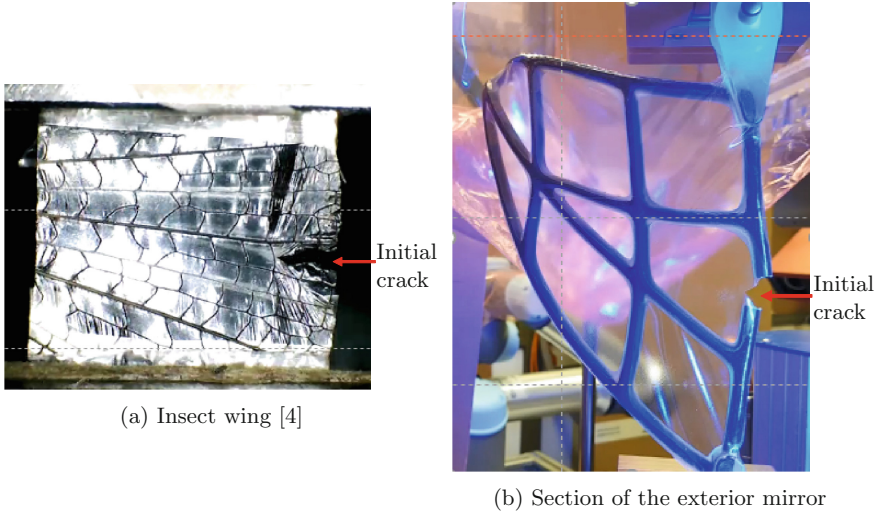


Fig. 8. Demonstration of the crack stop function

5 Conclusion and Outlook

It has been shown that the structure and function of an insect wing can be transferred to the technical application of an automotive side exterior mirror. For this purpose, the mirror was successfully topology-optimized and designed for the subsequent fiber reinforcement process. With the test rig set up, components can be infiltrated reproducibly and reliably with up to 30 wt% carbon short fibers. Thus leading to an increase of the Young's modulus by 189% and the tensile strength by 16% compared to the pure photopolymer. The electrical conductivity of the structure was realized by adding CNTs, however, the resistance is still high. By covering the structure with a thermoformed PETG film, a cellular, damage-tolerant structure was created.

This allows the production of topologically optimized, multi-functional light-weight structures in a short fiber composite design. Aerodynamics, stiffness and electrical conductivity are achieved simultaneously in the sense of a multi-functional insect wing, which allows a reduction in weight and assembly effort.

Further research should focus on improving the test rig for reliable processing of higher fiber content. In addition, it would be useful to match the resin systems (photopolymer and infiltration resin), coatings and fibers (length, diameter) to each other to improve the reinforcement effect. It is also possible that a matched system simultaneously increases electrical conductivity.

Another research aspect is the development of a process simulation, e.g. to make structural-mechanical forecasts by predicting the fiber orientation in the structure.

References

1. IronChris. Odonata – Gomphidae wing structure. This file is licensed under the Creative Commons Attribution-Share Alike 3.0 Unported license. To view a copy of this license, visit. <https://creativecommons.org/licenses/by-sa/3.0/deed.en>, https://commons.wikimedia.org/wiki/File:IC_Gomphidae_wing.jpg. Accessed: 15. Dec 2022
2. Schlotthauer T, Geitner A, Seifarth C, Schendel O, Lüuck T, Kaindl R, Kopp D, Spalt S, Walter P, Nolan D, and Middendorf P.: Reinforcement of stereolithographic manufactured structures by the subsequent infusion of short carbon fibers. SAMPE Europe Conference. Baden/Zürich – Schweiz. (2021)
3. Electrical conductivity of short fibre-reinforced polymers. *Science and Engineering of Short Fibre-Reinforced Polymer Composites (Second Edition)*. Ed. by Fu Sy, Lauke B, and Mai Yw. Second Edition. Woodhead Publishing Series in Composites Science and Engineering. Woodhead Publishing, 241–269. (2019) <https://doi.org/10.1016/B978-0-08-102623-6.00009-3>
4. Dirks, J.H., Taylor, D.: Veins Improve Fracture Toughness of Insect Wings. PloS one. (2012). <https://doi.org/10.1371/journal.pone.0043411>



Comparison of Different Material Systems for Filament Winding Based on the Split-Disk Experiment and Setup of a Digital Twin

Ruben Krischler^(✉), Markus Blandl, Maike Kliewe, Stefan Carosella, and Peter Middendorf

Institute of Aircraft Design, University of Stuttgart, Pfaffenwaldring 31, 70569 Stuttgart, Germany

<https://www.ifb.uni-stuttgart.de>

krischler@ifb.uni-stuttgart.de, blandl@ifb.uni-stuttgart.de,
kliewe@ifb.uni-stuttgart.de, carosella@ifb.uni-stuttgart.de,
middendorf@ifb.uni-stuttgart.de

Abstract. Wound components have gained relevance in recent years, especially due to hydrogen pressure vessels. However, the burst pressure test of the vessel structures is associated with a high time and monetary expenditure, which is why a simplified split-disk test is often applied. In the split-disk test, ring fragments are cut from a test pipe and are loaded in tension, which induces a membrane-like stress state in the laminate. The present study addresses the different mechanical material behavior during split-disk testing of a wet-wound material compared to a commercial Towpreg and the TPreg[®] material developed at the Institute of Aircraft Design. All three materials have the same layer orientation as well as similar process parameters. In addition to a mechanical investigation of the samples, optical measurement techniques are used to evaluate the quality of the material in terms of porosity and resulting resin areas. Furthermore, a finite element model is used and thus a digital twin of the experimental setup is created to test suitable numerical methods for the different material systems. This is done in order to be able to optimally design a real tank structure with a reduced experimental effort.

Keywords: Filament-Winding · Wet-Winding · Towpreg · TPreg · Bobbin Infusion Process · Split-Disk · Digital Twin · Finite Element Simulation

1 State of the Art and Motivation

Gaseous hydrogen storage (CGH₂) has played a major role in the mobility sector in recent years. Storage currently takes place at working pressures of up to 700 bar [1]. Due to the high burst pressures to which they are exposed, hydrogen pressure vessels made of fiber-reinforced composites have to meet high requirements in terms of the quality of the material used and the respective manufacturing process. In addition to the high qualitative grade, the material used should also be processable at an adequate speed to reduce the production costs of a single vessel. In recent years, the use of Towpregs has emerged as an opportunity to significantly increase production speed beyond the classic wet-winding process [2].

The Towpreg represents a roving pre-impregnated with resin, which is wound onto a bobbin. In addition to increased winding speeds, the use of the material offers the opportunity to precisely control the fiber volume content in a wound pressure tank. The main disadvantage that comes with the use of Towpreg is the high cost of materials [3]. Also, the possible fiber-resin combinations are specified by the manufacturer, which significantly limits the material selection when using a commercial Towpreg.

TPreg[®], which was developed at the Institute of Aircraft Design, attempts to overcome the prevailing disadvantages of a commercial Towpreg and a classic wet-winding process. On the one hand, the manufacturing process associated with the TPreg[®] allows any fiber to be combined with almost any infiltration resin, promising high flexibility even for small quantities of material required. As a consequence it is possible to carry out the manufacturing process oneself and then process the Towpreg produced in-house. On the other hand, the process also ensures that the rovings used are efficiently infused, thus reducing the amount of resin required in comparison to a wet-winding process.

2 Bobbin Infusion Process and TPreg[®] Material

The fundamental development of a new manufacturing process for pre-impregnated semi-finished fiber products originated at the Institute of Aircraft Design. The core of the process is the possibility to enable users to produce their own vacuum-based prepreg with low resource input and known production equipment (e.g. vacuum pump).

This means that for most resin systems, the transport cooling chain, the usual ordering times and the necessary logistics for this are no longer required. And for the first time, it will be possible to freely select material combinations of fiber and matrix and use them on site in the required quantities. To distinguish the new prepreg process from previous commercially available systems, the brand name TPreg[®] is used for this type of prepreg production.

The basic element of the infusion process is a perforated fiber support, e.g. in the form of a bobbin (hollow inside) which is spooled with the desired fiber material, as shown in Fig. 1. Moreover the prepreg properties can be determined by the spooling pattern, the bobbin size, the process conditions and the fiber material used. For the impregnation process, the bobbin is designed in a way that the impregnating agent can penetrate from the center of the fiber packing to the outside and vice versa.

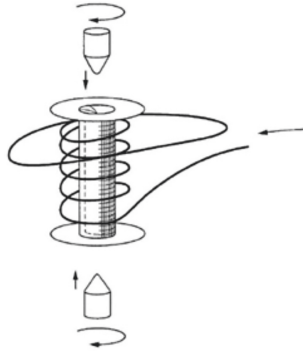


Fig. 1. Perforated bobbin with spooled fiber material [4]

The impregnation process can be carried out both in an open and a closed container. For both, the bobbin is placed in the container together with the wound rovings. In the case of an open version, the impregnation can be drawn out by changing the environmental conditions. In the closed version, on the other hand, a pressure system can be implemented. In Fig. 2 the impregnation container and an exemplary pressure system is shown. Furthermore, the process can also be carried out in such a way that several bobbins or fiber packages are impregnated together. Each fiber package is integrated into a container and impregnated simultaneously with any number of parallel bobbins. Robot systems can then remove the packages and process them further or load the containers themselves. This type of parallelization makes the process scalable and very flexible in adapting to changing material requirements. In this study a 170 mm TPrep[®] bobbin with a core diameter of 20 mm was used and illustrated in Fig. 3. The usable width is 164 mm and the outer diameter is 74 mm. The usable maximum volume of this bobbin is 653.5 cm^3 , which corresponds to a maximum prepreg weight of approx. 980 g with a material density of $1.5 \frac{\text{g}}{\text{cm}^3}$.

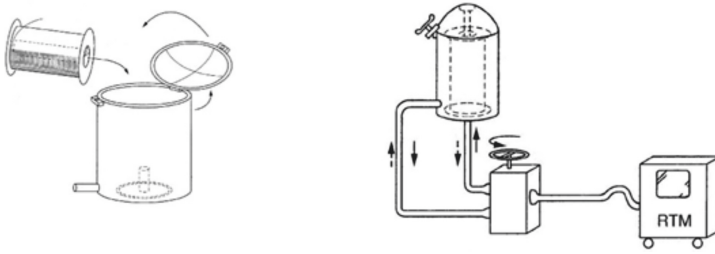


Fig. 2. Impregnation container and pressure system [4]

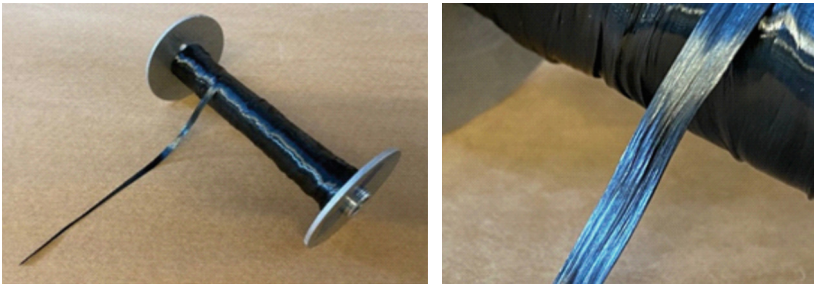


Fig. 3. Finalized TPrep[®] material

3 Specimen Geometry and Material Analysis

For the test geometry, several specimens were wound on a cylindrical mandrel with a diameter of 70 mm. The specifications listed in Table 1 apply to the tube specimens produced. The roving used is a Toray T700 24K 50C for all three manufacturing processes evaluated. In addition to the manufacturing processes, different yarn tensions in the winding process were varied, too. Since each of the three manufacturing processes has different requirements with regard to the resin system, this differs for all three methods. However, the mechanical properties are approximately equivalent according to the respective data sheets [5–7].

Table 1. Manufacturing specifications of the six wound tubes

Sample Description	Tow20	Tow30	Tow40	W5	W10	W15	T10
Manufacturing Process	Towpreg			Wet-Winding			TPreg
Yarn Tension [N]	20	30	40	5	10	15	10
Average Thickness [mm]	3.06	3.06	3.01	2.78	2.90	3.40	3.36
Fiber Type	T700 24K 50C						
Resin Type	TR1112			LY564			RIM135
Stacking Sequence	$\pm 14^\circ, \pm 60^\circ, \pm 14^\circ, \pm 60^\circ$						

After manufacturing the test specimens, the fiber volume content of the respective tubes is determined and microscope images of tube sections are taken. Starting with the evaluation of the fiber volume content, at least three random samples are taken along the tube and the fiber volume content is evaluated using the chemical laboratory method according to DIN EN 2564 A. The results for both fiber and void volume content are summarized in Table 2. It is noticeable that the fiber volume content of the Towpregs is consistently high. In contrast, an influence of the yarn tension seems to be clearly recognizable in the wet-wound tubes. If the yarn tension increases, the fiber volume content decreases significantly. A low fiber volume content can also be observed in the TPreg[®]. The void volume fraction is quite high for all three materials at any yarn tension. Therefore, in addition to the chemical laboratory method, microscope images are also evaluated to get a clearer impression of the wound material. Figure 4 shows the resulting material quality for all manufacturing processes investigated. It is noticeable that mainly interlaminar, macroscopic pores are formed in the commercial Towpreg. This can be explained by the fact that the Towpreg used is not sufficiently wetted with resin and thus tends to trap larger areas with air during the winding process. In addition to larger pores (both inter- and intralaminar), the wet-wound material also shows the effect that the resin pushes outwards at higher yarn tensions and creates a resin film on the outside. This can be seen especially in Fig. 4f) at a filament tension of 15N. Also, the high variation of the resulting thickness seen in Table 1 can be explained by the resin pocket. Although the TPreg[®] material has the highest void content according to the laboratory evaluation in Table 2, it can be seen in the microscopy image that these spread less locally in the material. Furthermore, the TPreg[®] also has a resin film deposited on the outside, which implies that the material behavior during the manufacturing process is more similar to a wet-wound fiber. Since a final statement on the material behavior of TPreg[®] cannot be made exclusively by microscopic evaluation, the split-disk test is consulted for the qualitative classification of TPreg[®] in comparison with the two commercial materials.

Table 2. Fiber Volume Content with corresponding Void Volume Content for each specimen

Sample Description	Tow20	Tow30	Tow40	W5	W10	W15	T10
Fiber Volume Content [%]	57.35 ± 0.55	58.16 ± 1.14	58.18 ± 0.26	54.87 ± 1.07	51.93 ± 1.41	42.80 ± 0.38	47.34 ± 0.96
Void Volume Content [%]	4.08 ± 0.62	3.25 ± 0.82	2.78 ± 0.17	5.67 ± 0.60	4.51 ± 0.66	4.35 ± 0.34	5.84 ± 0.57

4 Split-Disk-Experiment and Digital Twin

In the following chapter, the experimental and simulative setup of the split-disk experiment will be discussed. In addition to the experimental and numerical setup, the results of the test series will also be examined.

4.1 Experimental Setup

The series of tests performed is based on Procedure A from ASTM Standard D2290-19a. This describes a test setup in which a ring section is placed over the two-split disc and a tensile load is applied. Figure 5 illustrates a design of the split-disk experiment proposed according to the standard. The deformation of the ring section causes a bending moment in the gap between the two half-disks

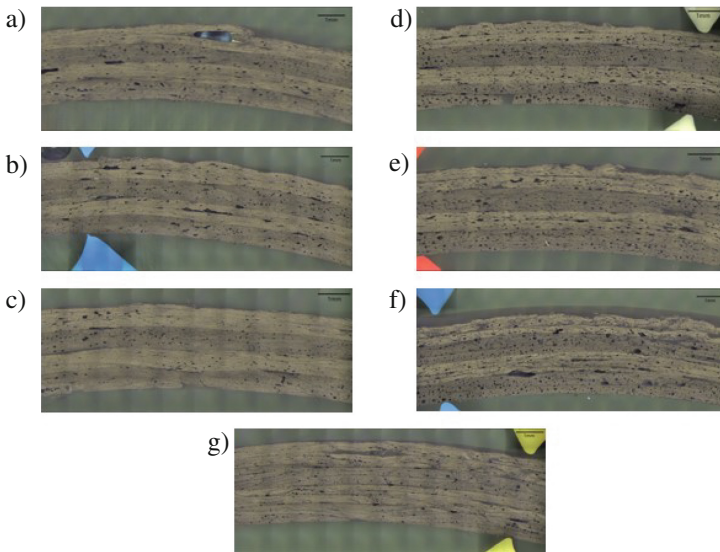


Fig. 4. Microscope images for all manufactured materials a)-c): TowPreg d)-f): Wet-Winding g): TPreg®

to be superimposed on the tensile load, which is why the measurable results are described by the standard as an apparent tensile strength. This is stated in Eq. 1, in which σ_a represents the apparent yield tensile stress, P_b the breaking load and A_m the minimum cross-sectional area of the specimen [8].

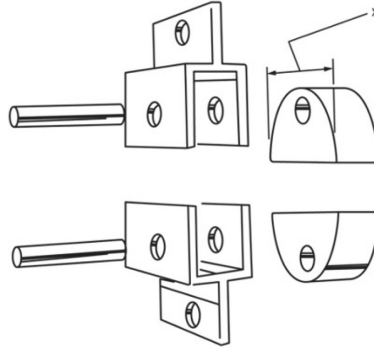


Fig. 5. Experimental Fixture according to the ASTM standard [8]

$$\sigma_a = \frac{P_b}{2A_m} \quad (1)$$

For the test series, seven 15.5 mm width sections were cut from each of the wound tubes introduced in Table 1. The fixture designed at the Institute of Aircraft Design is installed in a 250 kN testing machine from Hegewald&Peschke. The test speed is $2 \frac{mm}{min}$. For the evaluation of the tests the resultant force and displacement are measured. The testing setup is shown in Fig. 6.

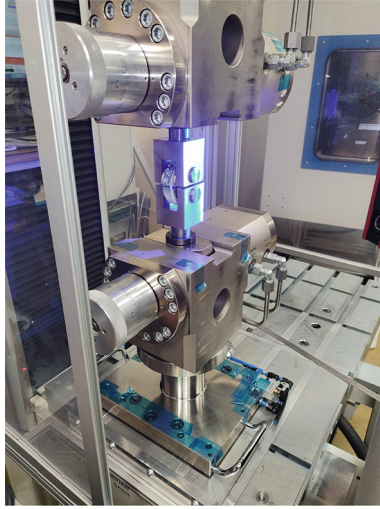


Fig. 6. Experimental setup at the Institute of Aircraft Design

4.2 Digital Twin

The digital test setup is implemented as an FEM model in Ansys LS-Dyna. Fully integrated solid elements are built up layer by layer for the ring section. Underintegrated shell elements are used for the split disks. Furthermore the thickness of the simulation model is set to 3 mm and its width to 15.5 mm. Figure 7 illustrates the digital test setup. The load case is set up exactly according to the real test model, so that the upper rigid moves upwards and the lower one is held in place. Meanwhile, there is a contact definition between each of the split disks to the CFRP ring.

For the material law, the Pinho failure model implemented in LS-Dyna (*MAT261*) is used for a fiber volume content of 50% [9]. The data is based on an internal material characterization of an equivalent material. Furthermore an element-by-element material orientation is assigned for each layer.

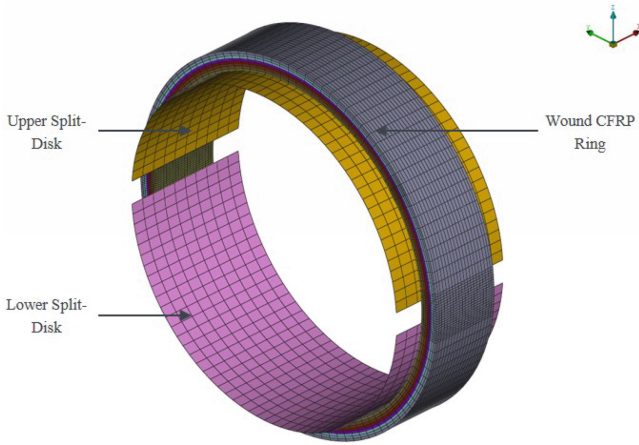


Fig. 7. Digital Test setup for the Split-Disk Experiment

4.3 Results

The sample series is evaluated using the ASTM standard described in Chap. 4.1. Thus, the apparent hoop tensile strength is determined and compared. Figure 8 compares the averaged ring tensile strengths for each specimen and normalizes them to a fiber volume content of 50%. The test evaluation shows that the commercially available Towpregs provide constant values for the strengths regardless of their yarn tension. However, it can also be seen that they perform somewhat worse compared to the wet-wound specimens and the TPreg[®]. This can be explained by the fact that the chosen ply structure provokes inter-fiber failure, whereby a dryer material ensures poorer load transfer.

The apparent ring tensile strength of the wet-wound material increases with increasing yarn tension. This can be explained by the fiber volume content evaluation from Table 2. It can be seen that the fiber volume content is also lowest in the tube with the highest yarn tension, which means that the specimen is very rich in resin and thus strengthens the load transfer between the fibers.

Qualitatively, it can be seen that the mechanical behavior of the TPreg[®] is also oriented to that of the wet fiber, which has already emerged from the fiber volume content evaluation in Table 2, as well as from the microscope images. The wet-wound material and the TPreg[®] exhibit the best agreement between simulation and experiment. Since the strength values were taken from an existing characterization of a comparable material, a detailed material characterization of the three selected materials is still pending.

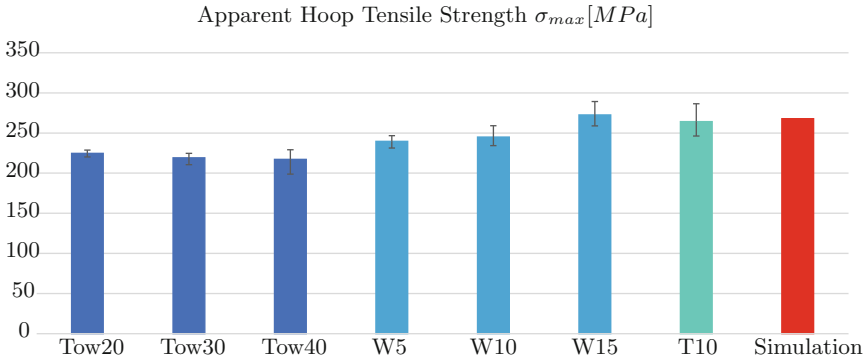


Fig. 8. Comparison of the different Apparent Hoop Tensile Strengths for each specimen (normalized to a fiber volume content of 50%)

5 Conclusion and Outlook

In summary, a varying of yarn tension in the Towpregs has little effect on the fiber volume content, thickness, and microstructure. In contrast, a clear influence of the yarn tension can be identified for the wet-wound material. On the one hand, a clear push-out of the resin can be identified at high yarn tension. This can be seen both in the increasing average thickness of the wet-wound specimen and in microscope images based on a resin film on the outside of the tube. Qualitatively, the TPreg[®] material behaves similarly to the wet-wound material, which can also be verified by a resin film on the outside. Furthermore, the fiber volume content of TPreg[®] is significantly lower than for the commercial Towpreg. The aforementioned observations are also confirmed in the split-disk test. The dryer commercial Towpreg shows a poorer performance in apparent ring tensile strength due to the ply structure. On the other hand, the wet-wound tubes perform significantly better, showing greater visual and mechanical similarity with the TPreg[®].

The simulation reproduces the wet-wound material and the TPreg[®] best. Material characterization for all three materials is needed to better simulate the differences between the three manufacturing processes in order to be able to consider the effects of yarn tension and dry spots.

Acknowledgements. This paper was written as part of the HyCoPE (Hydrogen Composite Pressure Vessel Engineering 4.0) public research project funded by the German Federal Ministry of Economic Affairs and Climate Action. We would like to thank both the Ministry and the Forschungszentrum Jülich GmbH (PtJ) for their support.

We would also like to thank all of our project partners, in particular Roth Composite Machinery GmbH for winding the test tubes.

Supported by:



**on the basis of a decision
by the German Bundestag**

References

1. Miller, E.L., Thompson, S.T., Randolph, K., Hulvey, Z., Rustagi, N., Satyapal, S.: US Department of Energy hydrogen and fuel cell technologies perspectives. *MRS Bulletin* **45**, 57–64 (2020)
2. Jois KC, Mölling T, Gries T, Sackmann J.: Towpreg-Based Design and Manufacture of Multi-Supply Filament-Wound Composite Pressure Vessels. *SAMPE neXus 2021* (2021)
3. Nebe M.: *In Situ Characterization Methodology for the Design and Analysis of Composite Pressure Vessels*. Springer (2021)
4. Method and Apparatus for Impregnating Semi-Finished Fibrous Products. US 10106930B2. University of Stuttgart. (2014)
5. Huntsman L.: *Advanced Materials Araldite[®] LY564/Aradur[®] 917/Accelerator 960-1*. (2004)
6. Composites T.: *Technical Data Sheet: TR 1112 TCR[™] Resin*. (2017)
7. Hexion. *Technical Data Sheet: MGS[®] RIM135*. (2005)
8. ASTM D.: 2290-19a. *Standard Test Method for Apparent Hoop Tensile Strength of Plastic or Reinforced Plastic Pipe*. American Society for Testing and Materials, Philadelphia (2019)
9. Pinho, S., Iannucci, L., Robinson, P.: Physically-based failure models and criteria for laminated fibre-reinforced composites with emphasis on fibre kinking: Part I: Development. *Composites Part A: Applied Science and Manufacturing* **37**, 63–73 (2006)



Digital Approaches for Optimization of Composite Processing: Bayesian Optimization for Impregnation and Fibre Spreading In-Situ Monitoring

Florian Schön[✉], Fabian Hübner, Marius Luik, Jeremias Thomas, Rodrigo Albuquerque, and Holger Ruckdäschel

Universität Bayreuth, Universitätsstraße 1, 95447 Bayreuth, Germany
florian.schoenl@uni-bayreuth.de, fabian.f.huebner@airbus.com,
marius.luik@uni-bayreuth.de, jeremias.thomas@gmx.de,
Rodrigo.Q.Albuquerque@uni-bayreuth.de, ruckdaeschel@uni-bayreuth.de

Abstract. In order to optimize the processing of composite materials, the importance of digital methods in materials science is steadily increasing. In this study, two approaches were used for composite materials processing. First, for the winding of H₂ storage vessels using towpregs, Bayesian optimization (BO) was used as a tool to find optimal process conditions within specified parameter limits. The applied algorithm can efficiently maximize selected target values within existing parameter limits. In this case, the goal was to achieve a maximum towpreg width of a winding standard of ¼" (6.35 mm) with a fibre volume content between 55–60 vol.%. Although this maximum couldn't be achieved within the specified parameter limits, the BO resulted in a steady reduction of the standard deviation and thus a significant increase in process quality. In the second part of this study, an in-situ monitoring tool for a fibre spreading process was developed. Fibre spreading of low-cost but mechanically weak Heavy Tows has the potential to be used in the future production of H₂ storage vessels, especially for the highly cost-effective automotive market. To gain deeper insights into the spreading process itself, a sufficient in-line monitoring tool is needed to observe and analyse the spreading behaviour of the given fibres. Using a camera setup and a developed Python tool, a method has been developed to observe the spreading process of the fibres in depth. This opens the possibility for further in-depth parameter studies on the spreading behaviour and the use of Heavy Tows in automotive applications.

Keywords: Hydrogen Storage Vessel · Bayesian optimization · In-situ Monitoring · Fibre Spreading

1 Introduction

Hydrogen technology is of huge interest due to nowadays technology push of green energy for cars, transport and aviation. Whether stored as gas (GH_2) at $+22\text{ }^\circ\text{C}$ or liquid (LH_2) at $-253\text{ }^\circ\text{C}$, the gravimetric energy density is remarkably higher than gasoline, kerosine, among others [1]. To enable a suitable storage solution at high pressures or cryogenic temperatures, the energy carrier H_2 can be efficiently stored in carbon reinforced composite vessels. The production of such rotationally symmetrical parts requires an enormous manufacturing effort, usually in a winding process using in-situ wet-impregnated fibres or preimpregnated towpregs [2]. To enable a higher market share of hydrogen vehicles, an economical production of such storage vessels is of great interest in today's research and development. [3–5].

Digital approaches to process and material optimisation are new data-based techniques that promise to increase production rates or quality. In common DoE studies, for example, a statistical approach could lead to an acceleration of the test matrix progression. In addition, Bayesian optimization (BO) is also a specific digital strategy for maximising values of a given function-based system. In this approach, a script is used to determine different variables and their mutual influence in a summarizing function. Each variable can be translated as a vector in multidimensional space, the BO script searches for a point in the multidimensional space to maximise a predefined value. For detailed background information on the basics of BO, further literature is referred to and recommended at this point. [6, 7] This methodology can already be found in literature in materials science. Li et al. [8] used the BO approach for the synthesis of short polymer fibres. Another successful use of BO and additionally the use of machine learning was done by Albuquerque et al. [9]. Novel bio-based resin systems with different hardener combinations were investigated to achieve the highest possible glass transition temperature. The use of a machine learning algorithm also enabled the researchers to predict the targeted glass transition temperatures with a high success rate.

In this study, the functional system is an impregnating machine for the manufacturing of a pre-impregnated towpreg with desired high width accuracy. In manufacturing, the width accuracy is needed to produce wound laminates without gaps or overlaps of the roving strand. The target was a winding standard of $\frac{1}{4}$ " (6.35 mm). A secondary objective was to achieve a typical fibre volume content of 55–60 vol.%. Obviously, some of the variables such as the angle of the resin drum influence the resin content and thus the fibre volume content. Therefore, the variables can also be chosen in dependence on each other. Further experimental details are explained in section 2.2.

Besides the search for optimal process parameters in the winding process of towpregs, the fibre spreading of Heavy Tows is the second topic investigated in this study. Especially for the cost-efficient automotive sector, low-cost Heavy Tows are an ideal base material for the future production of H_2 hydrogen vessels [10]. At present, these are mainly mostly used in low mechanical performance applications like the sports

industry or in rotor blades for wind turbines [11, 12]. However, H₂ storage vessels though require high mechanical performance due to high safety requirements. It is shown in the literature that a reduction of the fibre areal weight and the resulting cured ply thicknesses increase the mechanical performance at laminate level [13, 14]. With the technique of fibre spreading, it is possible to use the low-cost Heavy Tows as a similar high-performance material to the commonly used 12K and 24K carbon fibres. In order to exploit this potential, a reliable and successful tool for monitoring the spreading process itself is first required, which was developed in this study. The literature already contains some basic knowledge about the fibre spreading process and the factors that influence the spreading behaviour. The focus of this study will mainly be on the technique of mechanical spreading, as it has a high industrial relevance and is used with the UD500 spreading machine. Mechanical spreading is also already semi used in filament winding, where static pre-spreading bars are often installed along the fibre path [2].

Tonejc et al. presented a laboratory setup for single tows using five spreader bars to reduce friction [15]. In addition, two light sectioning sensors were used to monitor the roving width. In preliminary tests, a smaller bundle width than expected from the model was found. The authors assumed a reduced spreading behaviour due to variations in the applied sizing. A parameter study was not included in the conference paper. A similar set-up, consisting of 5 spreader bars, was published as part of the IGF-Vorhaben Nr. 18713 N, where a self-regulating tow-spreading machine was developed [16]. Similar to Tonejc, cameras were placed before and after the spreading unit to allow real-time width analysis and defect detection. In order to determine a reasonable range of parameters for subsequent self-regulation, a screening experiment was conducted. Regarding quality aspects, a significant impact on gap formation was found with an increasing number of spreader bars. Filament breakage showed comparable behaviour to fibre width, but increased more dramatically with increasing friction. Parameters such as the deflection angle, the rod diameter and the friction coefficient had a stronger influence on the fibre breakage than on the width. From this, it could be deduced that fibre breakage is strongly related to the friction between the spreader bar and the roving. In a second step, a final quadratic model, which determines the influences of the individual parameters on quality and width, was adapted to the results of a 3³-full-factorial plan, which includes machine speed, tow tension and deflection angle. Further investigations into the influence of parameters such as tension, machine speed or deflection angle were also carried out by Gizik, with tension and deflection angle showing a strong influence on most used fibres [17]. Gizik also showed, that some of the spread Heavy Tows, depending on the manufacturer, achieve similar values for tensile strength and modulus at laminate level as standard 12K rovings. Other influencing factors such as different sizings or the amount of sizing on the fibres or the influence of temperature during spreading are hardly found in the literature, resulting in several research gaps for now.

2 Experimental

2.1 Materials

Part A: Bayesian Optimization for Towpreg processing

For the experimental towpreg impregnation, aerospace grade IM7 12K carbon fibres from *Hexcel Corporation* (Stamford, USA) were purchased. The fibres were used as received from a bobbin on a winding and impregnation unit from *Engineering Technology Corporation* (Salt Lake City, USA). An in-house developed experimental hotmelt towpreg epoxy resin system was used for impregnation. The pot-life of the material is not limited by the temperatures used.

Part B: In-situ Monitoring for Fibre Spreading

For the fibre spreading trials ZOLTEK PX35 50K Heavy Tows have been kindly provided by *ZOLTEK Corporation* (Bridgeton, USA). These consist of 50.000 filaments with a tex of 3700 and an epoxy sizing amount of 1 wt.%.

2.2 Methods

Part A: Bayesian Optimization for Towpreg processing

As shown in many other publications, the spreading of the tow to a certain width during impregnation can depend on the creel tension, the resin content, the resin barrel angle, the impregnation speed, the bath temperature and the fibre volume content. These variables define the vectors in the multidimensional space that have been defined. The systematics of the variables boundary conditions are listed in Table 1.

Table 1. Parameter boundaries for the Bayesian optimization process

Parameter	Minimum Boundary	Maximum Boundary
Creel tension / N	1	7
Gap distance / resin film / μm	50	100
Impregnation temperature / $^{\circ}\text{C}$	77	95
Contact length on resin drum / mm	45	98
Impregnation speed / mm/min	2.9	29
Aim 1: Tow width / mm	2.5	6.35
Aim 2: Fibre volume content / vol.%	55	60

A total of 30 experiments, selected by a Python script, were performed in blocks. In each experiment, the width on the mandrel was measured at three different points, as a stable and repeatable process was observed.

Part B: In-situ Monitoring for Fibre Spreading

Fibre spreading of Heavy Tows was performed using an industrial spreading machine UD 500 from *Karl Mayer GmbH* (Obertshausen, Germany). The machinery is able to vary several process parameters including temperature, vibration frequency, machine

speed, deflection depth of spreader bars and tension along the rovings. For this study the following parameters, which were found as a rough standard throughout several other publications were used.

Table 2. Machine parameters used for spreading trials

Machine Parameter	Value
Temperature / °C	100
Vibration frequency / hz	30
Machine speed / m/min	5
Deflection depth / mm	12
Roving tension / cN	800

The roving tension which is not automatically controlled was adjusted by hand using a tension measurement tool DTSB-2000 from *Hans Schmidt & Co GmbH* (Waldkraiburg, Germany). The measurement was conducted at a distance of 1 m from the grammage, at the height of the roving, during active processing over ten seconds.

Width Analysis

Image analysis was carried out to determine the tow width of the value during the fibre spreading process. Of particular importance is the acquisition of data at different positions in the machine, as the tension on the tow varies locally. The cameras were positioned at 4 points along the spreading unit, which can be seen in Fig. 1. A laboratory tripod was chosen to save space when placing the cameras and to obtain high quality, vibration-free images as the cameras are not mounted on the machine itself. The type of camera selected is a USB webcam with a resolution of 8 K and a manual lens with variable focus of 5–50 mm from *Ailipu Technology Co., Ltd.* (Shenzhen, China). An additional chippable ring light was positioned around the camera to control the brightness. The camera focus is manually adjustable and lockable to ensure similar conditions for each measurement. All four cameras are connected to a computer that controls the image acquisition simultaneously.

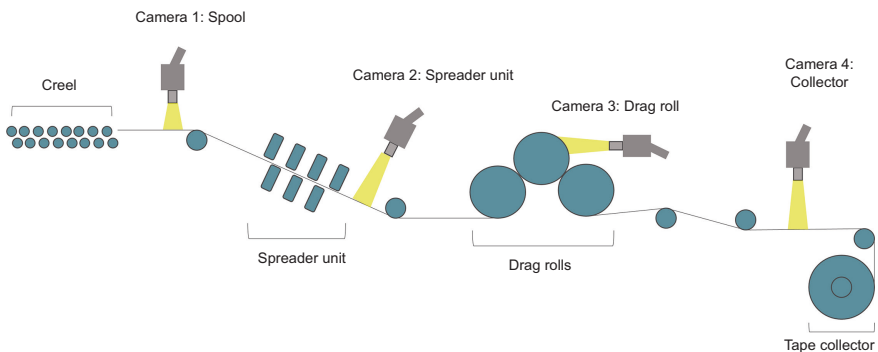


Fig. 1. Positioning of cameras as schematic representation.

In-situ Monitoring

Camera 1 (“Spool”) was positioned right above the entrance of the spreader unit to represent the pristine fibres. Camera 2 (“Spreader unit”) films between the drag roll and spreader unit, whereas camera 3 (“Drag roll”) aims at the drag roll. Last, camera 4 (“Collector”) is positioned between the drag roll and the compaction rolls, to represent the fibres before they are collected.

The width detection is performed in 6 steps. First, the picture is transformed into grey scale. The fibre itself is then distinguished from the background via binarization. The selected threshold is calculated dynamically using Otsu’s method. The algorithm selects the threshold as the minimal weighted within-class variance (see Eq. (1)) [18].

$$\sigma_w^2 = w_0\sigma_0^2 + w_1\sigma_1^2 \quad (1)$$

Each summand is calculated using the pixels up to a set threshold (index 0) or higher than a set threshold (index 1). The weights w are calculated as follows:

$$w_x = \frac{\text{total pixels in the respective region } x}{\text{total pixels in the image}} \quad (2)$$

The mean value for each respective region is calculated using Eq. (3):

$$\mu_x = \frac{\text{weighted sum of intensities}}{\text{total pixels in respective region } x} = \frac{\sum^i \text{pixel value}_i + \text{pixel count}_i}{\text{total pixels in respective region } x} \quad (3)$$

The weighted variation for the respective region can be written as:

$$\sigma_x^2 = \frac{\sum^i (\text{pixel value}_i - \mu_x)^2 * \text{pixel count}_i}{\text{total pixel in respective region } x} \quad (4)$$

After calculating the weighted within-class variance for all pixel values, the found minimum can be selected as the threshold. This limits the algorithm to bimodal contrast ratios. Also, blurring reduces its applicability. As can be seen in Fig. 2, for some pictures parts in the background are also selected as part of the roving. Therefore, in step 4 an evaluation frame is selected in which the roving is detected properly. Before the width of the roving can be detected by counting the black pixels for each row in the frame, the tilt of the roving must be detected. This is done by fitting a linear regression to the mean position of each row. The angle of the resulting fit line is subsequently incorporated in the determination of the real width of the roving. Strong deviations of the roving tilt also indicate an incorrect evaluated picture and easily allow their detection and exclusion.

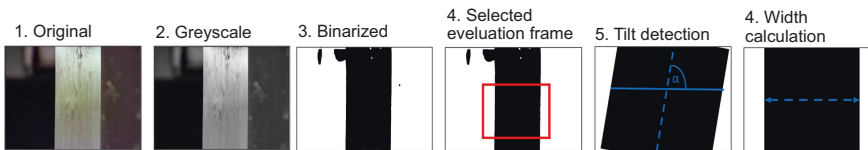


Fig. 2. Processing steps of roving width detection using image processing.

3 Results and Discussion

3.1 Part A: Bayesian Optimization for Towpreg Processing

First, the overall experiments of the towpreg part of this approach study are highlighted. The width of the ongoing experiments is shown in Fig. 3.

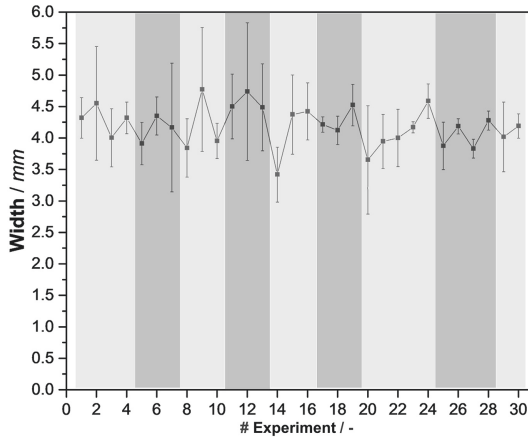


Fig. 3. Development of towpreg width over research blocks via Bayesian optimization.

Each experiment varied quantitatively in one of the six parameters that influence each other and the width as parameter number 7. No optimisation by maximising the width in the first place is visible via the consecutive numbers. In the standard deviation, the values vary from 3.7 to 4.8 mm. With an initial width of the dry roving from the bobbin of approx. 2.5 mm, this is an increase of +50% to more than 90%. This can be seen as a remarkable improvement, since no additional calendering rolls are used, and the impregnation procedure is a continuously driven fast process. A second improvement was seen in a steadier state process. In the first half of the experiments, the standard deviation is remarkably big (No. 2,7,9,12), while in the second half, only experiment No. 20 shows a big standard deviation. By optimising the parameters in the function, a more uniform steady-state process was found, with significantly better uniform widths. Further, the correlation of the parameters brought another analytical point to be investigated. To explore the multidimensional room and gather knowledge about the interdependent factors, the parameters were correlated in a heat map, which is shown below in Fig. 4.

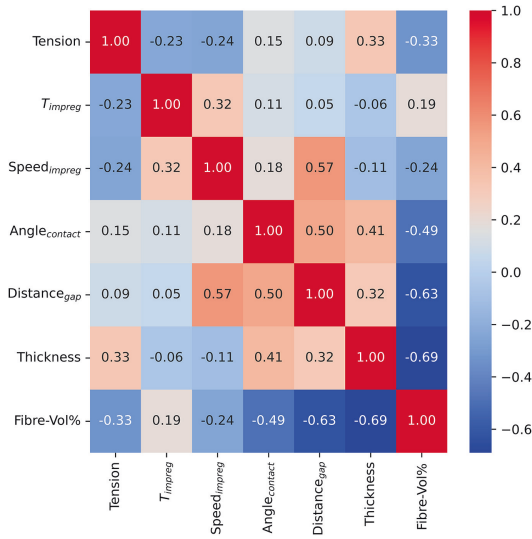


Fig. 4. Heatmap for significance of parameter influence.

Here the calculated correlation factors are shown in a range from +1 to -1 . While 0 means no correlation, +1 means a fully positive correlation and -1 means an inverse negative affecting correlation in terms of maximizing a value or parameter. As such, the diagonal value represents a solely numerical positive correlation to itself by +1. Overall, most values range from 0 to $+/-0.5$, representing a low correlation. Two values in this plot were seen as “hits” when it comes to interpretation. The “width-fibre $vol\%$ ” showed the strongest correlation with a value of -0.69 . Out of all processing parameters, the resulting fibre volume content of the roving seems to affect the roving width the most. Since the width shall be maximized, and the increasing fibre volume content decreases the width, this parameter is treated negatively. Of course, the fibre $vol\%$ of the roving is depending on the resin on the drum during impregnation. As such, the *contact angle* (-0.49) and the *gap distance* for the resin film (-0.63) have secondary correlation factors with the *fibre $vol\%$* . This represents an interdependent correlation of the chosen parameter, which was able to be quantified in this study.

To further highlight and investigate the strong correlation between fibre $vol\%$ and tow width, the results of the experiments of these two parameters were plotted and are represented in Fig. 5.

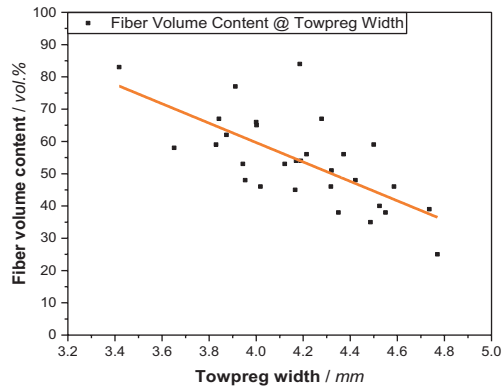


Fig. 5. Development of fibre volume content over towpreg width.

Here, the fibre volume content is decreasing with increasing width of the tape. The data points are supported with a linear regression (orange). Clear evidence can be concluded by the digital support of the BO. The first aim is affected and directly correlated with the second aim. A high fibre volume content is not achievable by having a high roving width at the same time, which the negative correlation factor of -0.69 concluded. Experimentally, this can be explained as follows: The resin content in the towpreg is highly affected by the resin brought on the drum roll while impregnation. Thus, the towpreg gathers width by the liquid resin. As such, the resin content is directly related to the other parameters. This allows a higher spread to be achieved as the material flows towards the edges and increases the width of the tow. The higher the fibre volume content and the lower the resin content, the lower the tendency of the material to spread. As such, the line could also be drawn to the initial dry width of 2.5 mm reaching the theoretical maximum of 100 vol.% fibre by the regression line.

3.2 Part B: In-Situ Monitoring for Fibre Spreading

To determine the variation of roving width during constant spreading conditions, see Table 2, a single spool was spread and measured over a duration of 2 h. The fibre width, evaluated for all 4 measurement stations, is plotted in Fig. 6 versus the actual time of the measurement.

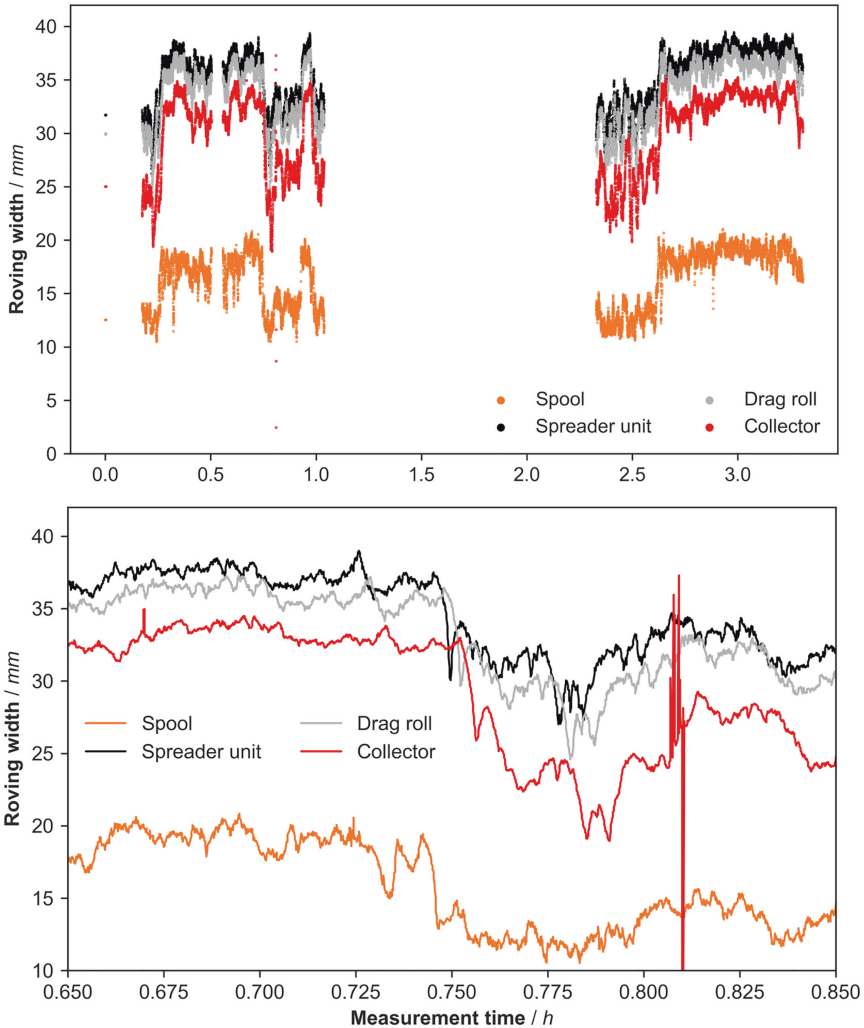


Fig. 6. Scatter plot of raw width data (*left*) and zoomed in (*right*).

Two runs split over 1 h each are shown. The variation of the data is visible, as well as larger steps in fibre width over the period of multiple minutes. It can be noticed that the measured fibre width shows two plateaus for each camera. The fibre width, therefore, has to vary around two width values. Zooming in further shows high accuracy even over small periods of time. Trends of the fibre width are represented by the expected time shift for each camera station. General trends, for example, a complete drop in fibre width, are represented accordingly. This confirms that the measurement system shows similar trends for all cameras even in shorter time frames, where a high signal-to-noise ratio is necessary.

Plotting a histogram of the roving widths measured for each camera allows the comparison of the measured widths, as seen in Fig. 7.

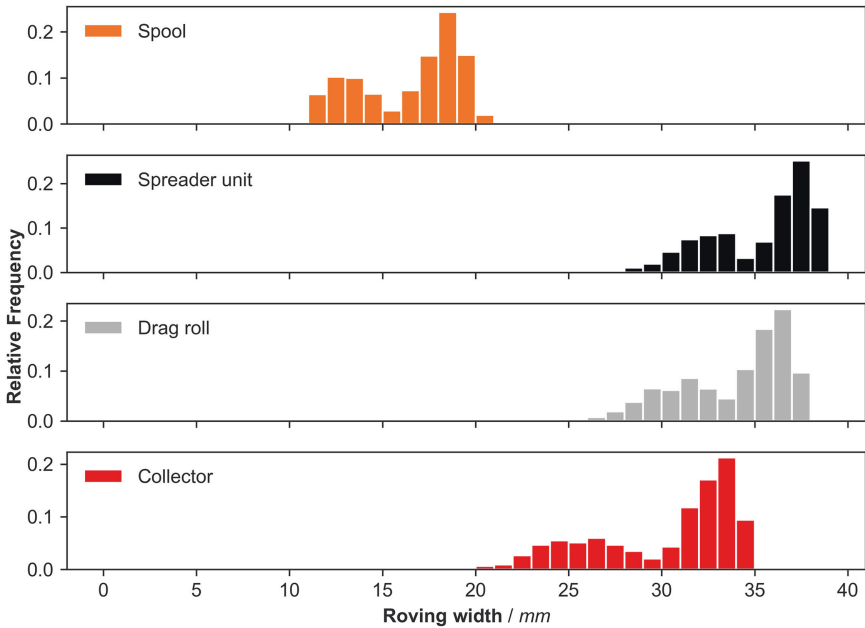


Fig. 7. Histogram of roving widths measured during single spool analysis.

It can be noticed that the measured roving widths are distributed bimodally, with a smaller and broader distribution at smaller roving widths. This distribution can be related to the drop in roving width between e.g., 2.4 h to 2.6 h and 2.6 h to 3.4 h and confirms the assumption of two plateaus of roving width. An explanation for this behaviour is the so-called “twist”. The roving, consisting of 50,000 aligned single filaments, has a rather low cohesion, only resulting from the sizing. If the roving was wound improperly, a height-increasing defect was produced, or the roving was wound too far over the edge of the layer below, the filaments slip past each other. This can be observed in Fig. 8.

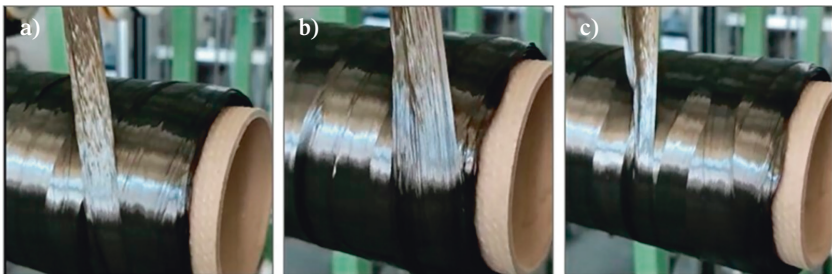


Fig. 8. Slipping of tow over spool edge during unwinding: **a** homogenous tension on roving in the middle of the spool, **b** slipping of roving over spool edge, **c** partial loss of roving tension.

In a), the roving is unwound properly, resulting in a homogeneous distribution of tension over the whole roving. In b), the roving is unwound over the edge of the spool, which leads to an uneven distribution of tension, which can be seen in c). The roving is only partly under tension and thus prone to twists. The phenomenon rearranges the filaments and changes the distribution of tension when the spool is unwound. The roving itself is constantly kept under tension during the processing, this leads to the propagation of the error throughout the complete process path. Defects seen over the duration of the experimental part of the project were the folding of the roving at the roving middle, the partly folding of the roving and also the twist of the roving producing a whole rotation. Some of these defects could be compensated by manually grabbing the roving at the spool and leading it oriented over the first bar in the spreader unit. As can be seen in the following pictures (see Fig. 9), the untwisted tow (b) was significantly broader without showing any gaps, in comparison to the twisted roving (a). Besides these effects it could be observed via several further rovings that the rovings often contain of twists already in their pristine state, which leads to fluctuations even from processing conditions at the manufacturer.

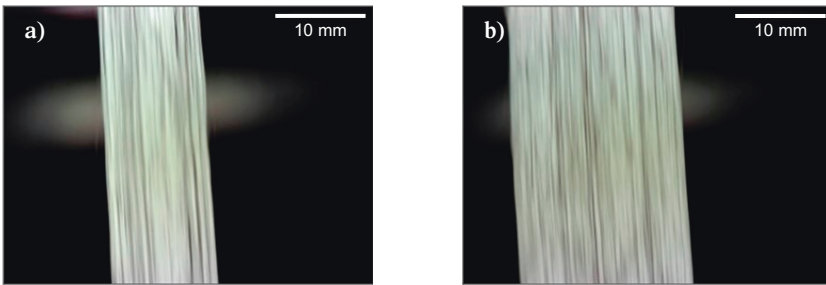


Fig. 9. Image of roving before entering the spreader unit (camera: “Spool”) during the analysis of a single roving **a** twisted roving and **b** untwisted roving.

This further leads to the assumption that the smaller and thinner part of the roving width distribution can be assigned to twists of the roving. To further analyze the actual measured roving width, all values below 15 mm width at the spool were neglected. The width distribution of the corrected data is shown in Fig. 10.

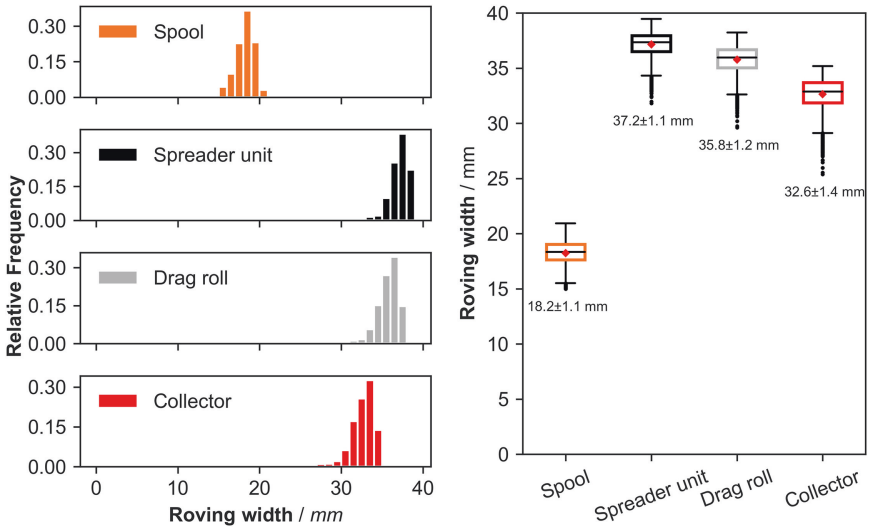


Fig. 10. Histogram and boxplot of corrected data (red dot: mean, line: median, value below: mean \pm standard deviation).

On the left side of Fig. 10, the histograms are plotted indicating a skewed distribution. This could be explained by the inaccurate neglect of data points deriving from “twisted” positions, due to the overlap of both distributions. However, Gizik [17] also described the non-normally distributed behaviour of fibre width after spreading, due to a maximum achievable width, but did not further go into detail. Similar behaviour of the roving could be assumed for the data displayed here. In Fig. 10, boxplots of the data in combination with their mean value (red dot), as well as their standard deviation, are written below the respective boxes. Comparing the three positions in the machine, the standard deviation increases after the spreading, while the mean roving width decreases. This could be explained by the mode of operation of the machine. Due to the roving width being related to tension, the highest tension is applied between the spreader unit and the drag roll, exactly where the “spreader unit” camera is installed. After the drag roll, the roving is led over multiple bars, where tension is lost, due to longer paths between the deflecting bars. Additionally, the winding unit regulates the tension of the rovings between the drag roll and winder using a pneumatic rod called “dancer”. Therefore, a variation in tension subsequently leads to a variation in width.

To determine the sample size n , the z -value of the standard normal distribution for a confidence level of 95%, equaling 1.96 was used. The standard deviation s was determined from the non-twisted and corrected data, selecting the highest deviation (Collector). A reasonable confidence interval for the width determination was selected to be ± 0.5 mm. Using Eq. (5),

$$n = \left(z^* \frac{s}{\Delta} \right)^2 \quad (5)$$

a sample size of $n = 31(30.11)$ was calculated. This means for further experiments, a sample size of at least 31 must be selected to determine the mean value for a confidence interval of ± 0.5 mm at a confidence level of 95%. Therefore, in the following experiments, 120 data points were measured per parameter setting over a length of 20 m. This allows the analysis of a longer roving sample and generates enough data to neglect failed measurements. After a correction of the data via time shift, the signals of the same part of the roving at different camera positions can be compared with each other. First, in Fig. 11 the roving widths at respective positions divided by the width of the unspread roving entering the spreader unit are plotted versus the absolute pristine width determined from camera 1 (“Spool”).

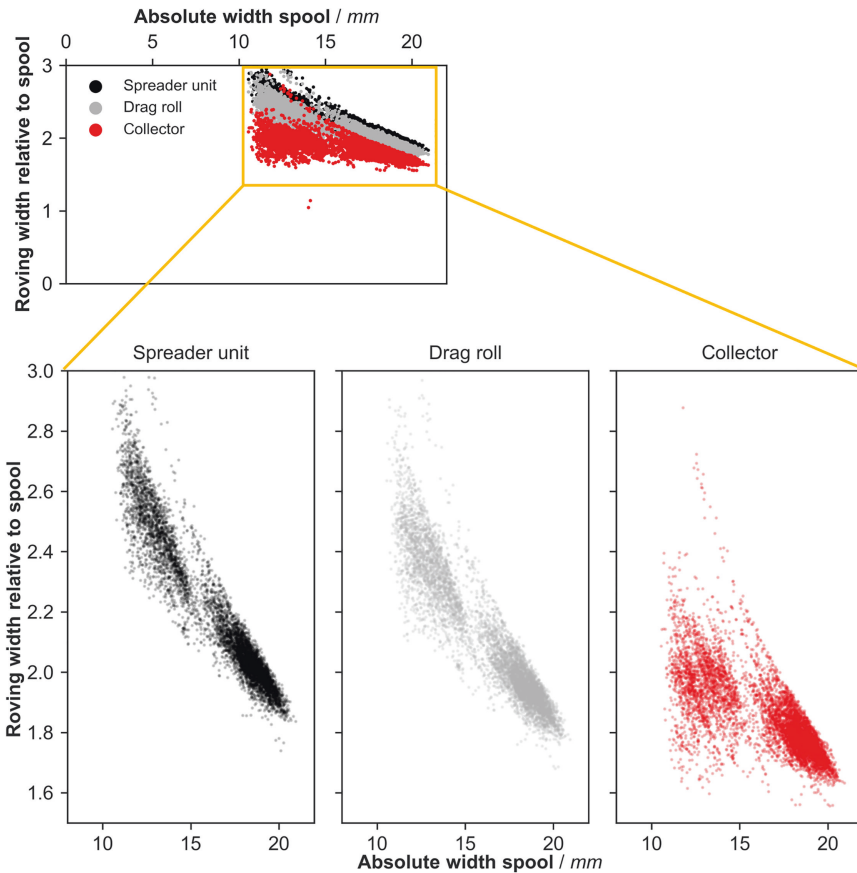


Fig. 11. Roving width increase versus absolute width at spool for “Spreader unit”, “Drag roll” and “collector” measurement positions.

It can be noticed that the measured data is split into two regions, as seen in the previously shown histogram (Fig. 7). The two data-clouds can be separated at the 15 mm mark for the entrance spool width. For the width measured at the collector, the shape of the data points is broader than the other two measurement positions, especially below the 15 mm mark. This could also be related to the loss in tension, seen before the tow is collected. Comparing both data clouds measured, the data points below 15 mm do not link to the cloud of data points above 15 mm in a way, comprehensible as a linear or curved line. This could indicate, that for both data sets a different spreading behaviour is seen. Further underlining the assumption of twists during the measurement.

Plotting the absolute width of the pristine roving at the entrance into the spreader unit versus its absolute width at the different stations of the machine (Fig. 12), the data represents more of a curved line. Also, the data points above and below 15 mm are more comprehensibly connectable, than in the relative representation.

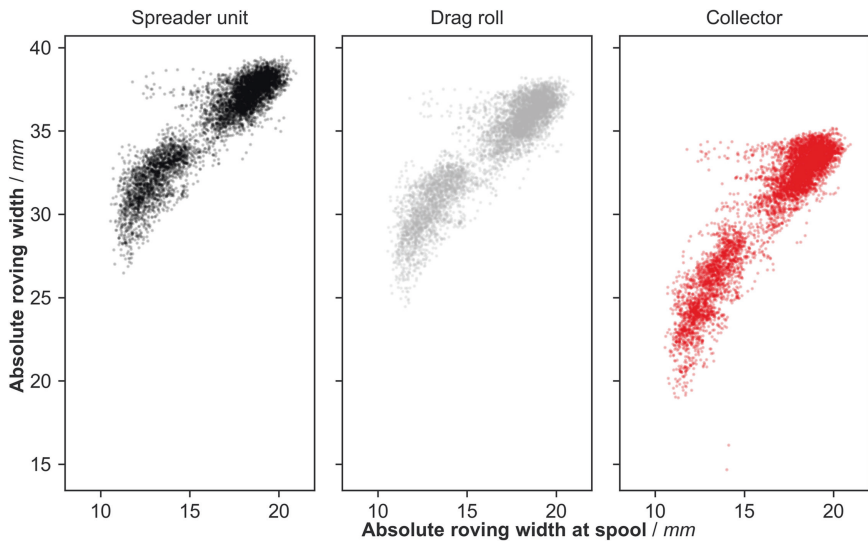


Fig. 12. Absolute roving width versus absolute width at spool for “Spreader unit”, “Drag roll” and “Collector” measurement positions.

The representation therefore does not allow to distinguish between the roving below and above 15 mm via the shape of the curve itself. Finally, it can be deduced, that the relative increase in tow width must be related to the width at the entry of the spool. Consequently, for following investigations the median of the collected data, specifically the increase in roving width related to the entry width of the roving is selected to quantify the spreading results. Evaluating the median reduces the influence of outliers or measurement errors and will be used in further into depth parameter studies.

4 Conclusion

4.1 Part A: Bayesian Optimization for Towpreg Processing

First, the BO showed tremendous potential for gaining rapid knowledge of the parameters that interact in the processing of towpreg material for composite-based hydrogen vessels. By choosing the right parameters to vary, a negative correlation between fibre volume content and towpreg width was found and quantified by a factor of -0.69 . Even though the target of a Towpreg width of 6.35 mm was not achieved, mainly due to the thin dry roving used, this BO approach is a powerful tool to learn more about the correlating parameters in a complex and multifunctional processing of such materials.

4.2 Part B: In-Situ Monitoring for Fibre Spreading

An in-situ monitoring tool to observe and analyse the fibre spreading process has been successfully developed. The new monitoring tool allows an in-depth characterisation of the evolution of the width of the spread rovings along several important stages of the spreading unit. It is possible to use this method as a quality control tool to distinguish between defects originating from the original state of the roving. It is especially important to distinguish the results of the spread rovings from defects such as twists that prevent sufficient spreading of the rovings used. This is especially important to obtain reliable results for future studies on the influence of parameters on the spreading process, as the spreading of twisted parts in the roving distorts the actual influence of the aligned process parameters. In the future, the developed monitoring tool can also be extended to detect imperfections along the spreading process, such as gaps in the spread roving, using machine learning tools.

Funding The Bayesian optimization approach was funded in the project “CryoFuselage” in the BayLu25 program under guidance of German Aerospace Center (DLR). Grants were given by the Regierung of Oberbayern with the Bavarian Ministry of Economic affairs, Regional Development and Energy (StmWi) with grant number LABAY108A.

The in-situ monitoring tool development for fibre spreading was funded in the project “InLineCon” in the LuFo VI-1 program under the guidance of German Aerospace Center (DLR). Grants were given by the Federal Ministry for Economic Affairs and Climate Action (BMWK) with grant number 20E1903B.

References

1. Züttel, A.: Hydrogen storage methods. *Naturwissenschaften* **91**(4), 157–172 (2004). <https://doi.org/10.1007/s00114-004-0516-x>
2. Pandita, S., et al.: Clean wet-filament winding – Part 1: design concept and simulations. *J. Compos. Mater.* **47**(3), 379–390 (Feb.2013). <https://doi.org/10.1177/0021998312440474>
3. Walker, G.: “Hydrogen storage technologies,” in *Solid-State Hydrogen Storage*, pp. 3–17. Elsevier, (2008). <https://doi.org/10.1533/9781845694944.1.3>

4. Lohse-Busch, H. et al.: "Report # ANL/ESD-18/12 Technology Assessment of a Fuel Cell Vehicle: 2017 Toyota Mirai," *US DOE -Energy Syst. Div.*, (2017) www.anl.gov
5. Ayakda, H., Ozan, S.: Aydiin, "HYDROGEN STORAGE TECHNOLOGIES" (2018) <https://doi.org/10.1533/9781845694944.1.3>
6. Shahriari, B., Swersky, K., Wang, Z., Adams, R.P., de Freitas, N.: Taking the Human Out of the Loop: A Review of Bayesian Optimization. *Proc. IEEE* **104**(1), 148–175 (Jan.2016). <https://doi.org/10.1109/JPROC.2015.2494218>
7. Agnihotri, A., Batra, N.: "Exploring Bayesian Optimization". <https://distill.pub/2020/bayesian-optimization/>
8. Li, C., et al.: Rapid Bayesian optimisation for synthesis of short polymer fibre materials. *Sci. Rep.* **7**(1), 5683 (Jul.2017). <https://doi.org/10.1038/s41598-017-05723-0>
9. Albuquerque, H., Rodrigo, Q., Rothenhäusler, F., Ruckdäschel, H.: "Designing formulations of bio-based, multi-component epoxy resin systems via machine learning", pp. 1–15. Submitt. Publisher
10. Nunna, S., Blanchard, P., Buckmaster, D., Davis, S., Naebe, M.: Development of a cost model for the production of carbon fibres. *Heliyon* **5**(10), e02698 (Oct.2019). <https://doi.org/10.1016/j.heliyon.2019.e02698>
11. Ennis, B. et al.: "Optimized Carbon Fibre Composites in Wind Turbine Blade Design," *Sandia Rep.*, no. November, (2019) <https://www.energy.gov/sites/default/files/2019/12/f69/SAND2019-14173-Optimized.pdf>
12. Friedrich, K., Almajid, A.A.: Manufacturing Aspects of Advanced Polymer Composites for Automotive Applications. *Appl. Compos. Mater.* **20**(2), 107–128 (Apr.2013). <https://doi.org/10.1007/s10443-012-9258-7>
13. Huang, C., et al.: Exploration relation between interlaminar shear properties of thin-ply laminates under short-beam bending and meso-structures. *J. Compos. Mater.* **52**(17), 2375–2386 (Jul.2018). <https://doi.org/10.1177/0021998317745586>
14. Cugnoni, J., et al.: Towards aerospace grade thin-ply composites: Effect of ply thickness, fibre, matrix and interlayer toughening on strength and damage tolerance. *Compos. Sci. Technol.* **168**, 467–477 (2018). <https://doi.org/10.1016/j.compscitech.2018.08.037>
15. Tonejc, M., Steiner, H., Fauster, E., Konstantopoulos, S., Schledjewski, R.: "A STUDY ON GEOMETRICAL PARAMETERS INFLUENCING THE MECHANICAL SPREADING OF FIBRE BUNDLES," in *20th International Conference on Composite Materials*, p. 10 (2015)
16. Vossen, C., Rene, G.: "Schlussbericht zu IGF-Vorhaben Nr. 18713 N Auto-Tow – Automatische Regulierung und Homogenisierung der Fasereigenschaften von Hochmodulfasergarnen," Aachen, (2018)
17. Gizik, D.: "Untersuchung der Verwendung von Heavy Tow Carbonfasern für Strukturbauteile in der Luft- und Raumfahrt," Universität Stuttgart, (2018) <https://www.dr.hut-verlag.de/978-3-8439-3911-9.html>
18. Otsu, N.: A Threshold Selection Method from Gray-Level Histograms. *IEEE Trans. Syst. Man. Cybern.* **9**(1), 62–66 (Jan.1979). <https://doi.org/10.1109/TSMC.1979.4310076>



3D Material Characterization and Determination of Out-Of-Plane Properties Based on Digital Image Correlation

Nikolas Korte¹(✉), Jens Bold², Alexander Hüls³, Sascha Ort³,
Bernd Westerhoff³, Bruno Musil¹, and Philipp Höfer¹

¹ Universität Der Bundeswehr München, 85577 Neubiberg, Germany
{nikolas.korte,bruno.musil,philipp.hoefer}@unibw.de

² Boeing Deutschland GmbH, 80805 Munich, Germany
jens.bold@boeing.com

³ VORWERK AUTOTEC GmbH & Co. KG, 42287 Wuppertal, Germany
{a.huels,s.ort,b.westerhoff}@vorwerk-automotive.de

Abstract. In this work, an approach for a 3D material characterization based on experiments is presented. Experimentally determined material properties are used to define a 3D compliance matrix for a more accurate simulation of the material's behavior. This includes out-of-plane properties, e.g. transverse contraction in thickness direction. To gain complete stress-strain curves in material testing, Digital Image Correlation (DIC) is used for strain measurement. Through the usage of a biplane DIC-setup, out-of-plane measurements including strains in thickness direction are possible. Unidirectional endless fiber composites and short fiber plastic were tested in tension and compression to determine in-plane and out-of-plane material properties, each for two material orientations.

Simulations of the short fiber plastic injection molding process lead to fiber orientations over the thickness, which are compared to computer tomographic (CT) scans. With adjusted distribution of fiber orientations, simulations of mechanical behavior in all three directions are presented and compared to test data.

Keywords: 3D Material Characterization · Digital Image Correlation · Out-of-plane Properties · Strains in Thickness Direction · Composites · CFRP · Short Fiber Plastic

1 Introduction

Composite parts have a high potential in weight saving for aerospace as well as automotive applications. In order to exploit this potential, a precise knowledge of the material's behavior is necessary. For a complete description of the material behavior, various material properties must be determined experimentally in different material directions and under different test methods. Some of these materials values, like

out-of-plane properties, are often only assessed based on literature or very thick laminates. For orthotropic materials, strains can be correlated with the stress vector and a 3D compliance matrix within a linear-elastic region, see Eq. 1 [1]. Here, the compliance matrix contains 12 engineering constants, that must be determined in experiments.

$$\begin{pmatrix} \varepsilon_1 \\ \varepsilon_2 \\ \varepsilon_3 \\ \gamma_{23} \\ \gamma_{31} \\ \gamma_{12} \end{pmatrix} = \begin{bmatrix} \frac{1}{E_1} & -\frac{\nu_{21}}{E_2} & -\frac{\nu_{31}}{E_3} & & & \\ -\frac{\nu_{12}}{E_1} & \frac{1}{E_2} & -\frac{\nu_{32}}{E_3} & & & 0 \\ -\frac{\nu_{13}}{E_1} & -\frac{\nu_{23}}{E_2} & \frac{1}{E_3} & & & \\ & 0 & & \frac{1}{G_{23}} & 0 & 0 \\ & & & 0 & \frac{1}{G_{31}} & 0 \\ & & & 0 & 0 & \frac{1}{G_{12}} \end{bmatrix} \begin{pmatrix} \sigma_1 \\ \sigma_2 \\ \sigma_3 \\ \tau_{23} \\ \tau_{31} \\ \tau_{12} \end{pmatrix} \quad (1)$$

For in-plane properties (1- and 2-direction), standard tests are well established for orthotropic materials like unidirectional or woven endless fiber reinforced plastics, shown in Fig. 1.

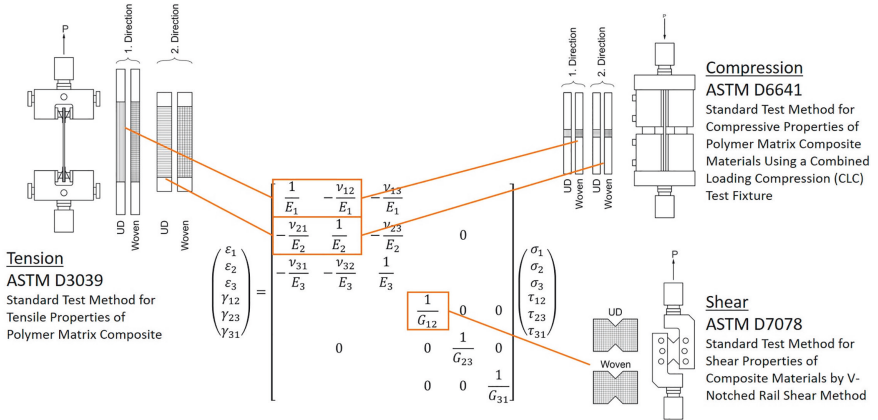


Fig. 1. 3D compliance matrix of polymer matrix composite including standard test methods for each material property

If a unidirectional laminate is regarded as a layup of individual plies in which the fibers with constant cross-section are arranged exactly parallel and have a uniform packing density, it is referred to as an ideal ply. This idealization also includes complete fiber-matrix adhesion, as well as the absence of pores, etc. [2].

For such ideal layers of unidirectional laminates, it is then considered to have transversal isotropic properties due to the same fiber architecture in 2- and 3-direction. This idealization leads to a reduction of the orthotropic compliance matrix in Eq. 1, where $E_3 = E_2$, $\nu_{31} = \nu_{21}$ and $G_{13} = G_{12}$ [1, 2].

For short fiber reinforced plastic, where the direction of the fiber is changing through the thickness, necessary values and allowable cannot be directly determined from standard tests because not a single direction like in the coupon test for endless fibers is tested. This corresponds to element tests for endless fibers. Additionally, for all types of fibers, the values and allowable related to the third direction are generally not measured in standard testing.

Standard tests, based on flat specimens in tension and compression were investigated with the use of 3D Digital Image Correlation (DIC) strain measurement. The 3D DIC not only offers complete stress-strain curves [3] which is necessary to use advanced failure criteria and material models in simulation. Beside strain values in in-plane, the authors present strain measurements in the out-of-plane (thickness) direction. With these test data, it is now possible to determine Poisson's ratios for different directions (ν_{12} , ν_{13} , ν_{21} , ν_{23}) and to compare dependencies of the material direction. In this work, different materials were investigated: short glass-fiber reinforced polyamide 6 and unidirectional carbon fiber laminate.

Simulations with standard and extended material values were performed for the short fiber plastic and compared to the experiments.

2 Experimental Work

2.1 Strain Measurement Using Digital Image Correlation

In this work, strain measurement is performed by Digital Image Correlation (DIC). To gain thickness information during testing, e.g. strains in thickness direction, a biplane DIC-Setup is used. Therefore, the two surfaces of each specimen are observed with two or three cameras, so that both surfaces can be mapped in 3D using the DIC-software (ISTRA 4D, Dantec Dynamics). Figure 2 shows a schematic illustration of the DIC-Setup. All specimens are prepared with a random speckle-pattern for a grey-value estimation performed by the DIC-Software. Each surface is separated into several facets for which displacement und strain values are calculated. Generally, the distance of these two surfaces represents the specimen's thickness. In-plane strains are calculated by the facet's deformation, while out-of-plane strains are calculated by the relative distance change of two facets, lying oppositely on the two mapped specimen surfaces. In this work, all calculated strains are mean values of several facets in a rectangular evaluation field of about 5×3 mm (length x width), depending on the specimens.

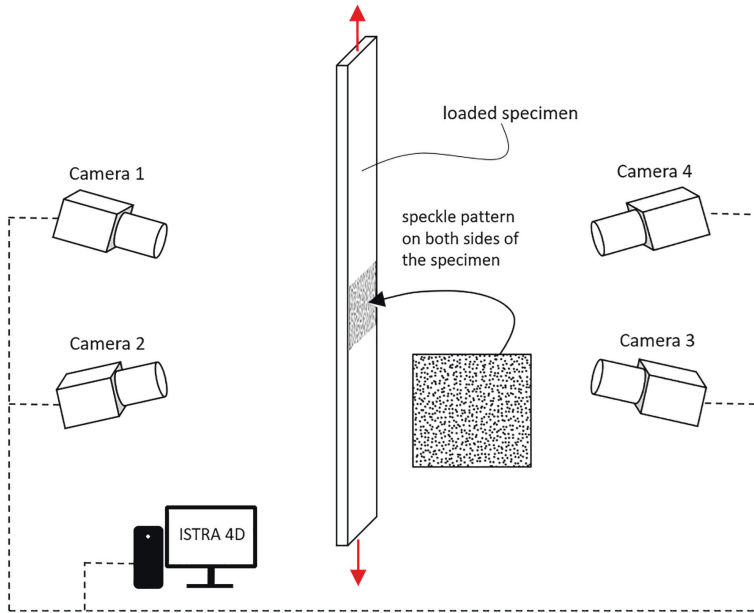


Fig. 2. Schematic illustration of a biplane DIC-Setup

2.2 Specimens and Test Device

An overview of tested materials, specimens and test methods in this work is shown in Table 1. All tests were driven on a Zwick Z150 testing machine with a speed of 1 mm/min.







Table 1. Overview of tested specimens

Material	Test method	Standard (acc. to)	Dimensions [mm]	Thickness [mm]	Number of specimens	Fixture / Grip
CFRP UD-Plain	Tensile 0°	ASTM D3039	250 × 15	2	5	Hydraulic grip
	Tensile 90°		225 × 25	2	5	Hydraulic grip
	Compression 0° and 90°	ASTM D6641	140 × 13	2	4 and 4	Hydraulic Composites Compression Fixture
Short Fiber Plastic	Tensile in- and crossflow		Dogbone 140 × 6	3	3 and 3	Wedge screw grip
	Compression in- and crossflow		Dogbone 140 × 6	3	7 and 8	Hydraulic Composites Compression Fixture

Unidirectional Carbon Fiber Plastic (CFRP-UD). Specimens were cut with the use of a diamond saw or milled out of a plate using diamond coated milling tools. According to ASTM D3039 and ASTM D6641, the specimen's dimensions were 250×15 mm in 0° fiber direction (tensile) and 225×25 mm in 90° fiber direction (tensile) with a free length of 125 mm, as well as 140×13 mm in 0° and 90° fiber direction (compression) [4, 5].

Short Fiber Plastic. Plates of 3 mm thickness were mold-injected with short glass fibers and polyamide 6 matrix. After injection, specimens were milled in inflow and crossflow direction, using the same dogbone geometry for tension and compression testing. Before testing and application of the speckle pattern, the specimens are dried in an oven at slightly elevated temperature for several days until relative weight loss is nearly asymptotic.

Table 2. Tested specimens

Test method	Specimen
Tensile CFRP UD 0°	
Tensile CFRP UD 90°	
Compression CFRP UD 0°	
Compression CFRP UD 90°	
Tensile Short Fiber Plastic	
Compression Short Fiber Plastic	

2.3 Test Results

In the following stress-strain diagrams, the colors of the single curves are according to the shown cartesian coordinate system, where the x-direction corresponds to the loading direction, whereas the y-direction is orthogonally on the specimen's surface. The z-direction is directed towards the thickness and out-of-plane direction.

Due to high noise in the DIC calculated strains in z-direction, this data is filtered by a moving average over nine data points, which was sufficient for an average curve. By the use of an additional camera aligned on the specimen's side to perform an additional 2D-DIC measurement, the measurement noise in z-strains is lower compared to the calculation through the relative thickness change of the two mapped surfaces. Therefore, no additional moving average was performed here. This setup was used only in one test series (tensile CFRP UD 90°). Material properties are calculated using linear regression between datapoints of $\varepsilon_{x,1} = 1000 \frac{\mu\text{m}}{\text{m}}$ and $\varepsilon_{x,2} = 3000 \frac{\mu\text{m}}{\text{m}}$ of strain in load direction. For every material and both orientations (0° and 90° , or inflow and crossflow) mean values and their standard deviation are presented. Material properties

were calculated as follows, using a linear regression approach for loading in 1-direction (CFRP UD 0° or short fiber plastic inflow):

$$\nu_{12} = -\frac{\Delta\varepsilon_y}{\Delta\varepsilon_x} \quad (2)$$

$$\nu_{13} = -\frac{\Delta\varepsilon_z}{\Delta\varepsilon_x} \quad (3)$$

The Poisson's ratios ν_{21} and ν_{23} represent the transverse contraction of the material loaded in 90° or crossflow direction with the same quotient of local strain differences. In this work, applied tensile forces result in positive stresses and positive strains in axial direction, whereas applied compressive forces are defined as negative resulting stresses and strains in axial direction.

Tensile CFRP UD 0° and 90° . Stress-strains curves of the tensile tested CFRP specimens are shown below. In Fig. 3a, strains in x-direction (red curves) show a clear, nearly linear curve for the 0° specimens. On the other hand, z-strains (blue curves) show a high noise in the data, which was filtered as described above. Some specimens show positive z-strains at the beginning of the test, whose possible cause has to be further investigated (e.g. uncertainties in DIC z-strain calculation, gripping-effects or other). Fig. 3b shows the stress-strain curves of 90° tensile testing, where an additional camera was faced towards the small specimen's plane. Hereby, an additional 2D-DIC measurement was done, which shows less measurement noise of z-strains. An offset of the single curves of the z-strains can be observed, which again has to be investigated in the near future.

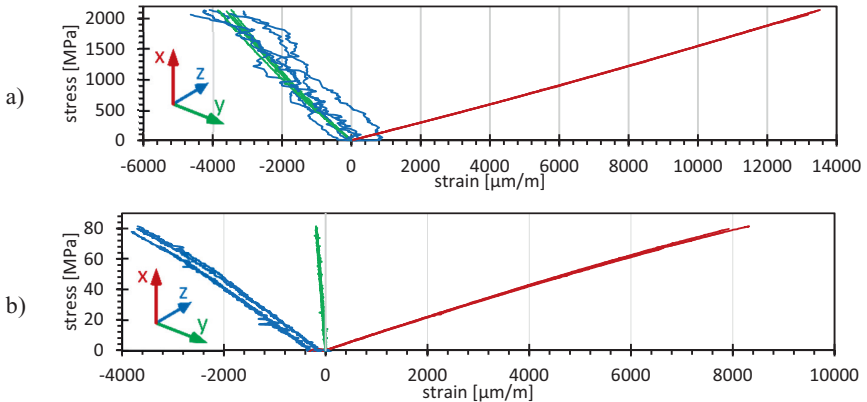


Fig. 3. Stress-strain curves of CFRP UD **a** 0° and **b** 90° tensile testing

Compression CFRP UD 0° and 90° . Strains in x-direction of compression tests are shown as an average of front- and backside at each timestep of each specimen in Fig. 4a for 0° and b for 90° specimens. Again, strains in z-direction of the 0° specimens show an elevated noise in the measurements. The noise of strains in z-direction

in Fig. 4b seems to be lower, but due to the high strain values until rupture, the noise is only poorly visible in this diagram.

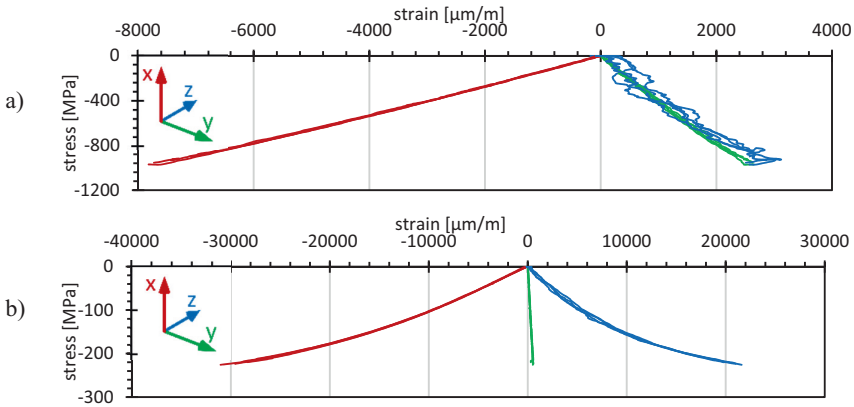


Fig. 4. Stress-strain curves of CFRP UD **a** 0° and **b** 90° compression testing

Determined Material Properties of CFRP UD 0° and 90°. In Fig. 5, the determined material properties based on the previously presented test data is shown. Figure 5a shows material properties for the 0° tensile and compression specimens, Fig. 5b for the 90° tensile and compression specimens. Comparing one material direction for different load direction (tension and compression), stiffness and Poisson’s ratios are different. Major differences in stiffness and transverse contraction, e.g. E_1 and E_2 , or ν_{12} and ν_{21} are based on the unidirectional carbon fiber lying either in load direction or orthogonally to it.

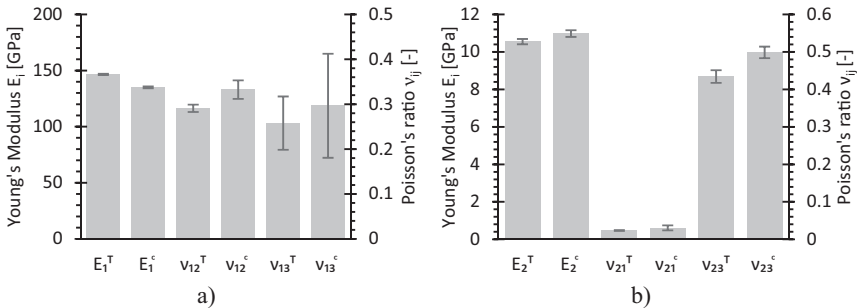


Fig. 5. Determined tension and compression material properties of CFRP UD **a** 0° and **b** 90°

Calculated values for Poisson’s ratios including the third direction show partly high standard deviations due to measurement noise in the calculated z-strains.

Nevertheless, differences between ν_{13} and ν_{23} are observed, which may indicate, that these material properties depend on the load direction for this material. Also, these values are different from values of in-plane transverse contraction ν_{12} and ν_{21} .

Tensile Short Fiber Plastic Inflow and Crossflow. Test data of the second material tested is shown in the next diagrams. Again, two directions of the material are con-sidered. In Fig. 6, tensile test data of a) inflow and b) crossflow direction of the short fiber plastic is presented. Ultimate strains in load direction (x) for the inflow direction specimens are lower but ultimate stresses are higher compared to crossflow direction specimens. In both diagrams, it is clearly shown that strains in y- and z-direction differ from each other.

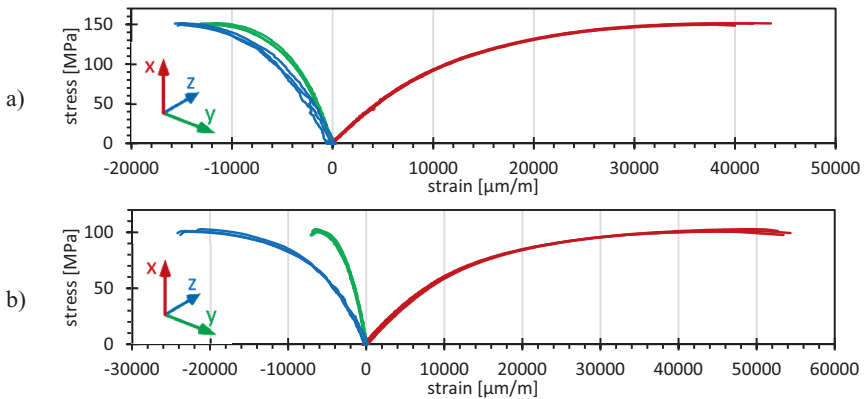


Fig. 6. Stress-strain curves of short fiber plastic **a** inflow and **b** crossflow tensile testing

Compression Short Fiber Plastic Inflow and Crossflow. In compression tests, strain in load direction (x) is averaged from the front- and backside of the specimen.

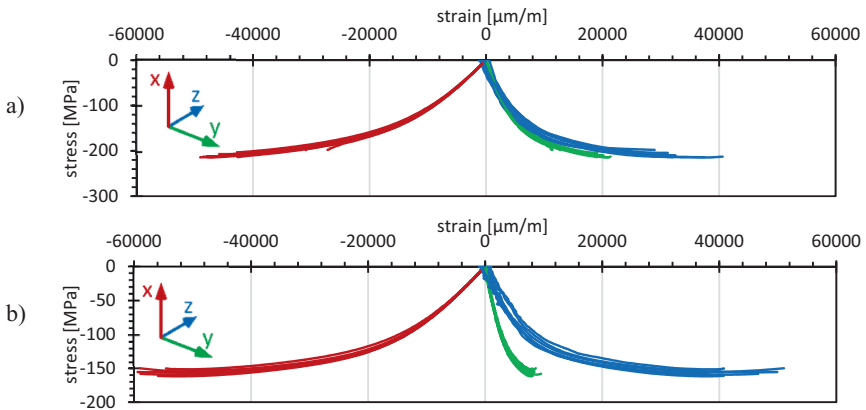


Fig. 7. Stress-strain curves of short fiber plastic **a** inflow and **b** crossflow compression testing

Qualitatively, differences of ultimate strains and stresses in the single directions are similar to tension tests.

Determined Material Properties of Short Fiber Plastic Inflow and Crossflow.

With the data of tension and compression tests shown above, material properties were calculated. Figure 8a shows material properties for the inflow specimens, Fig. 8b for the crossflow specimens. For both material orientations, compression stiffness is higher than tension stiffness. Due to the expected different fiber orientations of the materials, stiffness values are different comparing the material orientation. Here the inflow specimens show a higher Young's modulus.

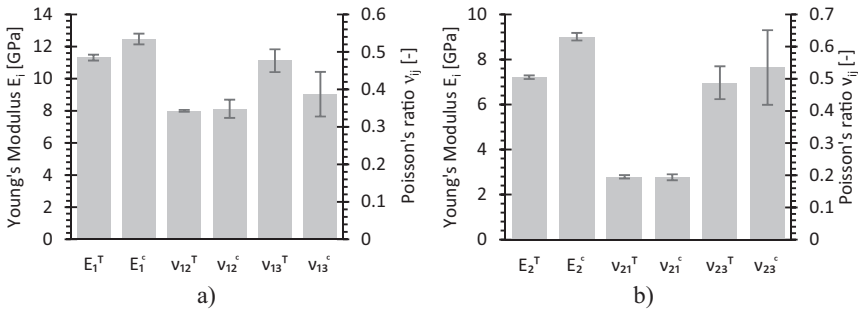


Fig. 8. Determined tension and compression material properties of short fiber plastic

Also, the Poisson's ratio ν_{12} shows higher values than ν_{21} for the crossflow specimens indicating the higher degree of fiber orientation in inflow direction. Standard deviations in Poisson's ratio containing the third direction (ν_{13} , ν_{23}) are elevated again, probably due to higher measurement noise in z-strains.

3 Simulation

3.1 Injection Molding Simulation

In order to capture the fiber orientations of the short fiber plastic, the manufacturing process of plates were simulated. The plate geometry was simulated by means of the filling simulation software CadMould. The plates of thickness 3 mm are the basic material for the later milled testing samples. With the target of getting a realistic output, the relevant areas including the thermal system of the injection tool were replicated. Other parameters of the simulation have been chosen according to measured data of the real process. The fiber orientation result is decomposed into layers along the thickness direction. Due to symmetry, only one half of the thickness is regarded. Here, layer 1 corresponds to the inside layer starting from the symmetry plane and layer 5 to the outside layer of the plate (see Fig. 9).

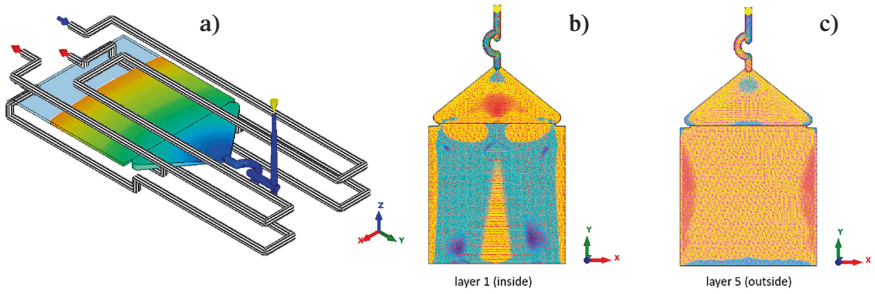


Fig. 9. Fill simulation: **a** layout, **b** layer 1 (*inside*) and **c** layer 5 (*outside*)

In-between there are further 3 layers as results available. Furthermore, the orientations are determined in two directions across the cross section as inflow and crossflow (see Fig. 10). Due to 2.5D fill simulation method the third direction is only a constant value. The fiber orientation of the plate model was then exported as a relevant result for further investigations.

Based on this software export, the fiber orientations were investigated layer-wise along the plate thickness and compared with measurements of the manufactured plates using CT scans. The simulation results of the fiber orientations are partly different from the measured values (see Fig. 11). A first comparison with the measured CT scan shows that the CadMould simulation results sometimes deviate quite significantly and by themselves are not sufficient to meet the reality. Thus, further investigations must follow to identify the reasons for that and to adjust the setup for improving the forecast of fiber orientation.

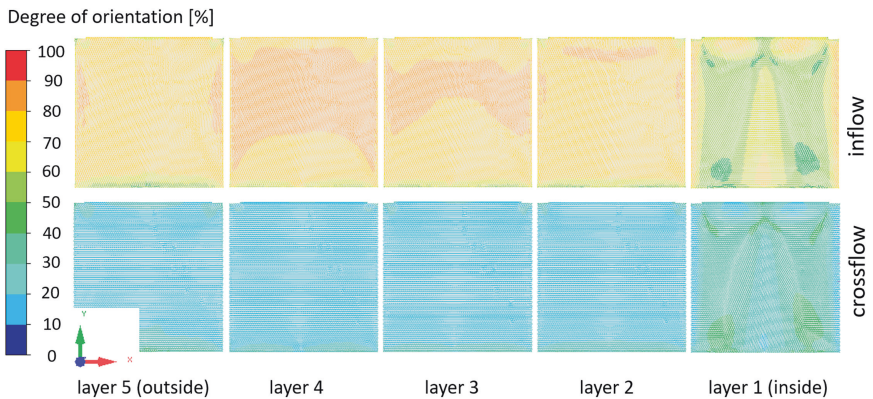


Fig. 10. Fiber orientation per layer

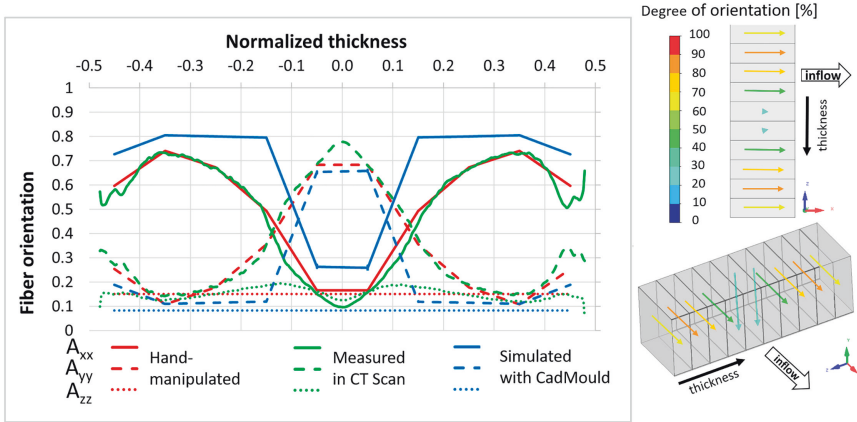


Fig. 11. Fiber orientation across the thickness

3.2 Mapping

For making the fiber orientation output usable for FEA, the exported data need to be converted and transmitted to the FEA mesh. For this, the software tool CONVERSE was used, which provides such an interface between CadMould and Abaqus.

The fiber orientation data were mapped to the final mechanical model. However, the mapped result could not be accepted without further processing due to the deviation in the fiber orientation. Because of the discrepancy in the CadMould simulated results, the mapped output needed to be manipulated, which was done manually by scripting because of less complexity of the sample mesh. The simulation model is still quite manageable in terms of complexity and therefore it was possible with a simple scaling approach to manually edit the fiber orientation definition in the areas to be considered.

Furthermore, the anisotropic/orthotropic material was calibrated based on the sample test results in tension and the measured fiber orientation distribution over the thickness. For this, CONVERSE offers the possibility of carrying out a material calibration based on the tensile test results. Here the material has been adjusted to tension with the appropriate assignment of the fiber orientation via the sample thickness for the first main direction.

3.3 Finite Element Analysis

In a third step the generated files were used for FEA. By means of Abaqus solver the sample geometry was simulated by loading in tension and in compression. The material calibration was done by considering the tensile measurements of test samples and the CT scanning measurements fiber orientation distribution across the thickness. Therefore, the behavior of the sample simulation in loading direction met sufficiently the measured real values taken from DIC (see Fig. 12).

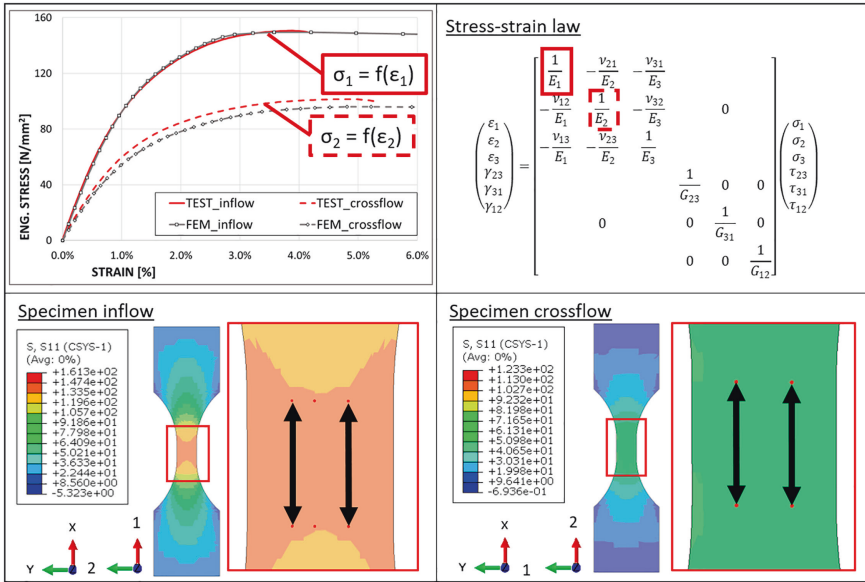


Fig. 12. Tensile behavior of inflow and crossflow samples

3.4 Postprocessing

In post-processing, the technical strain in the different spatial directions and the stress of the virtual sample were evaluated via displacements of the corresponding pairings of nodes. The DIC provides additional technical strain values in second direction perpendicular to loading direction on the sample surface which were compared with the FEA generated results. In the relevant area, the strain values were calculated based on the displacement of node pairs in all the directions and for all the directions as well as the stress is plotted over those strain values. The transverse contraction in-plane is also shown in Fig. 13.

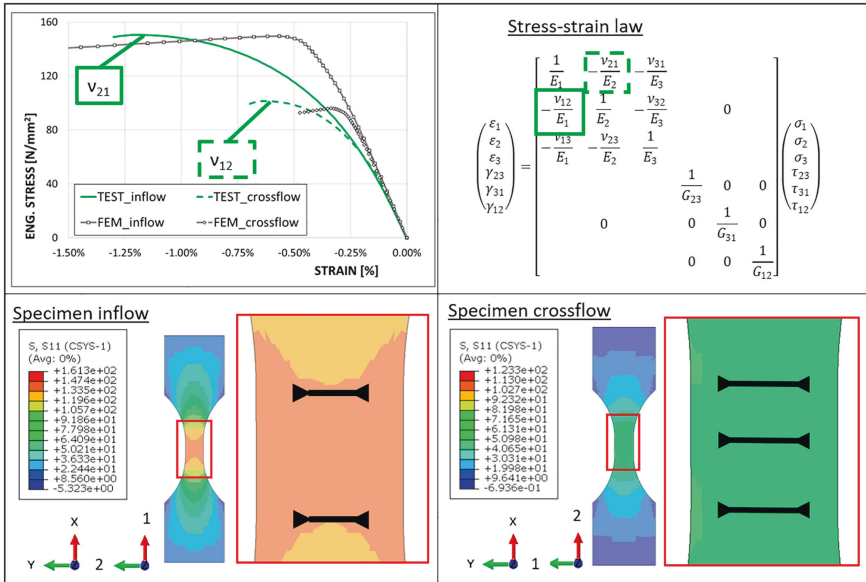


Fig. 13. Transverse contraction in-plane by loading in tension

For the FEM, however, further material data are often missing for a sufficient description of the anisotropic (orthotropic) behavior of a multiphase material like this. However, the DIC opens new ways of recording the transverse contraction in the thickness direction of the sample. This was also compared with the sample behavior in the simulation (see Fig. 14).

The potential of the material is not fully exploited, when loaded in compression. The DIC can also be used to measure strains under compression loads, especially where dimensional limitation does not allow the use of mechanical extensometer. Additionally, buckling effects need to be monitored and imperfection needs to be considered and evaluated. The compression test results of the specimens were compared with the FEM, too (see Fig. 15).

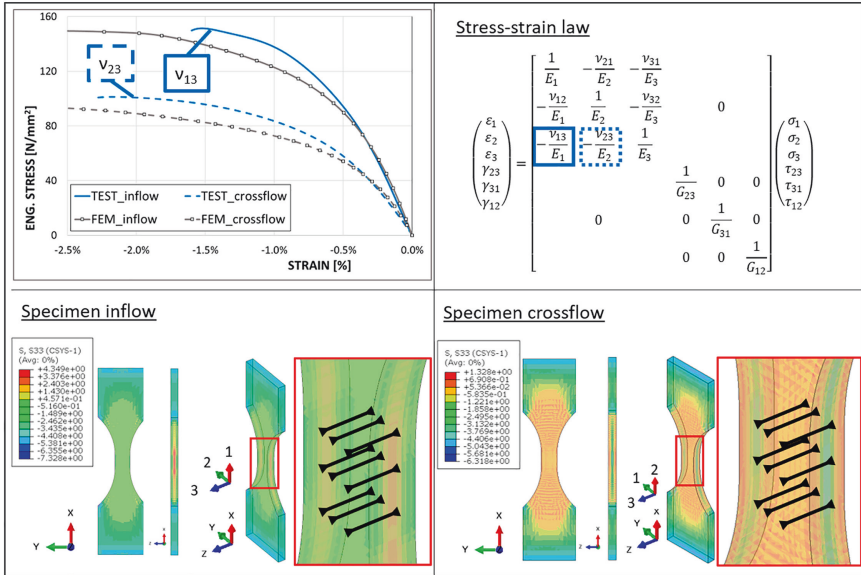


Fig. 14. Transverse contraction out-of-plane by loading in tension

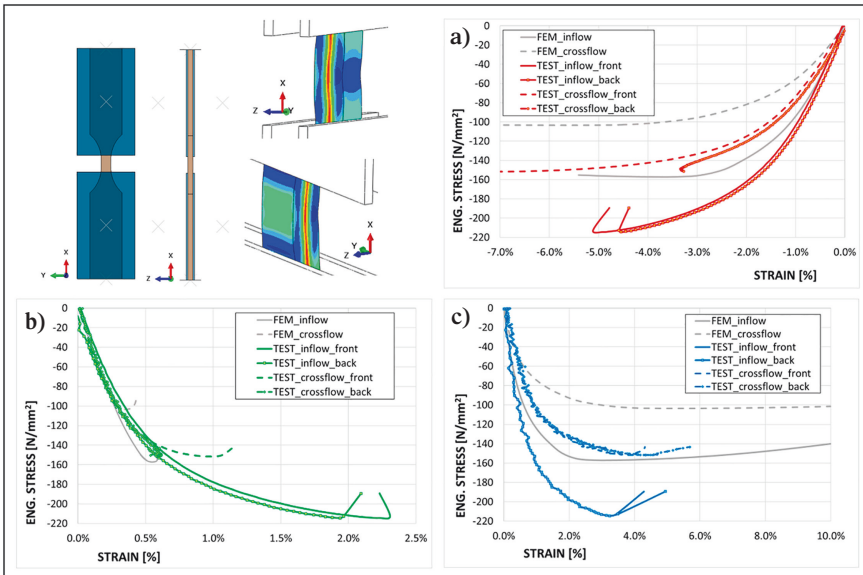


Fig. 15. Compressive behavior of inflow and crossflow samples **a** in loading direction, **b** transverse contraction in-plane and **c** transverse contraction out-of-plane

4 Summary and Outlook

Two materials, unidirectional CFRP and short fiber plastic, were tested in tension and compression in two directions. With the use of digital image correlation, complete stress-strain curves were created with strains in in-plane and out-of-plane direction. For the investigated materials, material properties like Young's modulus and Poisson's ratio were calculated based on these experiments, including transverse contraction in thickness direction.

With numerical methods, the short fiber plastic was simulated, starting from manufacturing process to generate the distribution of fiber orientations. Computer tomographic scans were compared to simulations and used to validate the fiber directions. Adjustments were done to the orientations to have a more correct representation which were then implemented in a material model for FEM. Here, the material behavior in tension and compression loading, including the thickness direction was simulated and compared to experiments.

Complete stress-strain curves, which are necessary for smarter testing using standard test results on coupon level as well as digital twins, can be determined for unidirectional and woven endless fiber reinforced plastics. The substitution of classical strain gauges by digital image correlation allows to measure the third direction Poisson's ratio free of charge, in case of the usage of biplane DIC setup. Additionally, a video is available to investigate the failure mode in more detail.

For short fiber reinforced plastics, material values and allowable cannot be determined directly from standard tests because the fibers have different orientations through the thickness of the specimen. This is similar to element tests for endless fiber reinforced plastics. Based on tension, compression and shear tests, the material values and allowable for a single direction short fiber reinforced material can be determined. According to Fig. 16, the 81 values and allowable needed for a complete 3D characterization of the short fiber reinforced plastic can be determined using results from 320 standard tests at three temperatures and the use of numerical methods in standard software.

A validation – comparison between higher level tests and simulation – will be done in a next step. Infill simulation using different software tools is planned and will be compared to CT-scans. To reduce testing, ALTAIR Multiscale Designer will be used to simulate fiber-matrix behavior on a micromechanical level and will be part of smart testing for the future. Further investigations will be done for the third direction measurements including different materials and the reduction of noise in DIC z-strain measurements.

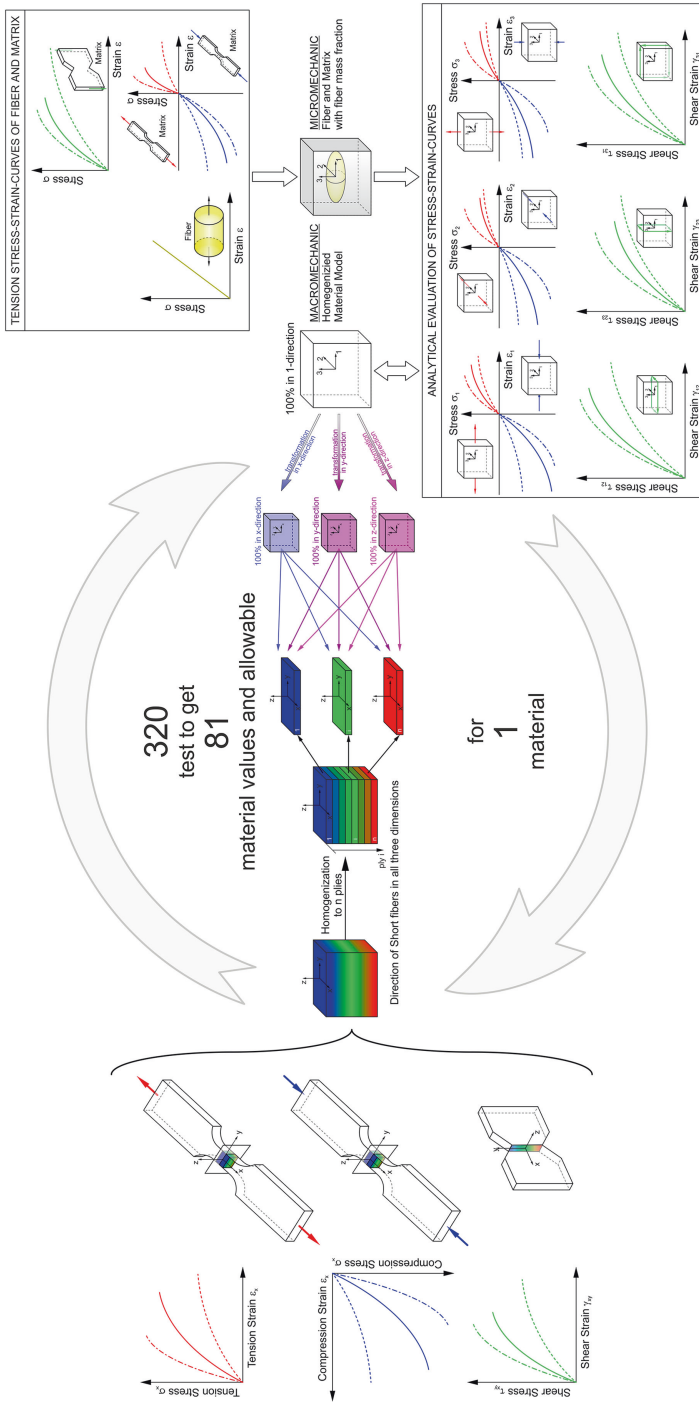


Fig. 16. Complete 3D characterization of short fiber reinforced plastic

Acknowledgement. The research was done in the project RICA (*Reduction of the CO₂-emission by increasing the material utilization using the 3D digital twin*), within the program Technologietransferprogramm Leichtbau (TTP-LB), which is funded by the German Federal Ministry for Economic Affairs and Climate Action. The consortia involved the Universität Der Bundeswehr München, the test house Applus+BKW, the material manufacturers Teijin and Henkel, the aircraft manufacturer Boeing, Altair for numerical simulation methods, Vorwerk Autotec for automotive applications and the small and medium enterprise Eckerle for tooling design and tooling manufacturing.

Supported by:



Federal Ministry
for Economic Affairs
and Climate Action

on the basis of a decision
by the German Bundestag

References

1. Jones, R.M.: Mechanics of composite materials, 2nd edn. CRC Press, Taylor & Francis Group, Boca Raton, London, New York (1999)
2. Schürmann, H.: Konstruieren mit Faser-Kunststoff-Verbunden, 2. Aufl. Springer, Berlin (2007)
3. Korte, N., Bold, J., Höfer, P.: Substitution of Strain Gauges by Optical Strain Measurement for Standard Test Methods of Composite Specimens and Introduction of a New Biaxial Test-Fixture. Proceedings of the Munich Symposium on Lightweight Design **2021**, 13–24 (2022)
4. ASTM International: Test Method for Tensile Properties of Polymer Matrix Composite Materials. ASTM D3039/D3039M-17, West Conshohocken, PA, United States (2017)
5. ASTM International: Standard Test Method for Compressive Properties of Polymer Matrix Composite Materials Using a Combined Loading Compression (CLC) Test Fixture. ASTM D6641/D6641M-16, West Conshohocken, PA, United States (2016)



Influence of Plasma Coating Pretreatment on the Adhesion of Thermoplastics to Metals

Wikentij Koshukow¹(✉), Alexander Liebsch¹, Jan Wippermann²,
Björn Kolbe³, Robert Kupfer¹, Juliane Troschitz¹, Magnus Buske³,
Gerson Meschut², and Maik Gude¹

¹ Institute of Lightweight Engineering and Polymer Technology – ILK,
Technische Universität Dresden, Dresden, Germany
{wikentij.koshukow, alexander.liebsch, robert.kupfer,
juliane.troschitz, maik.gude}@tu-dresden.de

² Laboratory for Material and Joining Technology – LWF, Paderborn
University, Paderborn, Germany
jan.wippermann@lwf.uni-paderborn.de,
meschut@lwf.upb.de

³ Plasmamatreat GmbH, Steinhagen, Germany
{bjoern.kolbe, m.buske}@plasmamatreat.de

Abstract. Combining metal sheets and thermoplastics into hybrid structures is a promising approach to design geometrically complex and highly durable lightweight parts. To ensure an economical production of these hybrid structures, the metal component can be overmoulded with a thermoplastic compound in an injection moulding process. Due to the dissimilarity of the materials, a suitable pretreatment of the metal sheet is required to ensure proper adhesion of the components. Plasma technology can be used to apply an adhesion promoter based on a precursor onto the metal surface. Furthermore, plasma pretreating can be integrated into the automated process chain. Additionally the metal sheet has to be preheated to activate the adhesion promoter. Besides the preheating temperature of the metal insert, the process parameters of the precursor application and the injection moulding process influence the adhesion strength of the joint between the metal and the thermoplastic. To identify the process window for sufficient adhesion, parameter studies based on a design of experiments are carried out. The manufactured hybrid test specimens are tested according to DIN EN 1465 for mode I shear strength. Additionally, the failure mode is evaluated by optical analysis. As a result, a correlation between the process parameters of plasma pretreatment and the structural property shear strength is derived.

Keywords: Hybrid composite structures · Adhesion · Shear strength · Plasma pretreatment · Overmoulding

1 Introduction

The EU confirms the zero CO₂ road mobility target by 2035, for which reason only zero-emission vehicles - preferably battery-electric or hydrogen-powered vehicles - will receive new registrations from 2035 [1, 2]. With this sign of transformation, the demands on the resource efficiency of individual mobility increase. Lightweight engineering, especially by innovative lightweight design, new types of materials and material combinations can make a significant contribution to achieving this aim [3, 4]. Here, multi-material components made of metal, endless fibre-reinforced plastics (FRP) and injection moulding compounds present a promising approach.

Metal substructures are predestined for areas subjected to multiaxial loads; the areas with directional load paths can be specifically reinforced with FRP [6]. The combination with the injection moulding process allows additional functionalisation, for example with screw domes, snap-in hooks or stiffening ribs combined with economic process times.

The combination of thermoplastic FRP and injection moulding compound into hybrid structures has been extensively researched in recent years [6–10]. As a result, customised, multifunctional and geometrically complex lightweight structures can be manufactured by the combination of FRP and injection moulding technology.

The main challenge in the development, production and use of hybrid structures is the design of the interface between the different materials. If a material bond is to be created between the FRP and the injection moulding compound, the FRP must always be pretreated, usually by heating it to above the melting temperature of the matrix [11]. The bonding strength between the thermoplastic components is achieved by the interdiffusion of the molecules and depends in particular on the type of matrix polymers, the temperatures of the FRP and the injection moulding compound as well as mould temperature [10, 12–16]. In addition to the process parameters, the geometry of the rib base also influences the load-bearing capacity. For instance, numerical and experimental studies have shown that for the same rib geometry, a wide rib base significantly increases the effective load-bearing capacity of the bonding zone compared to blunt rib base [14, 16, 17].

Previous research has demonstrated the lightweight potential of this hybrid design compared to classical metal structures, as well as the possibility of realising highly loadable structural components such as crash-relevant vehicle parts [5, 18, 19]. In contrast to FRP, injection moulding hybrids without metal inserts, the surface of the metal component needs to be modified to ensure a high bonding strength between metal and injection moulding compound or FRP [20]. In addition to macroscopic or microscopic interlockings [21, 22], adhesion promoters in the form of films or coatings are also used [22, 23], showing that these pretreatments can lead to highly loadable joints [24]. However, the pretreatment effort is often high, which means that these methods are not yet suitable for inline treatment of the metal surface within the cycle time of the injection moulding process. Plasma technology is an alternative to the methods mentioned. With this process, metal surfaces are cleaned and pretreated quickly and automatically. In addition, an adhesion promoter can be deposited by plasma polymerisation of precursors on the surfaces to improve the adhesion between metal and thermoplastic [25].

Thereafter, the coated metal inserts must be heated before overmoulding with injection moulding compound, pressed or printed with FRP in order to achieve high bonding strength [26].

The aim of this paper is to investigate the influence of the precursor application parameters and the metal preheating on the bonding strength between injection moulding compound and a plasma pretreated metal insert.

2 Materials and Methodology

2.1 Materials

The steel insert is made of a cold-rolled low alloyed steel (HC 420 LA). The used precursor (PT-Bond 1300.1, from Plasmamatreat GmbH, Seinhagen, Germany) acts as a chemical adhesion promoter. In order to increase the bonding strength, a precursor adapted injection moulding compound based on modified polyamide 6 (AKROMID® B3 GF 30 1 PST black (6647), from AKRO-PLASTIC GmbH, Niederzissen, Germany) is used.

2.2 Manufacturing Process

The manufacturing of the test specimens comprises the following main steps: chemical cleaning, plasma cleaning and coating, preheating and injection moulding.

Chemical Cleaning. As the cold-rolled steel HC 420 LA is prone to oxidation, an oil film is applied after the manufacturing for delivery and storage. In order to achieve bonding between the precursor and the metal, a two steps chemical cleaning process is performed. First, the coarse contaminations are removed by isopropanol and wiping with paper cloth until no residues remain. Afterwards, the metal is flushed with isopropanol and left for drying, to avoid contamination by the paper cloth.

Plasma Cleaning and Coating. To achieve an ultra-fine cleaning of the metal surface, the specimens undergo a robot-guided (KR6, from KUKA Industries GmbH, Augsburg, Germany) plasma cleaning and coating process (Fig. 1). The parameters of the plasma cleaning are shown in Table 1.

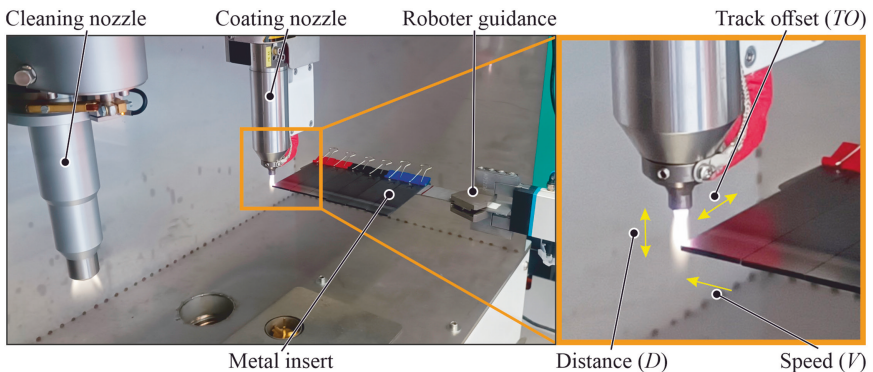
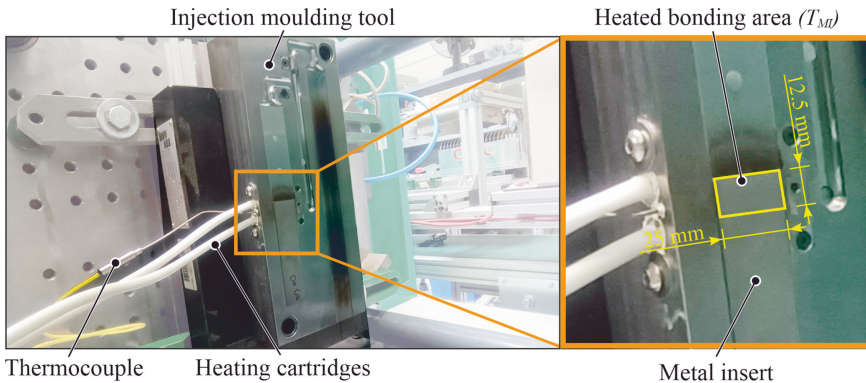


Fig. 1. Plasma cleaning and coating process.

Table 1. Parameter set for plasma cleaning and coating process.

Parameter	Cleaning	Coating
Voltage in V		290
Frequency in kHz		21
Plasma cycle time in %		60
Ionization gas flow in l/min	60	33
Carrier gas flow in l/h	N/A	300
Precursor mass flow in g/h	N/A	6
T piece temperature in °C	N/A	175
Jet head temperature in °C	N/A	110
Vaporizer temperature in °C	N/A	340

Preheating. For the preheating of the metal insert (Fig. 2) an injection moulding tool equipped with two additional 450 W heating cartridges (MISF19002B, from Hotset GmbH, Lüdenscheid, Germany) was used. To achieve the minimum Temperature of 80 °C, the metal insert was preheated for 30 s prior overmoulding by the tooling temperature. The temperatures of 160 °C and 240 °C were realized with 90 s and 240 s preheating time by the additional heating cartridges, which enable a local heating of the bonding area (Fig. 2 right).

**Fig. 2.** Injection moulding tool with integrated heating cartridges.

Injection Moulding. For overmoulding an Arburg 370H (Allrounder 370H 600-290, from Arburg GmbH+Co KG, Lossburg, Germany) injection moulding machine was used. The process parameters are summarized in the Table 2. To prevent oxidation and moisture absorption by the polyamide 6 all hybrid test specimens were kept in dry bags until testing.

Table 2. Injection moulding process parameters.

Injection speed	Packing pressure	Holding pressure	Cooling time	Injection mass temperature
150 cm ³ /s	1200 bar	550 bar	30 s	280 °C

2.3 Design of Experiments

To investigate the relationship between the process parameters and the structural properties, a two-level full factorial design (FFD) with a central point was chosen. After the analysis of the manufacturing process [27], 81 process parameters were identified that could have an impact on the bonding strength. For the experimental design (Table 3), these parameters were further reduced to four factors by taking the manufacturing and economical restrictions into account. The speed (V) and track offset (TO) of the plasma nozzle are selected (Fig. 1 right), as these factors are important to reduce the pretreatment time and therefore to increase the efficiency. The distance (D) of the plasma nozzle to the metal surface is relevant (Fig. 1 right), as highly complex metal parts restrict the required clearance of the plasma pretreatment process. To account for different preheating technologies and therefore the maximum achievable temperatures within reasonable time, the temperature of the metal insert (T_{MI}) was selected (Fig. 2 right).

Table 3. Variation of the factors for the 2⁴ – FFD.

Factor	Level–	Level 0	Level+
Speed in m/min	4	12	20
Track offset in mm	1	5	9
Distance in mm	4	12	20
Metal insert temperature in °C	80	160	240

2.4 Mechanical Testing

To determine the shear properties with sufficient statistical certainty six test specimens of each configuration are tested under standard climate of 23 °C and 50% relative humidity. To prevent mix mode loads during the tensile testing [28], a specific compression shear testing device [28] is used. By redirecting the tension forces introduced by the testing machine (Zwick Z100, from ZwickRoell AG, Ulm, Germany), to the compression edge of the compression shear testing device, primarily shear stresses occurs within in interface of the joint.

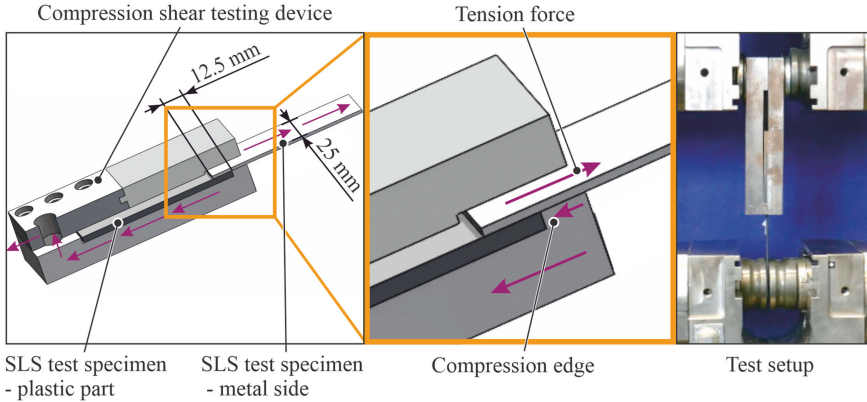


Fig. 3. Compression shear testing device (left and centre) [29] and test setup (right).

The force occurring during the test was recorded using a calibrated 10 kN load cell (Z12, from Hottinger Brüel & Kjaer GmbH, Darmstadt, Germany) and compared with the corrected crosshead travel measurement data. The measurements are recorded up to a force drop of 80% at a testing velocity of 2 mm/min in according to DIN EN 1465:2009.

3 Results and Discussion

3.1 Test Results

The results obtained can be divided into two categories: adhesive (left side) and cohesive (right side) failure, as shown in Fig. 4. No combination of the factors: distance, speed and track offset leads to adhesion at the preheating temperature of $T_{MI} = 80\text{ }^{\circ}\text{C}$ (test series 1 to 8) of the metal insert. At the centre-point, $T_{MI} = 160\text{ }^{\circ}\text{C}$ first bonding between the precursor and the injection moulding compound appears with a mean value of 6 MPa. For all factor combinations performed at $T_{MI} = 240\text{ }^{\circ}\text{C}$, adhesion with cohesive failure occurs. Both the mean values and the scattering depend on the combination of the values of V , TO and D . The lowest bonding strengths of 2.75 MPa mean value emerge at low V and D in combination with a narrow TO . The highest values between 30.3 MPa and 41.6 MPa bonding strength are achieved with the V of 4 m/min, D of 20 mm and TO settings of 1 mm.

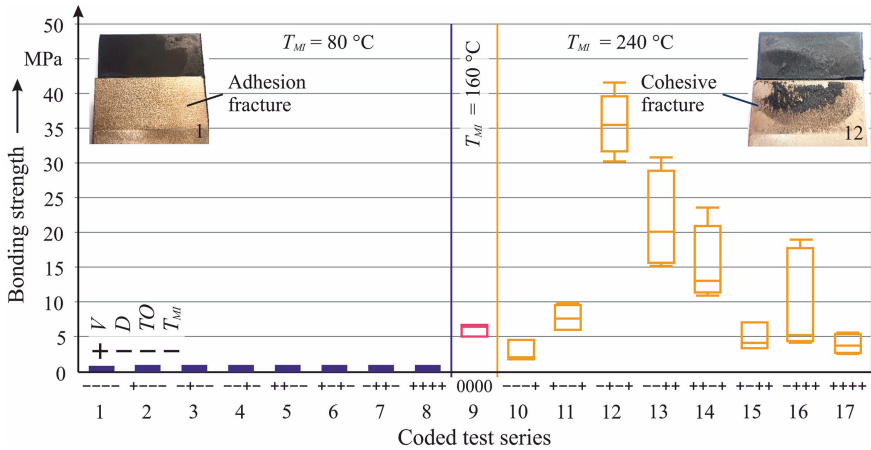


Fig. 4. Test results for the 2^4 – full factorial design.

For the test series 1 to 8 (Fig. 4), performed at low preheating temperature of the metal insert, only adhesion failure occurs (Fig. 4, top left corner). Small amounts of plastic residuals appeared on metal surface after testing for the series 9 to 11 as well as 15 and 17. The fracture surface of the test series 13, 14 and 16 indicates a mixture of adhesive failure between the metal and injection moulding compound as well as cohesive failure of the thermoplastic itself. A factor combination performed in the test series 12 causes fracture behaviour dominated by cohesive failure of the reinforced thermoplastic (Fig. 4, top right corner).

3.2 Statistical Modelling of Parameter Interactions

The first step to achieve a prediction model [30] of the bonding behaviour was to identify the factors and interactions which influence the mean bonding strength.

For this purpose, a significance level (α) of 1% was chosen. All factors and interactions lower than α are regarded to be statistically significant. The results of the reduced model are shown in Table 4. The software JMP 16 (SAS Institute GmbH, Heidelberg, Germany) was used for the analysis, modelling and visualisation of the 2^4 – FFD.

Table 4. Table for main effects, interaction effects and p-values.

	Factors and Interactions	p-value
1	T_{MI}	0.00000
2	$V * D * TO$	0.00006
3	$D * TO * T_{MI}$	0.00173
4	$D * TO$	0.00173
5	V	0.02152
6	$V * T_{MI}$	0.02152
7	$V * D$	0.08596
8	D	0.10136
9	$D * T_{MI}$	0.10136
10	$TO * T_{MI}$	0.16194
11	TO	0.16194
12	$V * TO$	0.48153

With the data in Fig. 4, a prediction model for the mean value of the maximum bonding strength (R_{max}) is described through the four factors: V , D , TO , T_{MI} and their interactions by Eq. 1.

$$\begin{aligned}
 R_{max} = & -17.437 + 1.500 * V + 0.389 * D + 1.360 * TO \\
 & + 0.036 * T_{MI} - 0.093 * V * D \\
 & - 0.189 * V * TO - 0.004 * V * T_{MI} \\
 & - 0.067 * D * TO + 0.009 * D * T_{MI} \\
 & + 0.011 * TO * T_{MI} + 0.014 * V * D * TO \\
 & - 0.001 * D * TO * T_{MI}
 \end{aligned} \tag{1}$$

It is important to note that the factors and interactions participating in the model cannot be reduced further. Those factors or interactions which do not meet the α criteria (5 to 12; Table 4) are part of the significant ones (1 to 4; Table 4).

Having identified the significant process parameters and the interactions among them, the next step is to determine the optimal parameter setting which will maximize the bonding strength by optimizing Eq. 1 (Table 5).

Table 5. Optimal process parameter settings for maximizing the bonding strength (R_{max}).

Factor	Level for maximum bonding strength (R_{max})
Speed in m/min	4
Distance in mm	20
Track offset in mm	1
Metal insert temperature in °C	240

The visualisation of the model by three-dimensional graphs (Figs. 5 and 6) allows the representation of the relationships of V , D and TO to the target variable: bonding strength. Using these graphs, the designer of hybrid components can easily select an appropriate parameter combination to meet a specific economical and manufacturing constraint on the interface bonding strength.

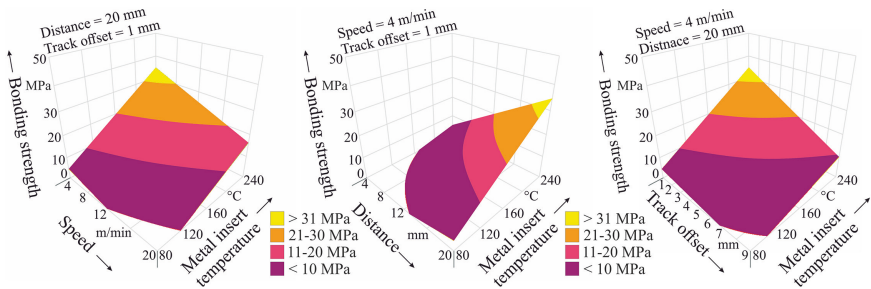


Fig. 5. Graphs representing the correlation between speed (left), distance (centre) and track offset (right) on the bonding strength in relation to the metal insert temperature.

If, for example, a high bonding strength is to be achieved by using infrared heating elements that limit the maximum preheating temperature to 160 °C, Fig. 5 can be scanned for favourable settings of speed, distance and track offset. In this case the factor set of $D=20$ mm, $TO=1$ mm and $V=4$ m/min leads to a mean bonding strength of 20 MPa. As the studies on induction assisted preheating [26] have shown, it is possible to achieve economic and consistent heating of complex shaped metal structures. Therefore the graphs in Fig. 6 are used to obtain convenient process parameters for fixed metal insert temperature.

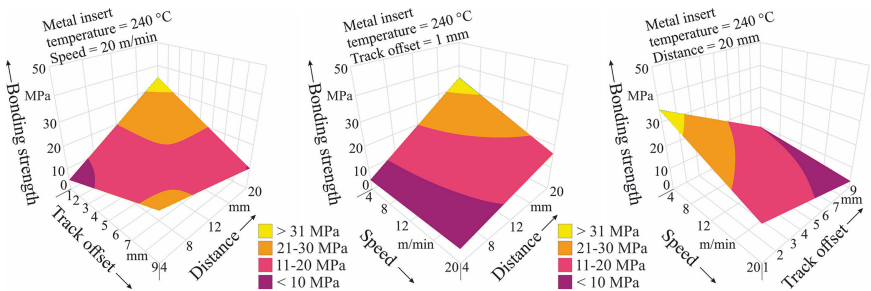


Fig. 6. Graphs representing the correlation between track offset (left), speed (centre) in relation to the distance and speed (right) in relation to the track offset on the bonding strength.

4 Conclusion

The precursor-based adhesion promoter applied by means of plasma technology enables a strong bond between metal and injection moulding compound. The application of the adhesion promoter is controlled by different process parameters leading to different bonding strengths. The metal insert temperature and the interactions of $V \cdot D \cdot TO$, $D \cdot TO \cdot T_{MI}$ and $D \cdot TO$ have an increasing effect on the interface strength (Table 4). The determined bonding strength prediction model provides reliable results above 40 MPa.

Based on the model, the process and geometrical restrictions, the designer can estimate the bonding strength between the metal and injection moulding compound.

For the investigations of the process-structure-property relationship and the design of the model, only 4 of 81 possible process influencing factors are investigated in detail by full factorial design of experiments. There is still a need for further research, especially to investigate the influences of physical plasma generation and precursor chemistry on bonding strength to different metals and injection moulding compounds.

Acknowledgement. This research and development project: HYPRO – Holistic implementation of hybrid design in series production (03XP0284A-J) is sponsored by the Federal Ministry of Education and Research (BMBF) within the framework “Werkstoffplattform Hybride Materialien (HyMat)” and supervised by the Project Management Agency Jülich (PTJ). The authors are responsible for the content of this publication. The participating project partners would like to thank the above-mentioned institutions for providing the financial resources.

Conflict of Interest

The authors declare that they have no conflict of interest.

References

1. European commission: A European Green Deal. https://commission.europa.eu/strategy-and-policy/priorities-2019-2024/european-green-deal_en. Accessed 26 Jan 2023
2. Federal Ministry for Economic Affairs and Climate Action (BMWi): Die Nationale Wasserstoffstrategie, Berlin (2020)
3. Federal Ministry for Economic Affairs and Climate Action (BMWi): Industriestrategie 2030 – Leitlinien für eine deutsche und europäische Industriepolitik, Berlin (2019)
4. Kupfer, R., Schilling, L., Spitzer, S., Zichner, M., Gude, M.: Neutral lightweight engineering: a holistic approach towards sustainability driven engineering. *Discover Sustain* 3, 17 (2022)
5. Kellner, P.: Zur systematischen Bewertung integrativer Leichtbau-Strukturkonzepte für biegebelastete Crashtträger. Dissertation, Technisch Universität Dresden (2013)
6. Hufenbach, W., Krahl, M., Kupfer, R., Rothenberg, S., Weber, T., Lucas, P.: Enhancing sustainability through the targeted use of synergy effects between material configuration, process development and lightweight design at the example of a composite seat shell, In: Hung, S., Subic, A., Wellnitz, J. (eds.) *Sustainable Automotive Technologies 2011*, In: Proceedings of the 3rd International Conference (ICSAT), Springer, pp. 103–110, Berlin (2011)
7. Müller, T.: Methodik zur Entwicklung von Hybridstrukturen auf Basis faserverstärkter Thermoplaste, Dissertation, Friedrich-Alexander-Universität Erlangen-Nürnberg (2011)

8. Müller, T., Drummer, D.: Process combinations as a key for producing lightweight and high-duty composite structures based on thermoplastic materials. In: Proceedings of the 15th European Conference on Composite Materials: ECCM-15, Venedig (2012)
9. Kaufmann, R., Bider, T., Bürkle, E.: Process integration: Lightweight parts with a thermoplastic matrix. *Kunststoffe international* 03, 106–109 (2011)
10. Dröder, K.: Prozesstechnologie zur Herstellung von FVK-Metall-Hybriden – Ergebnisse aus dem BMBF-Verbundprojekt ProVor^{Plus}. Springer, Braunschweig (2020)
11. Liebsch, A., Koshukow, W., Gebauer, J., Kupfer, R., Gude, M.: Overmoulding of consolidated fibre-reinforced thermoplastics - increasing the bonding strength by physical surface pre-treatments. *Procedia CIRP* 85, 212–217 (2019)
12. Joppich, T., Menrath, A., Henning, F.: Advanced molds and methods for the fundamental analysis of process induced interface bonding properties of hybrid, thermoplastic composites. *Procedia CIRP* 66, 137–142 (2017)
13. Valverde, M. A., Kupfer, R., Kawashiat, L. F., Gude, M., Hallett, S. R.: Effect of processing parameters on quality and strength in thermoplastic composite injection overmoulded components. *ECCM 18*, Athen (2018)
14. Hummel, S., Knorr, L., Karlinger, P., Schemme, M.: Eine Frage der Haftung – Die Verbundfestigkeit zwischen Organoblech und angespritzten Strukturen hängt von vielen Einflussfaktoren ab. *Kunststoffe* 07, 41–45 (2017)
15. Moritzer, E., Budde, C., Hüttner, M.: Wie Kurz- und Endlosfasern sich am besten vertragen. *Kunststoffe* 3, 85–88 (2015)
16. Stegelmann, M., Krahl, M., Garthaus, C., Hufenbach, W.: Integration of textile reinforcements in the injection-moulding process for manufacturing and joining thermoplastic support-frames. In: Proceedings of the 20th International Conference on Composite Materials: ICCM-20. Copenhagen (2015)
17. Luft, J., Liebsch, A., Kupfer, R., Zentgraf, T., Jäger, H.: Untersuchungen zur Festigkeit der Verbindungszone in thermoplastischen Hybridstrukturen. In: 26. Fachtagung über Verarbeitung und Anwendung von Polymeren, Chemnitz (2019)
18. Kellner, P., Steinbach, K.: Die 3D-Hybrid Leichtbautechnologie: Eine neuartige Stahl-GFK-Hybridbauweise für höchstbelastete Karosseriestrukturen. In: 18. Dresdner Leichtbausymposium, Dresden (2014)
19. Muhr, T., Weber, J., Theobald, A., Hillebrecht, M.: Wirtschaftliche Leichtbauweise für eine hybride B-Säule. *ATZ - Automobiltechnische Zeitschrift* 3, 16–20 (2015)
20. Grujicic, M., Sellappan, V., Omar, M., Obieglo, N., Seyn, S., Erdmann, M., Holzleitner, J.: An overview of the polymer-to-metal and direct-adhesion hybrid technologies for load-bearing automotive components. *J Mater Process Technol* 197, 363–373 (2008)
21. Ehrenstein, G., Amesöder, S., Fernandez Diaz, L., Niemann, H., Deventer, R.: Werkstoff- und prozessoptimierte Herstellung flächiger Kunststoff-Kunststoff und Kunststoff-Metall-Verbundbauteile. In: Tagungsband zum Berichts- und Industriekolloquium 2003 des SFB 396, Meisenbach Bamberg (2003)
22. Kohl, M.L., Schrickler, K., Bergmann, J.P., Lohse, M., Hertel, M., Füssel, U.: Thermal joining of thermoplastics to metals: Surface preparation of steel based on laser radiation and tungsten inert gas arc process. *Procedia CIRP* 74:500–505 (2018)
23. Haider, D.R., Krahl, M., Koshukow, W., Wolf, W., Liebsch, A., Kupfer, R., Gude, M.: Adhesion studies of thermoplastic fibre-plastic hybrid components Part 2: thermoplastic-metal-composites. *Hybrid Materials and Structures*, Bremen (2018)
24. Melamies, I.A.: Haftung als Messlatte. *J Oberflächentechnik* 56, 42–45 (2016)
25. Schettler, F., Ulke-Winte, L., Sorge, K., Nendel, W., Kroll, L.: Integrative Beschichtungstechnologien im Fahrzeugbau. *Kunststoffe* 03, 75–79 (2015)

26. Stier, T., Rieck, M., Lammert, N.: 3D Printing with Pellet Extruded Plastics on Metal. *Kunstst. Int.* 10, 14–17, (2020)
27. Koshukow, W., Liebsch, A., Kupfer, R., Troschitz, J., Schneider, F., Gude, M.: Entwicklung und Aufbau einer automatisierten Prozesskette für die Herstellung komplexer Kunststoff-Metall-Hybridstrukturen. In: *Technomer 2021–27. Fachtagung über Verarbeitung und Anwendung von Polymeren*, Chemnitz (2021)
28. Schneider, K., Lauke, B., Beckert, W.: Compression Shear Test (CST) – A convenient apparatus for the estimation of apparent shear strength of composite materials. *Appl. Compos. Mater.* 8, 43–62. (2001)
29. Wippermann, J., Meschut, G., Koshukow, W., Liebsch, A., Gude, M., Minch, S., Kolbe, B.: Thermal influence of resistance spot welding on a nearby overmolded thermoplastic-metal joint. *Welding in the World* (2023)
30. Jiju, A.: *Design of experiments for engineers and scientists*. Elsevier (2014)



Differential Evolution Based Optimisation of Multi-layered Space Radiation Shielding for Satellite Electronics

Nico Gerster and Tobias Dickhut (✉)

Chair of Composites and Technical Mechanics, Universität der Bundeswehr München,
85577 Neubiberg, Germany

{nico.gerster,tobias.dickhut}@unibw.de
<https://www.unibw.de/mb/institute/we8/we84>

Abstract. The recent push for the privatisation and commercialisation of space imposes considerable incentives to reduce costs and technological thresholds. Advances in satellite technologies are required to meet these new challenges. Fibre-reinforced composite materials have found considerable application in satellite structures due to their lightweight nature. These composites however often require additional structures and components to meet further functional requirements. Radiation shielding is a critical design aspect for satellites and substantial efforts are often made to best place components and provide sufficient shielding. The laminated nature of composite materials lends itself well to the integration of functional layers to exploit secondary radiation effects and thereby improve the overall shielding performance of these materials. However, the optimisation of multi-layered shielding has only been developed at a rudimentary level. In this paper, an optimisation approach for multi-layer shielding materials based on target weights is proposed. The optimisation approach samples the entire solution space for an n-layered material in conjunction with a differential evolution algorithm to find an optimal configuration. This approach offers considerable improvements in theoretical shielding performance over previous results. Furthermore, due to the efficient optimisation approach the functional layers can be adapted to best shield against the radiation field of a specific orbit.

Keywords: Ionizing Radiation · Radiation Shielding · Multi-Layer Material · Satellite Electronics

1 Introduction

Radiation shielding in satellites aims to reduce the damage effects of penetrating radiation to acceptable levels. The inclusion of shielding materials is diametrically opposed to minimizing the mass of the satellite structure. The shielding of satellite electronics is currently being achieved with homogeneous aluminium [1], as it offers a compromise between proton and electron shielding capabilities.

Shielding made of aluminium is commonly used in conjunction with radiation-resistant integrated circuits with different architectures and materials. Physical shielding reduces the energy of ionising radiation and thereby the total dose that can be transferred into sensitive electronic devices and the unique architecture of space-qualified components reduces the sensitivity toward radiation.

The three types of damage occurring due to space radiation in the electronic components of satellites is the cumulative dose or total ionising dose (TID), displacement damage (DD) and single event effects (SEEs), such as single event upsets (SEUs) and single event latchups (SELs). While the total dose is a time-dependent variable, DD and SEEs depend on the linear energy transfer (LET) of individual particles of ionising radiation, notably protons and other heavy ions.

Multi-layer shielding solutions have been investigated in recent years. Most of these studies address the feasibility of designing a suitable multi-layer material. Multi-layer shielding aims to enhance the shielding effectiveness to such an extent that off-the-shelf hardware can be used, particularly in low earth orbit missions, without compromising the reliability of the mission. In this work, an optimisation approach based on differential evolution for multi-layer materials is proposed.

To implement these multi-layer shielding materials to their fullest potential, numerous aspects have to be optimised, including where functional layers are located in a laminate, the individual layer thicknesses and the material composition of individual layers. Previous approaches heavily restricted the degrees of freedom [2], resulting in suboptimal solutions, or did not constrain the problem enough to satisfy real-world applications [3, 4].

The approach adopted in this work allows multi-layered shielding materials to be optimised for a mission target orbit with a specific target weight. This presents a flexible and efficient approach to radiation shielding, particularly multi-layer shielding approaches as a pioneering satellite technology. When combined with flexible manufacturing technologies, under the premise that satellites are often manufactured as one-offs or in small quantities and prepared for each mission individually, this presents a viable solution, particularly for scientific and small-scale commercial missions.

2 Particle Flux Predictions

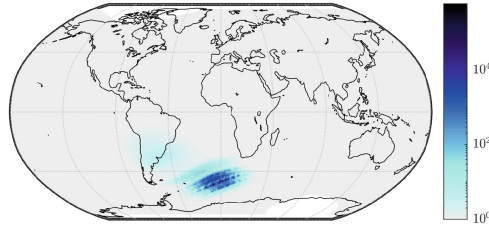
The first step in developing efficient radiation shielding, appropriate for a mission, is to understand the composition of the anticipated space radiation environment. The incident particles are in part defined by the use of trapped particle models *AP8* and *AE8* [5,6], as well as the revised *AP9* and *AE9* models [7], for protons and electrons respectively. These tools require the orbit of the satellite to be defined. Based on the orbit, particularly inclination, apogee and eccentricity, as well as the total mission duration, the particle flux for trapped protons and electrons can be predicted.

This research is part of the *SeRANIS* mission of the Bundeswehr University Munich, intending to demonstrate key satellite technologies in orbit. For this, the *ATHENE* satellite will integrate numerous hardware and software-based experiments, including a payload to demonstrate a multi-layer shielding material. The satellite is planned to enter a low sun-synchronous orbit in 2025. Due to the high inclination of the target orbit dose measurements can be performed over a vast range of latitudes. Orbit parameters are provided in Table 1.[8]

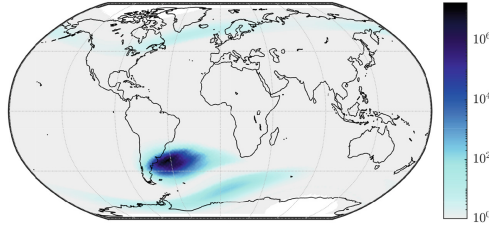
Table 1. *ATHENE* orbit parameters

Variable	Value	Unit
Apogee	512.8	km
Perigee	495.5	km
Inclination	97.4	deg

The majority of radiation exposure is expected when flying over the South-Atlantic anomaly for both electrons and protons. Furthermore, for electrons, a noticeable flux is expected in the polar regions, shown in Fig. 1. The flux maps show all particles above the minimum energy levels that can be predicted by the models. Namely $0.1MeV$ and $0.04MeV$ for protons and electrons respectively.



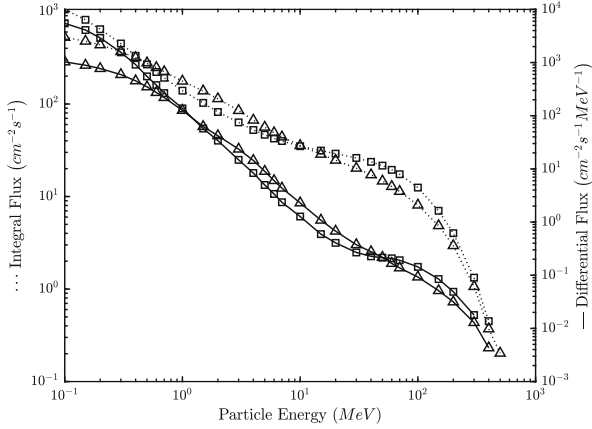
(a) Proton flux map above 0.1MeV



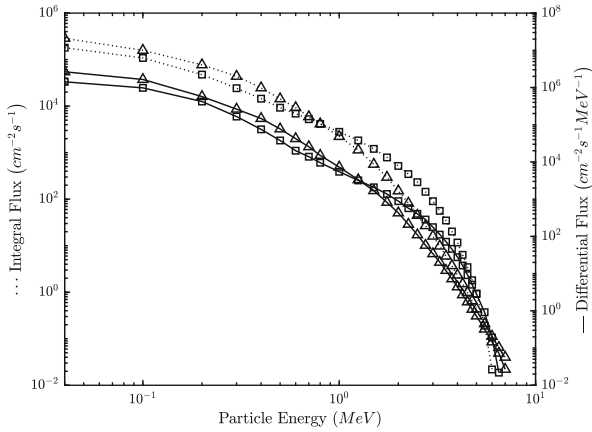
(b) Electron flux map above 0.04MeV . Additional flux is expected in the polar regions.

Fig. 1. World map showing the integral trapped particle flux for the *ATHENE* orbit, based on the legacy models. Flux peaks are expected over the South-Atlantic Anomaly. Regions left in white indicate where the legacy models cannot be applied.

The proton and electron fluxes for the orbit are shown in Fig. 2. Here, lower energy particles have a higher flux. Furthermore, electrons tend to occupy substantially lower energy ranges, while protons range from a few MeV to several hundred MeV .



(a) Flux predictions for trapped protons over an energy range from 0.1MeV to 1GeV



(b) Flux predictions for trapped electrons over an energy range from 0.04MeV to 10MeV

Fig. 2. Mean integral and differential particle flux predictions indicated by dotted and solid lines respectively based on the legacy and revised trapped particle flux prediction models, shown by the square and triangular markers respectively. The models agree for mean flux predictions and demonstrate an inverse proportionality between particle counts and particle energies.

3 Radiation Shielding Optimisation

Trapped particles in low earth orbit consist of electrons and protons. The particle physics, types of interactions and braking phenomena are different for each particle species. Materials best suited for the attenuation of electrons are dense metals with a high ratio of the square of the atomic number to the atomic mass

(Z^2/A) , while protons are best attenuated by materials with a high atomic number to atomic mass ratio (Z/A) , such as hydrogen and substances containing hydrogen. This gives rise to multi-layer approaches typically employing a 'low-high-low' atomic number structure, as outlined in [2,9].

In this work, the monte-carlo based *Geant 4* tool *Multi-Layered Shielding Simulation Software (MULASSIS)* [10] is used to simulate the dose associated with planar multi-layer radiation shields. Here the individual layers are defined by their density and atomic composition.

For all simulations a detector layer is added after the multi-layer shielding material, to measure the dose penetrating the shield. The total dose is therefore a function of the individual layer thicknesses, densities and atomic composition and to a lesser extent the definition of the detector layer itself.

Due to the probabilistic nature of the monte-carlo simulation, the results for the ionising dose are noisy. Hence classical optimisation algorithms, requiring the objective function to be continuous and differentiable, cannot be used. Furthermore, the monte-carlo simulations provide error estimates on the dose values, highlighting the inability to use results from the objective function directly, but rather the need to observe trends and adjust the layout of the multi-layer shielding material accordingly.

Therefore, a probabilistic meta-heuristic like differential evolution (DE) must be used, as it does not make any assumptions about the properties of the objective function. Given enough iterations and appropriate tuning of the algorithm parameters the algorithm converges to the global optimum.

A python-based extension to *MULASSIS* was written to combine and automate the *MULASSIS* based particle simulations with the differential evolution based optimisation. The code takes material properties from a user-defined list of materials to write the macro for the simulation and executes the *MULASSIS* code. Based on simulation results the multi-layer material is optimised to minimize the penetrating dose for a given mass target T .

The use of an areal weight constraint allows the results of the simulation to be compared against dose depth curves for aluminium and to identify the effectiveness of the solution. This constraint on the thicknesses x_i is expressed in Eq. 1 with the layer densities ρ_i :

$$T = \sum_{i=1}^n x_i \rho_i \quad (1)$$

To start the optimisation, the target weight T must be defined by the user. Similarly, the number of layers n is required to restrict the optimisation. Furthermore, the available materials for the optimisation must be stored in a file, alongside their respective densities, and atomic compositions.

In this work, the arrangement of the materials, i.e. which material is used for which layer, is fixed by the user. This is particularly sensible for simple tri-layer laminates, which are receiving a significant amount of research. The arrangement of the layers however can be made variable subject to the optimisation algorithm, but will considerably increase the duration of the optimisation code.

The differential evolution algorithm employed in this work requires an initial population of trial solutions. This population is automatically generated by the code to ensure the entire solution space is sampled.

The target weight T must be equal to the dot product of the layer thickness vector \mathbf{x} and associated densities vector $\boldsymbol{\rho}$. As a mass budget is provided during the design of a satellite, based on previous designs and radiation prediction analysis tools, this is used to fix the constraint and subsequently the layer thicknesses in \mathbf{x} . Therefore, the following equation can be used as a constraint on the global optimisation.

$$T = \mathbf{x} \cdot \boldsymbol{\rho} = \sum_{i=1}^n x_i \rho_i \quad (2)$$

The dimensions of the constraint equation can be removed by normalising with the target weight T . This results in a dimensionless form of the constraint equation with non-dimensional thicknesses ξ_i as follows.

$$\xi_i = \frac{x_i \rho_i}{T} \Leftrightarrow x_i = \frac{T \xi_i}{\rho_i} \quad (3)$$

The target weight constraint is redefined, where the sum of the non-dimensional thicknesses is equal to 1. Consequently, to test multiple solutions, the non-dimensional components can be varied.

$$1 = \sum_{i=1}^n \xi_i \quad (4)$$

To systematically create trial solutions the non-dimensional thicknesses can be produced with integers λ_i . For the initial population a set of possible integers are assigned for each individual thickness. This results in a set of combinations of these integer values that cover the entire solution space. The null solution can be removed as it sets all layer thicknesses to zero, thereby violating the target condition. It is then required to scale the values for each possible combination of λ values to determine the non-dimensional layer thickness vector $\boldsymbol{\xi}$. The scaling coefficient ϕ is defined via the non-dimensional constraint derived above:

$$1 = \sum_{i=1}^n \xi_i = \phi \sum_{i=1}^n \lambda_i \quad (5)$$

This gives the scaling coefficient:

$$\phi = \left(\sum_{i=1}^n \lambda_i \right)^{-1} \quad (6)$$

The non-dimensional thicknesses can be recovered with:

$$\boldsymbol{\xi} = \phi \boldsymbol{\lambda} \quad (7)$$

4 Demonstration Tri-Layer Laminate

In this paper we focus on a tri-layer laminate to demonstrate the capabilities of the optimisation algorithm. The optimisation approach developed is compared against classical shielding solutions, as well as to the approach taken by Beaucour [2], which similarly constrained the target weight.

In the optimisation attempt by Beaucour, a tri-layer laminate was explored and optimised by symmetrically distributing material around an inner layer. The optimisation was performed by simply varying the thickness of the internal layer, while maintaining the total areal weight of the shielding material.

This symmetric distribution of the ‘low’ molecular weight material, although offering some optimisation potential, still leaves considerable room for improvement. This can be demonstrated by comparing the possible solution spaces for an approach following Beaucour and the one presented in this work. Shown graphically below is the solution space for a tri-layer laminate, with the outer layers made of polyethylene (PE) and the central layer being made of tungsten (W). The full solution space, represented by the shaded grey area allows all radiation effects to be exploited fully, while the solution space according to Beaucour, shown by the red dashed line, over-restricts the degrees of freedom and consequently the effectiveness of the shielding solution.

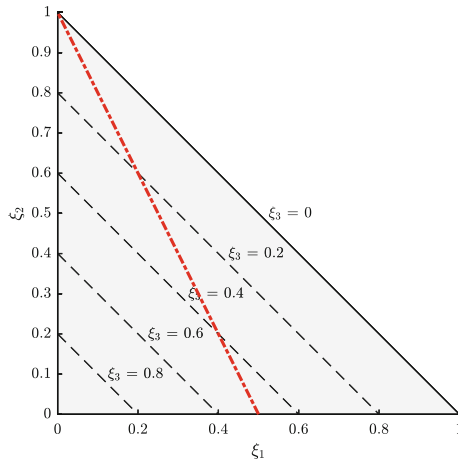


Fig. 3. Solution space for optimisation process in the dimensionless coordinate variables for a tri-layer laminate. The shaded triangle shows unrestricted solution space, while the red dashed line represents the symmetrically constrained solution space.

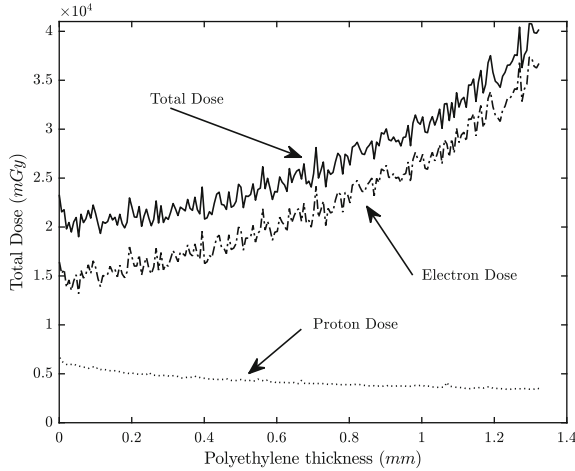


Fig. 4. Plot showing total dose predictions for varying outer polyethylene thicknesses. The total dose is represented by the solid line. Proton and electron dose results are shown by the dash-dotted and dotted lines respectively.

The optimisation potential of the method proposed by Beaucour is shown graphically in Fig. 4 for a target weight of 0.25g/cm^2 . Adjusting the individual layer thicknesses results in significant improvements in the shielding performance for the same material configuration, as can be seen by reducing the PE thickness. Consequently, the tri-layer laminates must be optimised to obtain an effective shielding material. With this restrictive approach to optimisation, improvements in comparison to homogeneous aluminium can be realised. However, as the *ATHENE* orbit is dominated by electrons, the constraints imposed on the optimisation emphasize the shielding of electrons, to the disadvantage of protons and more importantly secondary radiation in the form of x-rays. This results in a tungsten-heavy shielding material, unable to fully exploit secondary radiation effects.

In contrast, employing the method outlined in this work allows for substantial improvements to be made in a tri-layer configuration. This is as the full optimisation allows all secondary effects to be exploited to the fullest extent. The use of a differential evolution algorithm along with the initial population crudely covering the entire solution space for an n-layer shielding laminate, allows the optimisation to iteratively improve without falling into local minima. The optimisation potential of the tri-layer laminate is demonstrated in Fig. 5.

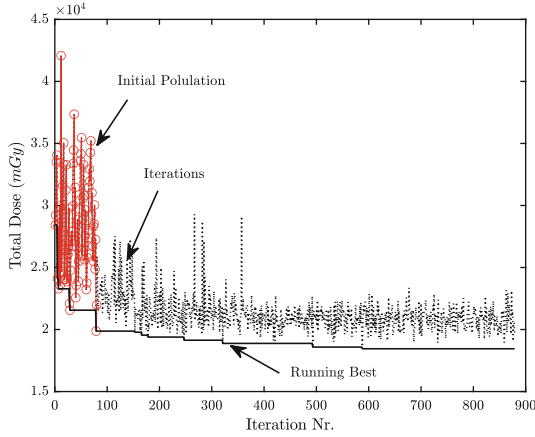


Fig. 5. Plot showing the full optimisation of a tri-layer laminate, with the outer layers made of polyethylene and the inner layer made of tungsten. The total dose received by the detector is plotted against the iteration number. The initial population of the optimisation algorithm is shown by the red circles, while subsequent optimisation attempts are shown by the black dashed line. The best solution found is recorded with the solid black line.

The optima for the methods are summarised in Table 2 below. The optimisation algorithm offers substantial improvements over homogeneous aluminium shielding, allowing the total dose to be reduced by 52%. This furthermore demonstrates that for the same target weight noticeable improvements can be achieved with an overall dose reduction of 8.1%, simply by opening up the solution space.

Comparing the dose components for protons and electrons demonstrates that the tri-layer laminate sacrifices some shielding capabilities against protons, but significantly improves the shielding of electrons. The optimisation based on *DE* demonstrates better performance for each dose component individually, furthermore demonstrating that opening up the solution space removes unnecessary performance losses.

Table 2. Table showing optimisation results for new and classical optimisation approaches with material distributions and total dose for protons and electrons, as well as the total dose received through an equivalent piece of aluminium.

	thicknesses (mm)			Dose (mGy)		
	x_1	x_2	x_3	p^+	e^-	Total
Aluminium	- 0.926 -			4,171	34,446	38,617
Beaucour	0.0267	0.127	0.0267	5,956	14,129	20,085
Gerster	0.0482	0.126	0.0291	5,917	12,533	18,451

5 Conclusion

It is evident that multi-layer radiation shielding offers a great potential for improvements in the shielding of satellite components, thereby allowing for greater mission safety or the use of cheaper and more capable off-the-shelf components in the future.

The optimisation of radiation shielding material, particularly made of multiple layers, can be substantially improved with the use of differential evolution algorithms and an initial population that informs the algorithm of solutions across the entire solution space. With this less restrictive optimisation secondary radiation effects can be exploited more fully, resulting in more efficient shielding materials.

As the particle flux of trapped ionising radiation varies significantly between orbital heights, eccentricity and inclination no standardised radiation shielding material configuration can be realised. This drives the need for mission-specific shielding solutions. The optimisation defined in this work, and a mission-dependent shielding mass budget, allows a unique radiation shielding configuration to be developed for individual missions and target orbits.

The need for a flexible radiation shielding architecture lends itself to be integrated as functional layers in fibre-reinforced composite structures, as these already rely on a layer-wise construction and offer improved specific mechanical properties in comparison to metallic materials.

Acknowledgements. This work was supported by the dtcc.bw-Digitalization and Technology Research Center of the Bundeswehr through the Project SeRANIS-Seamless Radio Access Networks in the Internet of Space under Grant 150009910.


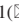





References

1. “Methods for the calculation of radiation received and its effects, and a policy for design margins,” standard, European Cooperation for Space Standardisation, Noordwijk, NL. (2008)
2. Mangeret, R., Carriere, T., Beaucour, J., Jordan, T.: Effects of material and/or structure on shielding of electronic devices. *IEEE Trans. Nucl. Sci.* **43**(6), 2665–2670 (1996)
3. Nartallo, R.: “JORE2M2 Project: GA Shield Optimiser for MULASSIS. Requirements, Interface Control, Design, Implementation and Justification Document,” tech. rep. (2010)
4. Daneshvar, H., Milan, K. G., Sadr, A., Sedighy, S. H., Malekie, S., Mosayebi, A.: “Multilayer radiation shield for satellite electronic components protection”. *Sci. Rep.* **11** (2021)
5. Sawyer, D.M., Vette J. I.: “AP-8 trapped proton environment for solar maximum and solar minimum. [AP8MAX and AP8MIN],” 12 (1976)
6. Vette, J. I.: “The AE-8 trapped electron model environment”. (1991)
7. Ginet, G., O’Brien, T., Huston, S., Johnston, W., Guild, T., Friedel, R., Lindstrom, C., Roth, C., Whelan, P., Quinn, R. et al.: “AE9, AP9 and SPM: New models for specifying the trapped energetic particle and space plasma environment’. *The Van Allen Probes Mission*, pp. 579–615, Springer (2013)

8. Kinzel, A., Bachmann, J., Jaiswal, R., Karnal, M., Novo, E.R., Porcelli, F., Schmidt, A., Förstner, R., Hofmann, C., Knopp, A., Schwarz, R. : “Seamless Radio Access Network for Internet of Space (SeRANIS): New Space Mission for Research, Development, and In-Orbit Demonstration of Cutting-Edge Technologies”. (2022)
9. Steffens, M., Hepp, F., Höoffgen, S.K., Krzikalla, P., Metzger, S., Pellowski, F., Santin, G., Tiedemann, L., Tighe, A., Weinand, U.: Characterization of Novel Lightweight Radiation Shielding Materials for Space Applications. *IEEE Trans. Nucl. Sci.* **64**(8), 2325–2332 (2017)
10. Lei, F., Truscott, R., Dyer, C., Quaghebeur, B., Heynderickx, D., Nieminen, R., Evans, H., Daly, E.: MULASSIS: A Geant4-Based Multilayered Shielding Simulation Tool. *IEEE Trans. Nucl. Sci.* **49**(6), 2788–2793 (2002)



Integrating Geometric Metamodel-Assisted Process Assurance into Topology Optimization of Low-Pressure Die Castings

Tobias Rosnitschek¹  , Maximilian Erber² ,
Christoph Hartmann² , Bettina Alber-Laukant¹ , Wolfram Volk² ,
and Stephan Tremmel¹ 

¹ Engineering Design and CAD, University of Bayreuth, 95643 Bayreuth, Germany
{tobias.rosnitschek,bettina.alber,stephan.tremmel}@uni-bayreuth.de

² Metal Forming and Casting, Technical University of Munich, 85748 Garching, Germany
{maximilian.erber,christoph.hartmann,wolfram.volk}@utg.de

Abstract. Integrating complex process knowledge into structural optimization of casting parts enables design proposals to exploit manufacturing processes' full potential. However, a significant bottleneck for integrating process knowledge is the computational effort necessary for process simulations. In this article, we focused on low-pressure die casting. We used the medial axis transform and the shortest path algorithm to describe geometry-related features that we used as input data for a neural network metamodel, which replaced the casting process simulation. This allowed us to reduce the time for process simulation from multiple hours to a few seconds and, thus, incorporate the metamodel into the topology optimization framework. To reconstruct the geometry, we used an implicit modeling approach in which the modified geometry was built from volume lattices filtered afterward to obtain solid volumes. The approach was tested on two application examples and proved that the metamodel-based results are equivalent to the results obtained using casting process simulations.

Keywords: Topology Optimization · Process Assurance · Medial Axis Transform · Neural Networks · Implicit Modelling

1 Introduction

Two key pillars for developing new products are climate neutrality and energy efficiency. Casting processes have the capability to combine both pillars advantageously by fabricating complex structures at high volumes [1, 2]. Accordingly, we can derive

Tobias Rosnitschek and Maximilian Erber contributed equally

two main objectives, on the one hand lightweight structures that minimize material usage, respectively energy consumption during the product life cycle. On the other hand, efficient and error-free manufacturable geometries, which minimize the scrap-rate. However, the search for a “perfect part” that combines both objectives is difficult. A major bottleneck is the integration of time-consuming process assurance simulation into a topology optimization framework. In this article, we integrate the process assurance via a geometric feature-based artificial neural network metamodel and modify the geometries using implicit modelling.

1.1 Background

Topology optimization is a widely used method for numerical structural optimization with the purpose of identifying the best material distribution in a given design space [3–6]. Nevertheless, optimized design proposals are often non-manufacturable. Therefore, manufacturing constraints are commonly used, for casting processes, these are, among others, minimum length scale, symmetry, extrusion, or parting lines [7–9].

These manufacturing constraints represent a simplification of the unconstrained optimization problem and cannot describe the limits of stable casting processes [10]. Since the major bottleneck for the efficient integration of process assurance is the time-consuming process assurance simulation, the use of computationally cheap metamodels can leverage the quality of casting design proposals significantly.

Such metamodels are often built upon machine learning models, inspired by the idea that in particular artificial neural networks represent universal approximators [11]. Accordingly, machine learning is widely used in manufacturing related topics as energy consumption, wear modelling or tool wear prediction [12–14]. In the context of casting processes, metamodels were applied to predict the results of 2D-casting simulations [15], properties such as hardness based on process parameters [16], or for increasing the product quality by optimizing initial temperature and wall temperature [17].

All the named examples apply machine learning algorithms to optimize process parameters or conditions but are not used within the context of adapting the part’s geometry. Accordingly, for the objective of combining topology optimization with process assurance, well suited machine learning models are not yet identified. The task of searching a well-suited machine learning model for a new problem is difficult, since selecting algorithms and adjacent hyperparameters can be extremely costly. Automated machine learning systemizes the searching or selecting procedure [18, 19]. An efficient method for a neural architecture search system provides the work of Jin et al., where the search space is explored via morphing the neural network architectures guided by a Bayesian optimization algorithm [19]. Automated machine learning approaches do not guarantee to outperform human guided modelling, but they can provide a helpful assistance tool in the modelling process.

1.2 Approach

The objective of this article is to use a geometric feature-based metamodel to replace the casting simulation within a topology optimization process assurance framework, as we show in Fig. 1.

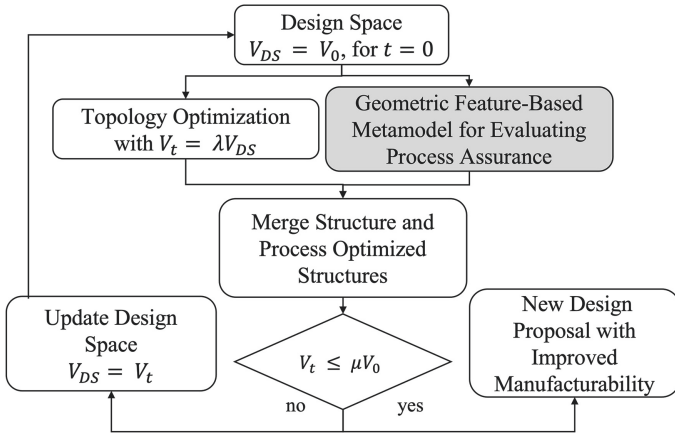


Fig. 1. Metamodel assisted framework for combined topology optimization and process assurance based on the workflow presented in [10]. A topology optimization with an initial Volume V_0 and a target Volume $V_t = \mu V_0$ with volume constraint μ and step length λ is conducted parallel to a casting simulation for process assurance. The latter is replaced by the metamodel (shaded in grey).

In this article, we replace the time-consuming casting simulation by a geometric feature-based metamodel for process assurance. Subsequently, we use implicit modeling to modify the design proposals based on the given evaluation criterion along with the topology optimization results. We apply this approach to a cantilever beam and a traverse link, shown in Fig. 2, and compare the modified design proposals with simulation-based geometry modification.

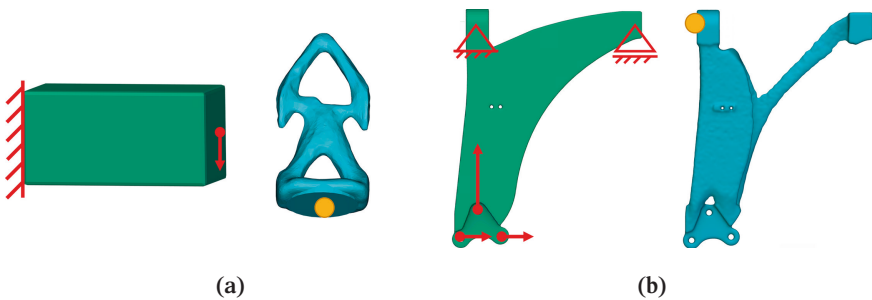


Fig. 2. Overview of the design space (green) and optimized design proposals without integrated process assurance (blue) for the two test examples. (a) Cantilever beam; (b) Traverse link. The load case is sketched in red on the design spaces, while the ingate position is marked orange on the design proposals.

2 Materials and Methods

2.1 Metamodel Architecture

In this article, we used artificial neural networks as metamodels. For preparing the data, building, optimizing and evaluating the metamodel, we used the python libraries numpy [20], seaborn [21], pandas [22, 23], matplotlib [24, 25], scikit-learn [26], scikit-optimize [27], TensorFlow[28, 29], Keras [30, 31] and Auto-Keras [19]. Figure 3 shows the general architecture of the artificial neural network.

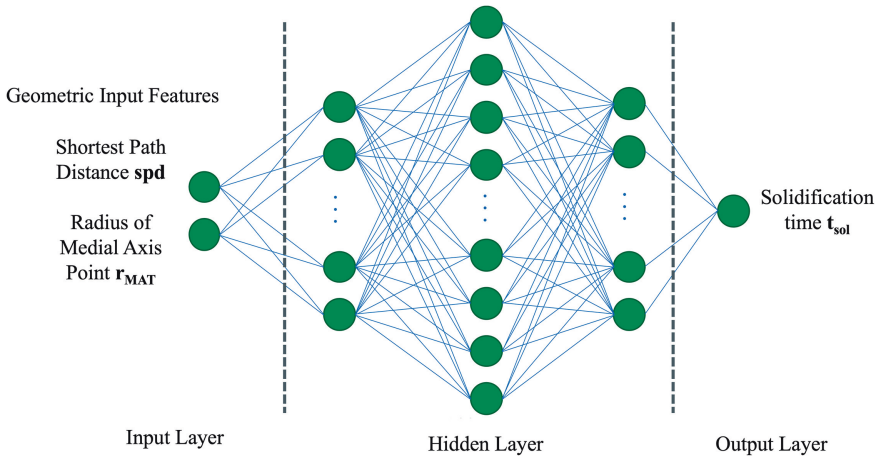


Fig. 3. Architecture of the baseline feed forward multilayer perceptron. Two geometric input features are used to estimate the solidification time in low-pressure die castings.

The baseline model was a dense feed forward multilayer perceptron neural network. We optimized the architecture and the hyperparameters using a two-step automated machine learning approach. The output parameter is the solidification time, which we obtained from previously made casting simulations. As geometric input features, we used shortest path distances, which provide the shortest distance between the ingate and any point in the geometry, and the radii of the medial axis points obtained by the medial axis transform, which represent the part thickness along the solidification path. The calculation of both geometric input features is shortly explained in the following.

Medial Axis Transform. The medial axis transform is a surface skeletonization technique for three dimensional objects, which is calculated from the Voronoi diagram. Every point on the medial axis is associated to an internal ball that touches the part's surface but does not penetrate it [32]. The radii of the balls provide therefore the part thickness for every point on the medial axis. We used the implementation presented in our previous work [32].

Dijkstra's Shortest Path. Dijkstra's shortest Path algorithm begins at a starting node and gradually selects the currently most favorable paths via the nodes on a graph that can be reached next [33]. We used the shortest path to calculate the shortest flow distances between the ingate and all points on the medial axis, thus providing qualitative information how fast a point can possibly be reached by the melt.

Data Preparation. For training and testing the models, we used a dataset containing 220,000 pairs of shortest path distance, radius of medial axis point, and solidification time. The data was split into 200,000 training and 20,000 test data.

Automated Machine Learning. The two-step automated machine learning approach consists of Bayesian optimization supported search for an well suited architecture and a subsequent hyperparameter optimization using the hyperband algorithm [34]. The objective for both optimization tasks was to minimize the mean squared error. During both optimizations, a 5-fold cross-validation was used on the training data. Table 1 shows the selected parameters summarized.

Table 1. Summary of the chosen settings for two-step automated machine learning. The objective function was in both cases the mean squared error (MSE).

	Algorithm	Objective	Iterations
Architecture Search	Bayesian Optimization	MSE	100
Hyperparameter Optimization	Hyperband	MSE	250

2.2 Evaluation of Process Assurance

The process assurance is evaluated using the evaluation criterion developed in our previous work for low-pressure die castings [10]. By assuming a directional solidification in low-pressure die casting, the ratio of the solidification time (t_{sol}) and the shortest path distance (spd) should be descending along the solidification path, which we evaluated using the following equation:

$$QL = \log \left(\frac{t_{sol}}{spd} \right) \quad (1)$$

2.3 Modification of the Design Space

To modify the design spaces, we used the software nTopology (Version 3.35, nTopology Inc., New York, NY, USA) that allows an implicit representation of geometries. Based on the density values of the topology optimization, we first create a volume lattice for activated (high-density, material) and deactivated (low-density, holes) elements, which strut diameters are further adapted by the evaluation criterion point map of QL. We illustrate this procedure in Fig. 4.

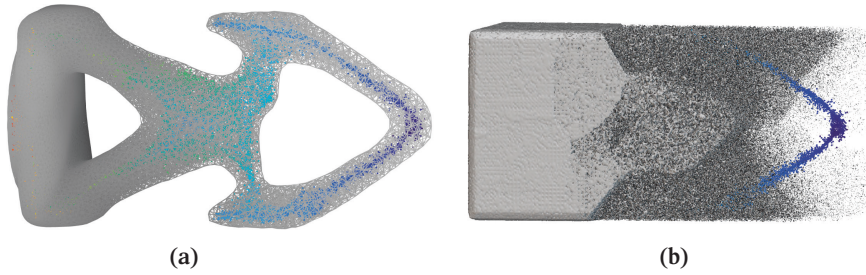


Fig. 4. Volume lattices for (a) activated elements and (b) deactivated elements. The colored point map represents the evaluation criterion's value on each cell of the design proposal.

This procedure allows further the filtering of geometric features according to the lattice density. Subsequently, the activated geometry and the deactivated geometry are filtered, smoothed, and merged, as we show in Fig. 5. The result is a modified design proposal with increased manufacturability.

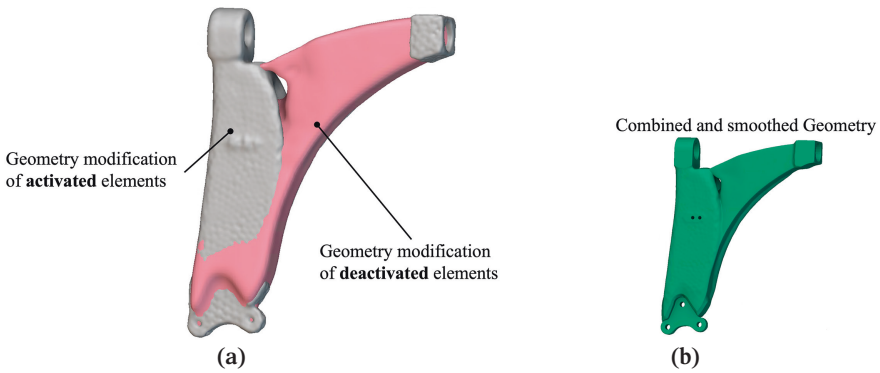


Fig. 5. Illustration of the reconstruction process: (a) The filtered meshes for activated (grey) and deactivated (red) elements are merged. (b) Combined and smoothed geometry which represents the final design proposal.

3 Results and Discussion

3.1 Metamodel Performance

We show the results of the metamodel performance in Fig. 6 by plotting the predicted solidification times ($y_{\text{predicted}}$) against the true – or target – solidification times (y_{target}). For the cantilever the coefficient of determination (R^2) reached 0.79, while the

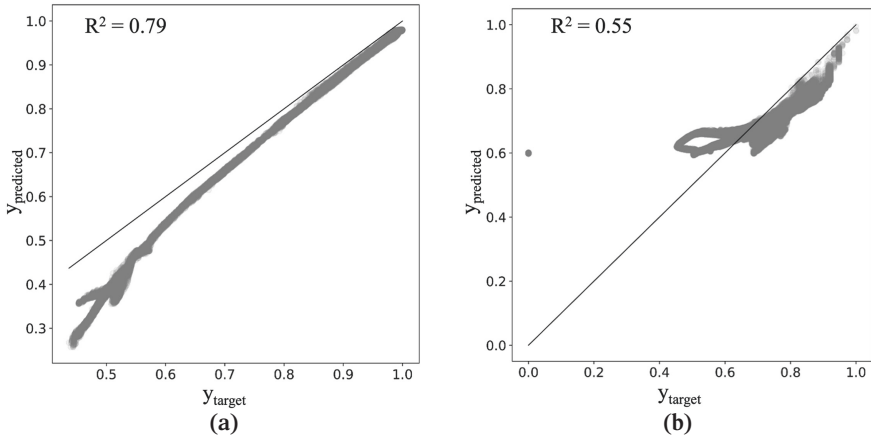


Fig. 6. Results for the metamodel performance for (a) cantilever beam; (b) traverse link.

prediction for the traverse link reached 0.55. This result is plausible due to the cantilever's simpler geometry.

However, since the metamodel's objective is an acceptable estimation rather than a high-fidelity prediction, the achieved results show sufficient accuracy for both test examples.

3.2 Evaluation of Modified Design Proposals

To evaluate the modified design proposals, the QL was first calculated using the predicted solidification times. In the next step the calculated QL modifies the geometries according to the process described in Sect. 2.3. In the following the final metamodel-based design proposals are compared to the simulation-based design proposals. Figure 7 shows that for the cantilever beam the difference volume between metamodel and simulation design proposal is close to zero (Fig. 7b). Accordingly, the presented metamodel-based approach led to equivalent design proposals.

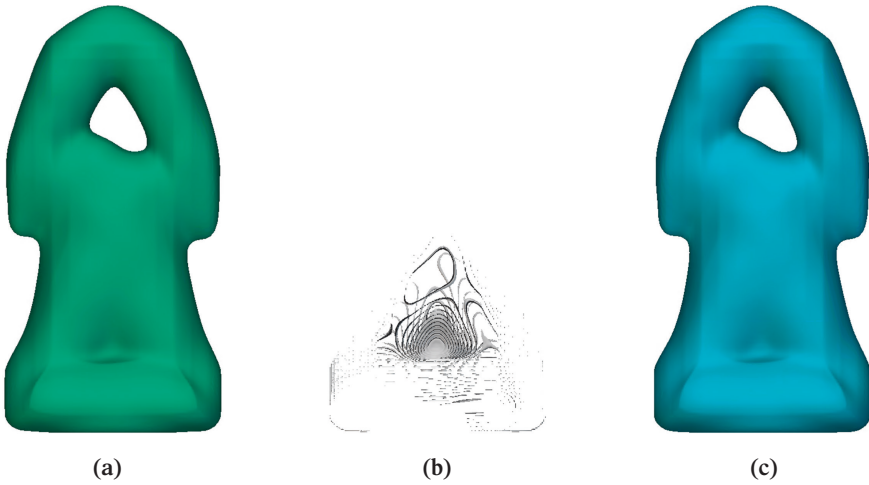


Fig. 7. Comparison of the final cantilever beam design proposals for (a) metamodel-based; (c) simulation-based. (b) represents the difference Volume between both design proposals.

The comparison of the traverse link design proposals shows Fig. 8. In this case deviations between simulated and predicted solidification were significantly greater, which also resulted in deviation of the modified design proposals. In both design proposals, the reconstruction aimed to better connect the box with drill hole on the left side (Fig. 2b) to the rest of the geometry. Interestingly, the metamodel's deviations led to a design proposal, which – geometrically – looks superior the simulation-based proposal.

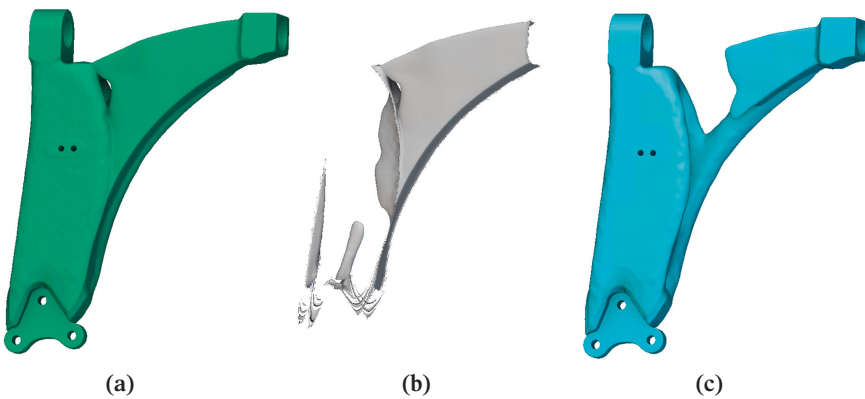


Fig. 8. Comparison of the final traverse link design proposals for (a) metamodel-based; (c) simulation-based. (b) represents the difference Volume between both design proposals.

We attribute this effect to the evaluation criterion calculation on the activated elements and further extrapolation of the values on the deactivated elements. Accordingly, we conclude that also for the traverse link the metamodel resulted in an at least equivalent design proposal, though a smaller coefficient of determination.

4 Summary

In this article, we presented an incorporation of process assurance evaluation into a topology optimization framework, using geometric feature-based metamodel. While building the metamodel, we used a two-stage automated machine learning approach which helped to systematically exploit the parameter space and, thus, identifying a well-suited model architecture and hyperparameters.

The built metamodel reduced the needed time for process assurance evaluation from multiple hours to a few seconds while maintaining a sufficient prediction accuracy. The automated geometry reconstruction further mitigated weak points in the design proposal provided by the isolated topology optimization.

Therefore, our presented approach realizes an efficient incorporation of process assurance into structural optimization and fosters its further dissemination and exploitation of lightweight potentials.

Acknowledgements. The Authors would like to thank the German Research Foundation (DFG) for financial support under grant number 434348474.

References

1. Heilmeier, F., Goller, D., Opritescu, D., Thoma, C., Rieg, F., Volk, W.: Support for Ingate Design by Analysing the Geometry of High Pressure Die Cast Geometries Using Dijkstra's Shortest Path Algorithm. *AMR* 1140, 400–407. (2016). <https://doi.org/10.4028/www.scientific.net/AMR.1140.400>.
2. Franke, T., Fiebig, S., Bartz, R., Vietor, T., Hage, J., vom Hofe, A.: Adaptive topology and shape optimization with integrated casting simulation. In: *EngOpt 2018 Proceedings of the 6th international conference on engineering optimization*, H. C. Rodrigues, J. Herskovits, C. M. Mota Soares, A. L. Araújo, J. M. Guedes, J. O. Folgado, F. Moleiro, and J. F. A. Madeira, Eds. Cham: Springer International Publishing, 2019, 1263–1277. https://doi.org/10.1007/978-3-319-97773-7_109.
3. Rieser, J., Zimmermann, M.: Topology optimization of periodically arranged components using shared design domains. *Struct. Multidiscip. Optim.* **65**(1), 1–22 (2021). <https://doi.org/10.1007/s00158-021-03125-5>
4. Sigmund, O., Maute, K.: Topology optimization approaches. *Struct. Multidiscip. Optim.* **48**(6), 1031–1055 (2013). <https://doi.org/10.1007/s00158-013-0978-6>
5. Harzheim, L., Graf, G.: A review of optimization of cast parts using topology optimization: I - Topology optimization without manufacturing constraints. *Struct. Multidisc. Optim.* **30**(6), 491–497 (2005). <https://doi.org/10.1007/s00158-005-0553-x>

6. Wang, J., Sama, S.R., Manogharan, G.: Re-thinking design methodology for castings: 3D sand-printing and topology optimization. *Int. J. Metalcast.* **13**(1), 2–17 (2018). <https://doi.org/10.1007/s40962-018-0229-0>
7. Harzheim, L., Graf, G.: A review of optimization of cast parts using topology optimization: II-Topology optimization with manufacturing constraints. *Struct Multidisc Optim* **31**(5), 388–399 (2006). <https://doi.org/10.1007/s00158-005-0554-9>
8. Vatanabe, S.L., Lippi, T.N., de Lima, C.R., Paulino, G.H., Silva, E.C.N.: Topology optimization with manufacturing constraints: A unified projection-based approach. *Adv. Eng. Softw.* **100**, 97–112 (2016). <https://doi.org/10.1016/j.advengsoft.2016.07.002>
9. Wang, Y., Kang, Z.: Structural shape and topology optimization of cast parts using level set method: Structural shape and topology optimization of cast parts using level set method. *Int. J. Numer. Meth. Engng* **111**(13), 1252–1273 (2017). <https://doi.org/10.1002/nme.5503>
10. Rosnitschek, T., Erber, M., Hartmann, C., Volk, W., Rieg, F., Tremmel, S.: Combining structural optimization and process assurance in implicit modelling for casting parts. *Materials* **14**(13), 3715 (2021). <https://doi.org/10.3390/ma14133715>
11. Hornik, K., Stinchcombe, M., White, H.: Multilayer feedforward networks are universal approximators. *Neural Netw.* **2**(5), 359–366 (1989). [https://doi.org/10.1016/0893-6080\(89\)90020-8](https://doi.org/10.1016/0893-6080(89)90020-8)
12. Weigold, M., Ranzau, H., Schaumann, S., Kohne, T., Panten, N., Abele, E.: Method for the application of deep reinforcement learning for optimised control of industrial energy supply systems by the example of a central cooling system. *CIRP Ann.* **70**(1), 17–20 (2021). <https://doi.org/10.1016/j.cirp.2021.03.021>
13. Nakai, M.E., Aguiar, P.R., Guillard, H., Bianchi, E.C., Spatti, D.H., D’Addona, D.M.: Evaluation of neural models applied to the estimation of tool wear in the grinding of advanced ceramics. *Expert Syst. Appl.* **42**(20), 7026–7035 (2015). <https://doi.org/10.1016/j.eswa.2015.05.008>
14. Caggiano, A., Nele, L.: Fraunhofer Joint Laboratory of Excellence on Advanced Production Technology (Fh-J_LEAPT UniNaples) P.le Tecchio 80, Naples 80125, Italy, Department of Industrial Engineering, University of Naples Federico II, Naples, Italy, and Department of Chemical, Materials and Industrial Production Engineering, University of Naples Federico II, Naples, Italy, “Artificial Neural Networks for Tool Wear Prediction Based on Sensor Fusion Monitoring of CFRP/CFRP Stack Drilling,”. *IJAT* **12**(3), 275–281 (2018). <https://doi.org/10.20965/ijat.2018.p0275>
15. Krimpenis, A., Benardos, P.G., Vosniakos, G.-C., Koukouvtiki, A.: Simulation-based selection of optimum pressure die-casting process parameters using neural nets and genetic algorithms. *Int J Adv Manuf Technol* **27**(5–6), 509–517 (2006). <https://doi.org/10.1007/s00170-004-2218-0>
16. Kittur, J.K., Manjunath Patel, G.C., Parappagoudar, M.B.: Modeling of pressure die casting process: An artificial intelligence approach. *Int. J. Metalcast.* **10**(1), 70–87 (2015). <https://doi.org/10.1007/s40962-015-0001-7>
17. Shahane, S., Aluru, N., Ferreira, P., Kapoor, S.G., Vanka, S.P.: Optimization of solidification in die casting using numerical simulations and machine learning. *J. Manuf. Process.* **51**, 130–141 (2020). <https://doi.org/10.1016/j.jmapro.2020.01.016>
18. Yao, Q. et al.: Taking Human out of Learning Applications: A Survey on Automated Machine Learning. [arXiv:1810.13306](https://arxiv.org/abs/1810.13306) [cs, stat], (2019) Accessed 5 Feb 2022. <http://arxiv.org/abs/1810.13306>
19. Jin, H., Song, Q., Hu, X.: Auto-Keras: An efficient neural architecture search system. In: Proceedings of the 25th ACM SIGKDD international conference on knowledge discovery & data mining, Anchorage AK USA, 1946–1956, July 2019. <https://doi.org/10.1145/3292500.3330648>

20. Harris, C.R., et al.: Array programming with NumPy. *Nature* **585**(7825), 357–362 (2020). <https://doi.org/10.1038/s41586-020-2649-2>
21. Waskom, M.: seaborn: statistical data visualization. *JOSS* **6**(60), 3021 (2021). <https://doi.org/10.21105/joss.03021>
22. Reback, J. et al.: pandas-dev/pandas: Pandas 1.0.3. Zenodo (2020). <https://doi.org/10.5281/ZENODO.3715232>
23. McKinney, W.: Data Structures for Statistical Computing in Python. Paper presented at the Python in science conference, Austin, Texas, 56–61 (2010). <https://doi.org/10.25080/Majora-92bf1922-00a>
24. Caswell, T.A. et al.: matplotlib/matplotlib: REL: v3.5.1. Zenodo (2021). <https://doi.org/10.5281/ZENODO.5773480>
25. Hunter, J.D.: Matplotlib: A 2D graphics environment. *Comput. Sci. Eng.* **9**(3), 90–95 (2007). <https://doi.org/10.1109/MCSE.2007.55>
26. Pedregosa, F., et al.: Scikit-learn: Machine learning in python. *JMLR* **12**, 2825–2830 (2011)
27. Head, T. et al.: Scikit-Optimize/Scikit-Optimize: V0.5.2. Zenodo (2018). <https://doi.org/10.5281/ZENODO.1207017>
28. TensorFlow Developers: TensorFlow. Zenodo (2021). <https://doi.org/10.5281/ZENODO.5799851>
29. Abadi, M. et al.: TensorFlow: Large-scale machine learning on heterogeneous systems. (2015). <https://www.tensorflow.org/>
30. Chollet, F., et al.: Keras. (2015). <https://keras.io>
31. O'Malley, T. et al.: KerasTuner. (2019). <https://github.com/keras-team/keras-tuner>
32. Erber, M., Rosnitschek, T., Hartmann, C., Alber-Laukant, B., Tremmel, S., Volk, W.: Geometry-based assurance of directional solidification for complex topology-optimized castings using the medial axis transform. *Computer-Aided Design* 103394 (2022). <https://doi.org/10.1016/j.cad.2022.103394>
33. Dijkstra, E.W.: A note on two problems in connexion with graphs. *Numer. Math.* **1**(1), 269–271 (1959). <https://doi.org/10.1007/BF01386390>
34. Li, L., Jamieson, K., DeSalvo, G., Rostamizadeh, A., Talwalkar, A.: Hyperband: A novel bandit-based approach to hyperparameter optimization. 52



CAD Reconstruction of Watertight Surface Meshes Using Polycube Parameterization and Subdivision Surfaces

Moustafa Alsayed Ahmad¹(✉), Majid Hojjat¹, and Kai-Uwe Bletzinger²

¹ BMW Group, Petuelring 130, 80809 München, Germany
{Moustafa.Alsayed-Ahmad, Majid.Hojjat}@bmw.de

² Technische Universität München, Arcisstraße 21, 80333 München, Germany
kub@tum.de

Abstract. Topology optimization can produce optimal geometries in terms of the simulated physics, but they are primarily represented as watertight surface meshes which enclose a volume. As a result, they cannot be incorporated directly into the design process, which is mainly carried out using Computer Aided Design (CAD) data. To enable the integration into the design process, an interpretation step is required to convert these surface meshes into CAD models, known as CAD reconstruction. However, CAD reconstruction proved to be time-consuming and makes it difficult to deploy topology optimization in the industry and in generative design when carried out manually. This contribution presents a method to automatically construct a CAD model starting from a watertight surface mesh. First, the surface mesh is divided into different components based on its topology, each component being called a part. Second, each part is segmented using polycube segmentation methods, where each segment is called a patch. The patches of each part form a polycube, which can be easily meshed using coarse quad elements. The quad meshes of all parts are then assembled to form a quad mesh, which approximates the original watertight surface mesh. The quad mesh serves as a basis for the generation of the subdivision surface. The resulting subdivision surface approximates well the original surface mesh and is flexible for further post-processing or modification in later steps.

Keywords: Computer Aided Design (CAD) · CAD reconstruction · Topology Optimization · Polycube parameterization · Subdivision surfaces

1 Introduction

Converting meshes into CAD models has always been an active area of research. This process may also be known as CAD reconstruction or reverse-engineering. In this process, the raw positional data (position of the vertices of the mesh or the point cloud) gets interpreted and a series of parametric curves and surfaces are constructed to approximate it. A list of scientific developments and publications have been made in this field. In [12] the authors detect surface features on the mesh obtained from topology optimization, then use those features as a basis for the generation of biquartic surface splines; whereas in [17] the authors detect surface types or regions using curvature information and try to compute feature lines between those regions and fit NURBS surfaces over them. Both [12] and [17] rely on computing surface features or types, which is not robust and is strongly sensitive to the mesh quality. In [18], the authors propose a semi-automatic procedure of extracting a curve-skeleton approximating the topology of the underlying mesh and then manually constructing a CAD model (mainly through sweep-operations). This approach has been implemented in an automatic way in [13] and [6]; however, the surface complexity around the curve-skeleton is very low. [21] and [16] rely on similar procedure of approximating the mesh using medial surfaces (include curve- and surface-skeletons), then automatically constructing the CAD model around the skeleton-curves; in [21] the authors use CSG-models (Constructive Solid Geometry models) to approximate the mesh abstracted by the curve-skeleton and in [16] the authors perform offsetting and manipulation of the surface-skeleton to generate a solid geometry. These approaches lack the ability of reconstructing surfaces, which are not tubular or exhibit simple cross section around its skeleton. An approach presented by [11] relies on a voxel structure to re-mesh the given mesh from topology optimization and then using marching cubes to generate a surface mesh and converting every single shell element into a CAD patch, which is very robust but generates a lot of CAD patches which makes the CAD model hard to manipulate. On the other hand, there have been numerous developments from the industry in implementing automatic CAD reconstruction workflows. One approach implemented by CATIA V5 [7] is to some extent similar to [11]; however, as pointed out before, it has the disadvantage that it produces high number of surface patches; the models are also hard to edit and they exhibit no natural parametrization (like feature lines where there is a ridge, or a feature line separating two distinct components in the geometry). Another method, which is followed by many software developers like nTopology, Synera and Autodesk [15] performs re-meshing of the given mesh to create a quad mesh, then the quad elements are merged according to some geometric criteria with adjacent quad elements to form bigger patches, until either there are no more quad elements to merge, or no merge satisfies the specified geometric criteria. This approach is very robust since it can work for all geometries regardless of whether they are watertight or not. However, if one wishes to edit the CAD model produced by this approach, the full underlying quad mesh needs to be edited which is not easy. Furthermore, this approach relies on pure local geometric criteria to assess the merge quality of the quad

elements, and this is why the resulting patches can be small even though the underlying surface is almost flat, or the patches can be large even though the underlying surface is highly curved. In addition, the patches do not represent a natural partitioning of the topology optimization mesh since the feature lines don't necessarily partition two semantic parts or two ridges.

In this paper, we want to develop a new approach, which produces CAD models that contain few CAD patches and are easy to edit and manipulate in a commercial software. In addition, we don't desire the CAD model to exactly match the mesh from topology optimization, since we perform afterwards shape optimization to detect the optimal form. These three criteria form the guidelines in designing our CAD reconstruction workflow as presented in Fig. 1.

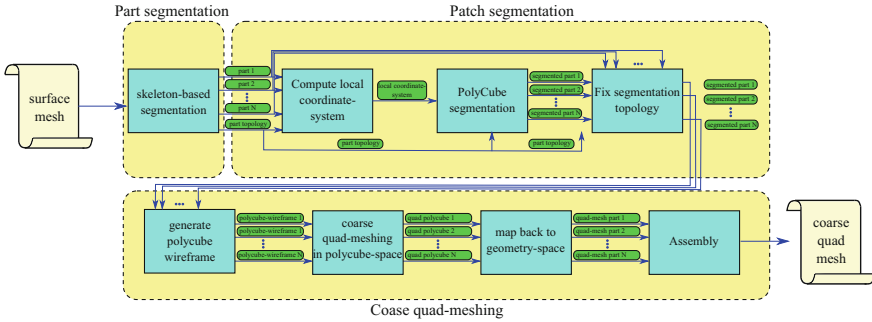


Fig. 1. Workflow of reconstructing a watertight surface mesh and creating a coarse quad dominated mesh (base mesh) to be later used as a base to the subdivision surface

2 Methods

In this section, the method of constructing a subdivision surface based on a given mesh resulting from topology optimization is presented and discussed. The workflow proposed to construct a coarse quad mesh or also called a base mesh (basis of the subdivision surface) from a given watertight surface mesh is given in Fig. 1.

The workflow starts by partitioning the surface mesh into multiple part meshes; these part meshes are denoted by the set $M_{\mu}^{\text{part}}(V, F)$, $\mu = 1, \dots, N^{\text{part}}$ (see Sect. 2.1). Then each part M_{μ}^{part} is partitioned further using a polycube parameterization method into patches, which are denoted by the set $M_{\mu, \nu}^{\text{patch}}(V, F)$, $\nu = 1, \dots, N^{\text{patch}}$ (see Sect. 2.2). Polycube parameterization is first proposed in [20] for texture mapping, and it segments a given surface mesh into a union of cubes of equal size, see Fig. 2. These cubes are all aligned to an orthogonal coordinate system, and each color in Fig. 2 represents a distinct patch. A collection of patches $M_{\mu, \nu}^{\text{patch}}$ such that $\cup_{\nu} M_{\mu, \nu}^{\text{patch}} = M_{\mu}^{\text{part}}$ is converted

to a polycube structure using a polycube deformation method [22]. We denote the polycube structure M_μ^{PC} , where for each part we get a corresponding polycube structure. The coarse quad mesh is generated based on the polycube structure and then it gets mapped back to the shape of the corresponding part (see Sect. 2.3). The coarse quad mesh is then used as the base mesh for the generation of the subdivision surface (see Sect. 2.4). Lastly, the subdivision surface is post-processed, so that its deviation from the input surface mesh or also called the target mesh is minimal (see Sect. 2.5).

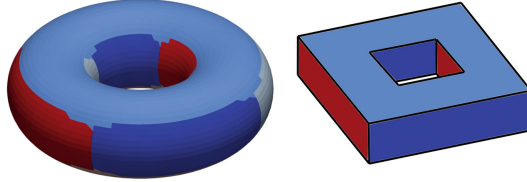


Fig. 2. (left) A given surface mesh with polycube parameterization (right) the corresponding polycube structure

2.1 Part Segmentation

Part segmentation is the process of partitioning a surface mesh into multiple parts $M_\mu^{\text{part}}(V, F)$, $\mu = 1, \dots, N^{\text{parts}}$, where each part is a set of faces $S_\mu^{\text{part}} = [F_1, F_2, \dots, F_{N^{\text{part-faces}}}]$ where $N^{\text{part-faces}}$ here is the number of faces within part μ . Each part is represented either as a part mesh $M_\mu^{\text{part}}(V, F)$ or a part segmentation with the set $S_\mu^{\text{part}}(F)$. In [9], they performed part segmentation before patch segmentation using polycube parameterization. This approach has an advantage in that it reduces the number of corner vertices in the polycube structure that is generated later. The reason behind this is that polycube structures are aligned with the axes, so even if a straight geometry, such as a cylinder with small variations in its shape, is segmented using a single polycube structure, it may have more than eight corner points. This is because a perfect cylinder can be ideally segmented with a single polycube structure with eight corner points. Hence, if we seek a polycube structure with few corner-points, we can partition the surface mesh into multiple parts, in such a way each part is aligned to a certain coordinate system. One can either manually partition the surface mesh into multiple parts or use curve-skeletons-based segmentation [2] to achieve that.

2.2 Patch Segmentation

After all part meshes $M_\mu^{\text{part}}(V, F)$ are extracted, each one of them gets further segmented using a polycube segmentation method. The method of choice in this paper is the Harmonic Boundary-Enhanced Centroidal Voronoi Tessellation or

short HBECVT [10]. For a visual discription of the patch segmentation procedure see Fig. 3. The procedure of patch segmentation starts by extracting local coordinate systems of each extracted part mesh and the interface (described by the vertices shared by two part meshes $M_{i,j}^{\text{interface}}(V) = M_i^{\text{part}} \cap M_j^{\text{part}}$, where parts i and j are adjacent). For either the part meshes or the interfaces, their corresponding local coordinate system is computed using the Principal Component Analysis (PCA). The PCA-method computes the axes of the local coordinate system by determining the eigenvectors of the following covariance-matrix:

$$\mathbf{C} = \frac{1}{1 - N_{\text{part-vertices}}} (\mathbf{V} - \bar{\mathbf{V}}) \otimes (\mathbf{V} - \bar{\mathbf{V}}), \quad \mathbf{V} \in M_{\mu}^{\text{part}}(V, F) \quad \text{or} \quad \mathbf{V} \in M_{i,j}^{\text{interface}}(V) \quad (1)$$

where $\bar{\mathbf{V}} = \frac{1}{N_{\text{part-vertices}}} \sum_{i=1}^{N_{\text{part-vertices}}} \mathbf{V}_i$, \mathbf{V}_i is the i th row of the matrix \mathbf{V} of vertex-coordinates within the part mesh or the interface. The eigenvectors of the covariance-matrix \mathbf{C} sorted from the smallest to the largest eigenvalue determines the local x,y and z axes of the local coordinate system as shown in Fig. 3b. Now the faces of each part mesh are segmented by minimizing the following energy-functional with respect to the labels \mathbf{c} :

$$E(\mathbf{n}_F, \mathbf{c}) = \sum_{i=1}^{N_{\text{part-faces}}} \left[\frac{L}{\sum_{l=1}^L d(\mathbf{n}_{F_i}, \mathbf{c}_l)^{-1}} \right], \quad (2)$$

where \mathbf{n}_F is the matrix of face-normals, \mathbf{c} is matrix of six labels of axis vectors aligned to the previously computed local coordinate system $(+x, -x, +y, -y, +z, -z)$, L is six (number of labels), \mathbf{n}_{F_i} is the i th face's normal vector and \mathbf{c}_l is the l th label vector. Faces, which are adjacent to each other and are assigned to the same label vector are called a patch. The function $d(\mathbf{n}_{F_i}, \mathbf{c}_l)$ mathematically described in Eq. 3 computes in term 1 the deviation of the face's normal vector to the label's vector and penalizes in term 2 the adjacent face from having a different label compared to the label the current face has, where $\tilde{n}_{i,l}$ is the number of faces in the neighborhood of face F_i , which have a label different that the assigned label to face F_i and λ is a multiplication-parameter and has the value 0.5. In addition, two more terms were added to the original formulation in [10]. Term 3 prevents the current face F_i from being assigned to a label when at least one of its neighboring faces has an opposite label (for example $+x$ and $-x$), where \tilde{o}_i equals the number of faces in the neighborhood of face F_i , which have opposite label compared to face F_i . Term 4 prevents the face sitting next to an interface from having a label which has a label vector parallel to the x-axis of the interface, where \tilde{a}_i equals the number of those faces. p is the penalty-factor and equals 10^5 .

$$d(\mathbf{n}_{F_i}, \mathbf{c}_l) = \sqrt{\underbrace{\|\mathbf{n}_{F_i} - \mathbf{c}_l\|^2}_{\text{term 1}} + \lambda \underbrace{(\tilde{n}_{i,l})}_{\text{term 2}} + p \left(\underbrace{\tilde{o}_i}_{\text{term 3}} + \underbrace{\tilde{a}_i}_{\text{term 4}} \right)} \quad (3)$$

So far if we perform the patch segmentation as discussed, we would get a segmentation as shown in Fig. 3c; however, one can notice that at the interface,

the patch segmentation of parts 1 and 2 are not matching. This is due to the fact that the local coordinate system of parts 1 and 2 are not aligned. To solve this problem, we propose in this paper blending the local coordinate systems of parts 1 and 2 to the interface's local coordinate system. At Fig. 3d the blending function is plotted at the rightmost side, and this blending distance is a user parameter and is chosen in this paper equal 4 times the average element size.

2.3 Coarse Quad Meshing

After extracting the patch segmentation using HBECVT-method (polycube-based segmentation), we need now to convert each part into a polycube structure and perform coarse quad meshing upon it, then the vertices of the coarse quad mesh can be easily mapped from the polycube structure to the part mesh.

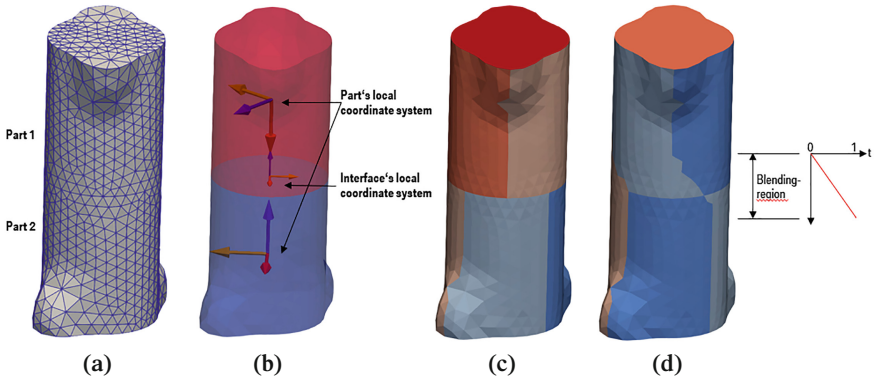


Fig. 3. Patch segmentation procedure; (a) given a surface mesh (b) a part segmentation is computed and local coordinate systems for each part and the interface between the parts is determined (c) patch segmentation using HVECVT-method without using the blending procedure (d) patch segmentation using the HBECVT-method using the blending procedure

To generate a polycube structure, we use the method proposed in [22], which takes a part mesh with its patch segmentation and deforms the part mesh in such a way that the faces' normal vectors are aligned to the normal vectors dictated by the label vectors assigned to each face by minimizing the energy in Eq. 2. This deformation is formulated as a successive solution of a linear system of equations; for full details of the deformation-procedure see [22]. The number of iterations needed to re-solve this linear system in our paper is 20. After deforming the mesh, we get a mesh similar to the one shown in Fig. 4a.

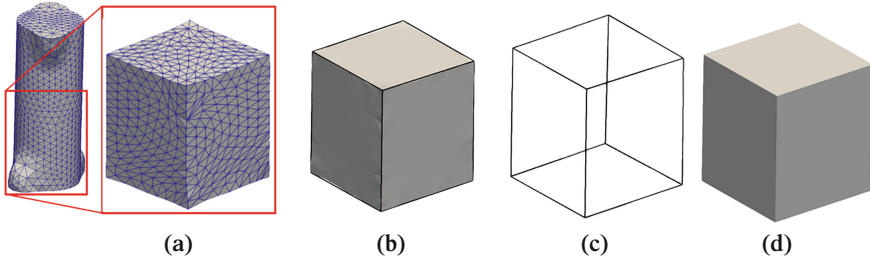


Fig. 4. Procedure of generating the polycube structure; (a) the surface mesh is deformed according to [22] (b) the wireframe connecting corner-vertices is constructed (c) the wireframe is deformed to form the polycube structure (d) quad elements are created based on the polycube structure

Mesh deformation according to [22] does not produce perfect polycube structures (see not fully aligned faces in Fig. 4b). A solution would be to extract the corresponding wireframe structure, which consists of vertices located at the mesh's corner-vertices (vertices surrounded by three or more distinct labels) and edges connecting them. Each edge of the wireframe structure lies between two perpendicular label vectors. For a perfect polycube structure, those wireframe edges should be perpendicular to the two labels-vectors. After the mesh-deformation and the extraction of the wireframe structure, the edges are not in general perpendicular to the two label vectors. To make them so, we deform the wireframe until the edge-vectors are perpendicular to the two label vectors; see Fig. 4c.

After having a perfectly aligned wireframe structure, quad elements are created on each patch and then their vertices are mapped back the shape of the surface mesh. These quad elements are computed by firstly using triangulation algorithms for 2-dimensional polygons, then triangles are merged together according to some mesh quality criteria to form quad elements; see Fig. 4d.

After each part mesh is meshed with quad elements, they get assembled to form the coarse quad mesh or the base mesh needed for the generation of the subdivision surface.

2.4 Generation of Subdivision Surfaces

Now given the coarse quad mesh generated by the methods presented in Sect. 2.3, which also will be called the base mesh, the subdivision surface is created using the Catmull-Clark method [4]. The Catmull-Clark method is chosen since the base mesh is quad dominated; however, for triangular meshes one can use the Loop subdivision method [14]. The Catmull-Clark method is based on the idea of successively adding new vertices at the middle of quad faces and at the middle of each edge and then determining the position of those new vertices and modifying the position of the original ones based on some sort of averaging scheme as shown in Fig. 5a-d; the reader is advised to read [4] to see full details of the averaging

schemes used. Those refined meshes shown in Fig. 5b–d are called subdivision meshes and the subdivision surface is the limit of those subdivision meshes as the number of subdivision iterations reaches infinity.

The vertex position of the base mesh is represented by the $(N \times 3)$ matrix $\mathbf{V}^{(0)}$, where 0 indicates that this is the original vertex position or the 0th subdivision iteration. The successive vertex positions using the Catmull-Clark method can be computed using the following linear operation:

$$\mathbf{V}^{(i+1)} = \mathbf{S}^{(i)} \cdot \mathbf{V}^{(i)}, \tag{4}$$

where $\mathbf{S}^{(i)}$ is called the subdivision matrix used in the i th iteration, and it is a rectangular matrix, since the number of vertices at the subdivision iteration $i + 1$ is larger than the number of vertices at the subdivision iteration i . The subdivision-matrix which gets multiplied by the original vertex positions $\mathbf{V}^{(0)}$ to get $\mathbf{V}^{(i+1)}$ can be computed as follows:

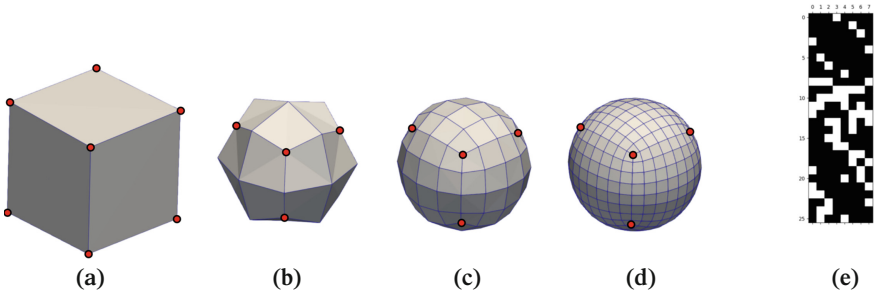


Fig. 5. Generation of subdivision meshes (a) starting from the base mesh (b) 1st subdivision iteration (c) 2nd subdivision iteration (d) 3rd subdivision iteration, where the red vertices are the original vertices getting averaged according to the Catmull-Clark method and (e) represents the non-zero structure of the subdivision matrix $\mathbf{S}^{(0)}$, where the non-zero entries are represented as black squares

$$\mathbf{S}_i = \prod_{j=0}^i \mathbf{S}^{(j)}. \tag{5}$$

This subdivision matrix will be used in the following section to map variation in quantities back and forth between the base mesh and the subdivision mesh; for the non-zero structure of the subdivision matrix $\mathbf{S}^{(0)}$ (after one subdivision iteration of the base mesh shown in Fig. 5a) see Fig. 5e.

2.5 Post-processing of Subdivision Surfaces

After the subdivision surface is computed, we get a surface close to the surface mesh which originated from topology optimization or as we call it the target mesh. However, this subdivision surface due to the subdivision averaging does

shrink and it deviates from the target mesh; see Fig. 6. To mitigate this deviation, a post-processing step is proposed to modify the base mesh in such a way that the subdivision surface becomes as close to the target mesh as possible. To do that we use node-based (or vertex-based) shape optimization in order to modify the vertex position of the base mesh. Node-based shape optimization uses the vertex position as the design variable. In order to modify the base mesh such that the corresponding subdivision surface is as close as possible to the target-mesh, we propose to maximize the volume of the subdivision surface $f_{\text{volume}}(\mathbf{V}^{(i)})$ and use a packaging-constraint $f_{\text{packaging}}(\mathbf{V}^{(i)})$ (using the penalty-method with penalty-factor p equals 10^5) to limit the volume-growth in such a way that the subdivision surface stays contained within the target mesh. An additional constraint on the thickness $f_{\text{thickness}}(\mathbf{V}_j^{(0)})$ of the base mesh is imposed to prevent self-penetration during the optimization. The optimization-statement is presented in Eq. 6.

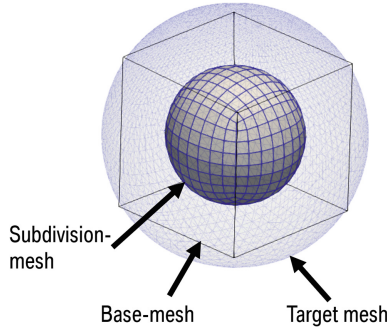


Fig. 6. Deviation of the subdivision mesh from the target mesh (to be approximated)

$$\begin{aligned}
 & \text{minimize} && - f_{\text{volume}}(\mathbf{V}^{(i)}) + p \cdot f_{\text{packaging}}(\mathbf{V}^{(i)}), && (6) \\
 & \text{design variables} && \mathbf{V}^{(0)} \\
 & \text{s.t} && \mathbf{V}^{(i)} = \mathbf{S}_i \cdot \mathbf{V}^{(0)}, \\
 & \text{s.t} && f_{\text{thickness}}(\mathbf{V}_j^{(0)}) \geq t_{\text{min}} \quad \forall \mathbf{V}_j^{(0)} \in \mathbf{V}^{(0)}
 \end{aligned}$$

The detailed formulation for the functions f_{volume} , $f_{\text{packaging}}$ and $f_{\text{thickness}}$ along with their shape derivative is presented in Eqs. 7 [5], 8 and 9 respectively.

$$f_{\text{volume}}(\mathbf{V}^{(i)}) = \frac{1}{6} \sum_{\mu, \nu, \gamma \in F^{(i)}} \mathbf{v}_{\mu}^{(i)} \cdot (\mathbf{v}_{\nu}^{(i)} \times \mathbf{v}_{\gamma}^{(i)}), \quad \frac{\partial f_{\text{volume}}(\mathbf{V}^{(i)})}{\partial \mathbf{V}_j^{(i)}} = A(\mathbf{V}_j^{(i)}) \mathbf{n}(\mathbf{V}_j^{(i)}), \quad (7)$$

where $A(\mathbf{V}_j^{(i)})$ is the vertex area of the vertex $\mathbf{V}_j^{(i)}$, and $\mathbf{n}(\mathbf{V}_j^{(i)})$ is the normal vector of the vertex $\mathbf{V}_j^{(i)}$

$$f_{\text{packaging}}(\mathbf{V}^{(i)}) = \sum_{\mu \in \mathcal{V}^{(i)}} \max((\mathbf{V}_\mu^{(i)} - \tilde{\mathbf{V}}_\mu^{(i)}) \cdot \mathbf{n}^{\text{target mesh}}(\tilde{\mathbf{V}}_\mu^{(i)}), 0), \quad (8)$$

$$\frac{\partial f_{\text{packaging}}(\mathbf{V}^{(i)})}{\partial \mathbf{V}_j^{(i)}} = \mathbf{n}^{\text{target mesh}}(\tilde{\mathbf{V}}_\mu^{(i)}),$$

where $\tilde{\mathbf{V}}_\mu^{(i)}$ is the closest point projection (CPP) of the vertex $\mathbf{V}_\mu^{(i)}$ on the target mesh, and $\mathbf{n}^{\text{target mesh}}(\tilde{\mathbf{V}}_\mu^{(i)})$ is the normal vector at the CPP-point $\tilde{\mathbf{V}}_\mu^{(i)}$.

$$f_{\text{thickness}}(\mathbf{V}_j^{(i)}) = (\mathbf{V}_j^{(i)} - \mathbf{V}_j^{(i),*}) \cdot -\mathbf{n}(\mathbf{V}_j^{(i)}), \quad \frac{f_{\text{thickness}}(\mathbf{V}_j^{(i)})}{\mathbf{V}_j^{(i)}} = -\mathbf{n}(\mathbf{V}_j^{(i)}), \quad (9)$$

where $\mathbf{n}(\mathbf{V}_j^{(i)})$ is the normal vector at the vertex $\mathbf{V}_j^{(i)}$ and $\mathbf{V}_j^{(i),*}$ is the intersection of the ray originating at $\mathbf{V}_j^{(i)}$ in the direction of $-\mathbf{n}(\mathbf{V}_j^{(i)})$.

The shape gradient of the functions is needed since the node-based shape optimization will be carried out using a gradient-based algorithm called the Relaxed Gradient Projection (RGP) [1]. The RGP method computes the search direction in the design space of the position of the base mesh's vertices by considering the gradient of both the objective function and the active constraints. Since the functions 7, 8 are represented as a function of the subdivision mesh's vertices, a mapping of the gradients between the subdivision mesh and base mesh is needed. This mapping is realized using the subdivision matrix \mathbf{S}_i in Eq. 5. To map search direction (in base mesh space) to shape change of vertices of the subdivision mesh, the following relation is used:

$$\delta \mathbf{V}^{(i)} = \mathbf{S}_i \cdot \delta \mathbf{V}^{(0)}, \quad (10)$$

and for mapping shape gradient from the space of vertices of the subdivision mesh to the space of vertices of the base mesh, the following relation is used:

$$\frac{\partial f}{\partial \mathbf{V}^{(i)}} = \mathbf{S}_i^T \frac{\partial f}{\partial \mathbf{V}^{(0)}}. \quad (11)$$

The relation represented in Eqs. 10 and 11 are similar to the forward- and backward-mapping operations used in the Vertex Morphing method to map between the design space and the geometry space [3, 8].

3 Results and Discussion

Two industrial test-cases are used to demonstrate the workflow discussed in Sect. 2. They both are bracket structures developed for different purposes. Both part- and patch-segmentation are shown in Figs. 7a and 8a.

The different colors shown in Figs. 7a and 8a represent different patches, where each patch gets meshed using quad- and triangular elements to result in the coarse meshes (represented as a wireframe) shown in Fig. 7b and 8b. The

subdivision mesh is obtained after two subdivision iterations of the base mesh represented by the black wireframe. The influence of the postprocessing step detailed in Sect. 2.5 is shown in Fig. 7b and 8b, where it can clearly be seen that the subdivision meshes are getting closer to the target mesh (represented as a transparent grey-surface). However a low deviation of the subdivision mesh from the target-surface is hard to achieve due to the fact that the base mesh has low number of vertices (or degrees of freedom) to allow for richer deformation of the subdivision mesh. Nevertheless, the RGP-method finds a way to exploit the existing degrees of freedom to get as close to the target mesh as possible; see the sharp feature at the left side of the right leg in Fig. 8b.

Looking at Fig. 7c and 8c one sees clearly the benefit of using subdivision surfaces for representing the CAD-models as it gives very smooth transition between the patches, which is clearly observed by the light-reflections. In CATIA V5, we only need to import the base mesh, and the software generates instantly a corresponding subdivision surface. The subdivision surface can be modified in terms of topology and shape very easily using the readily available tools in CATIA V5.

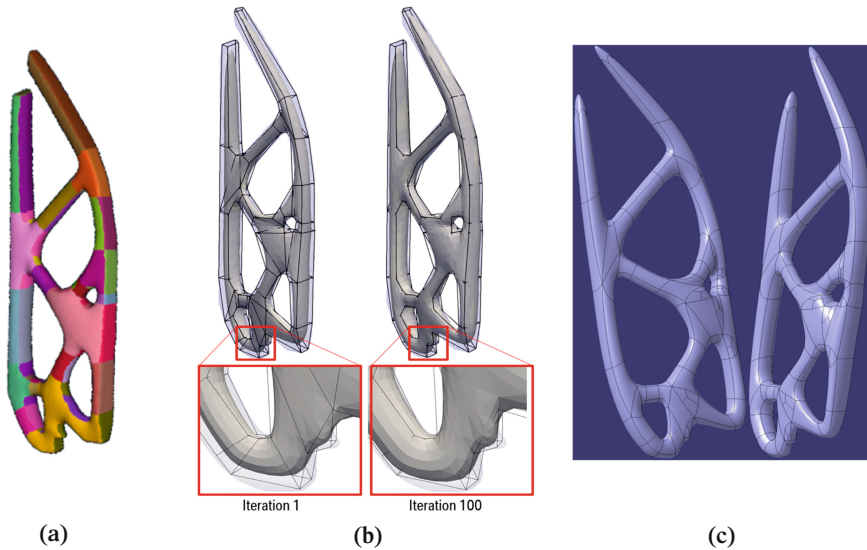


Fig. 7. Bracket-structure (a) after part- and patch-segmentation, (b) after undergoing shape-optimization with 100 iterations to bring its shape close to the target mesh (transparent grey) and (c) represented as subdivision surface in CATIA V5 [19]

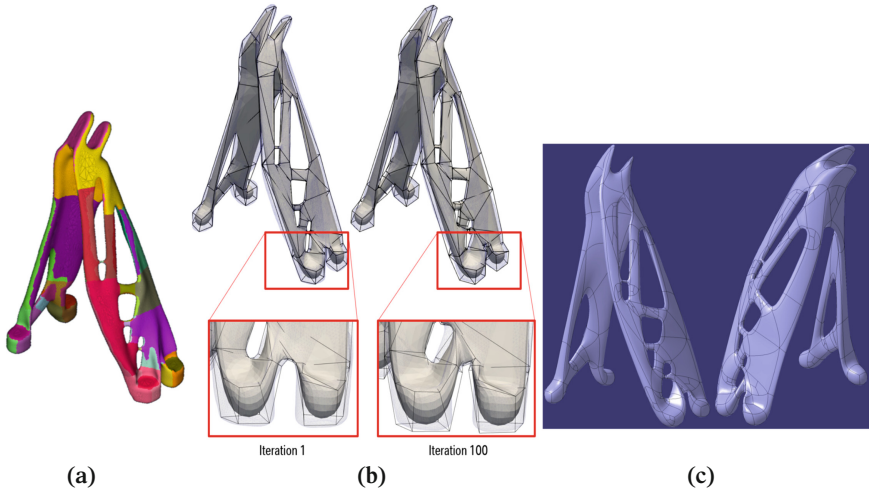


Fig. 8. Holder-structure (a) after part- and patch-segmentation, (b) after undergoing shape-optimization with 100 iterations to bring its shape close to the target mesh (transparent grey) and (c) represented as subdivision surface in CATIA V5 [19]

4 Conclusion

This paper presents a workflow to perform CAD reconstruction of watertight surface meshes obtained from topology optimization using subdivision surfaces. The workflow is designed such that it generates subdivision surfaces that have low number of vertices in its base mesh and are easy to modify and adjust in a commercial software. The core idea of the proposed workflow is the hierarchical segmentation of the mesh using part- and patch segmentation. To be able to model complex geometries, the polycube parameterization method is chosen to compute the patches in patch segmentation, which form the basis of the quad- and triangular elements of the base mesh. The workflow's post-processing stage, which eliminates the need for the CAD reconstruction to have a complex parameterization (with a large number of degrees of freedom in the base mesh), is an additional advantage. Instead, it uses shape optimization during post-processing to make up for the base mesh's low number of degrees of freedom. With this method, the target mesh and computed subdivision surface are intended to be tightly aligned. The workflow is proved to work on two industrial topology optimization meshes, where the subdivision surfaces are close to the target meshes and can be very easily modified and adjusted using the CATIA V5 environment.

References

1. Antonau, I., Hojjat, M., Bletzinger, K.U.: Relaxed gradient projection algorithm for constrained node-based shape optimization. *Struct. Multidiscip. Optim.* **63**(04), 1633–1651 (2021)

2. Au, O., Tai, C.-L., Chu, H.-K., Cohen-Or, D., Lee, T.-Y.: Skeleton extraction by mesh contraction. *ACM Trans. Graph.* **27**(08) (2008)
3. Bletzinger, K.U.: A consistent frame for sensitivity filtering and the vertex assigned morphing of optimal shape. *Struct. Multidiscip. Optim.* **49**(01), 873–895 (2014)
4. Catmull, E., Clark, J.: Recursively generated b-spline surfaces on arbitrary topological meshes. *Comput. Aided Des.* **10**(6), 350–355 (1978)
5. Crane, K., de Goes, F., Desbrun, M., Schröder, P.: Digital Geometry Processing with Discrete Exterior Calculus. CM SIGGRAPH 2013 courses. SIGGRAPH '13. ACM, New York. <https://www.cs.cmu.edu/~kmc Crane/Projects/DDG/> (2013)
6. Denk, M., Rother, K., Paetzold, K.: Fully automated subdivision surface parametrization for topology optimized structures and frame structures using euclidean distance transformation and homotopic thinning. In: Pflingstl, S., Horoschenkoff, A., Höfer, P., Zimmermann, M. (eds.) *Proceedings of the Munich Symposium on Lightweight Design 2020*, pp. 18–27. Springer, Berlin (2021)
7. Dautre, P.-T., Morretton, E., Vo, T.H., Marin, P., Pourroy, F., Prudhomme, G., Vignat, F.: Comparison of Some Approaches to Define a CAD Model From Topological Optimization in Design for Additive Manufacturing, pp. 233–240. Springer International Publishing, Cham (2017)
8. Hojjat, M., Stavropoulou, E., Bletzinger, K.-U.: The vertex morphing method for node-based shape optimization. *Comput. Methods Appl. Mech. Eng.* **268**(01), 494–513 (2014)
9. Hu, K.: Centroidal Voronoi Tessellation with Applications in Image and Mesh Processing 7. Carnegie Mellon University, Pittsburgh (2016)
10. Hu, K., Zhang, Y.J., Liao, T.: Surface segmentation for polycube construction based on generalized centroidal voronoi tessellation. *Comput. Methods Appl. Mech. Eng.* **316**, 280–296 (2017). Special Issue on Isogeometric Analysis: Progress and Challenges
11. Joshi, S., Medina, J.C., Menhorn, F., Reiz, S., Rueth, B., Wannerberg, E., Yurova, A.: CAD-Integrated Topology Optimization. Technical University of Munich, Munich (2016)
12. Koguchi, A., Kikuchi, N.: A surface reconstruction algorithm for topology optimization. *Eng. Comput.* **22**, 1–10 (2006)
13. Kresslein, J., Haghghi, P., Park, J., Ramnath, S., Sutradhar, A., Shah, J.J.: Automated cross-sectional shape recovery of 3d branching structures from point cloud. *J. Comput. Des. Eng.* **5**(3), 368–378 (2018)
14. Loop, C.: Smooth Subdivision Surfaces Based on Triangles. University of Utah, Salt Lake City (1987)
15. Marinov, M., Amagliani, M., Barback, T., Flower, J., Barley, S., Furuta, S., Charrot, P., Henley, I., Santhanam, N., Finnigan, G., Meshkat, S., Hallet, J., Sapun, M., Wolski, P.: Generative design conversion to editable and watertight boundary representation. *Comput. Aided Des.* **115**, 194–205 (2019)
16. Mayer, J., Wartzack, S.: A concept towards automated reconstruction of topology optimized structures using medial axis skeletons. In: Pflingstl, S., Horoschenkoff, A., Höfer, P., Zimmermann, M. (eds.) *Proceedings of the Munich Symposium on Lightweight Design 2020*, pp. 28–35. Springer, Berlin (2021)
17. Park, J.M., Lee, B.C., Chae, S.W., Kwon, K.Y.: Surface reconstruction from fe mesh model. *J. Comput. Des. Eng.* **6**(2), 197–208 (2019)

18. Weber, C., Husung, S., Cantamessa, M., Cascini, G., Marjanovic, D., Graziosi, S. (eds.): International Conference on Engineering Design (ICED 15) 6, 235–244. ISBN: 978-1-904670-69-8. ISSN: 2220-4334. <https://www.designsociety.org/publication/37838/FEATURE+BASED+INTERPRETATION+AND+RECONSTRUCTION+OF+STRUCTURAL+TOPOLOGY+OPTIMIZATION+RESULTS> (2015)
19. Dassault Systèmes. Catia
20. Tarini, M., Hormann, K., Cignoni, P., Montani, C.: Polycube-Maps. *ACM SIGGRAPH 2004 Papers* (2004)
21. Yin, G., Xiao, X., Cirak, F.: Topologically robust cad model generation for structural optimisation. *Comput. Methods App. Mech. Eng.* **369**, 113102 (2020)
22. Zhao, H., Lei, N., Li, X., Peng, Z., Ke, X., Xianfeng, G.: Robust edge-preserving surface mesh polycube deformation. *Comput. Visual Media* **4**, 01 (2018)



Optimization of Lightweight Vehicle Components for Crashworthiness Using Solution Spaces

Ying Lin, Paolo Ascia^(✉), and Fabian Duddeck

Technische Universität München, Arcisstraße 21, 80333 München, Germany
paolo.ascia@tum.de, ge64lij@mytum.de, duddeck@tum.de
<https://www.epc.ed.tum.de/cm>

Abstract. In this work, we investigate the potential of using the solution space as constraint in an optimization problem of newly developed components: we propose a workflow to find the best compromise between the mass of a component and its crashworthiness. We provide a link between the solution space methodology - a systems engineering method for crashworthiness - and the shell thicknesses of newly developed components to better exploit the potential of the method itself. To do so, we use the Efficient Global Optimization (EGO) algorithms, constrained by the output of the solution space method - force intervals. By optimizing all components involved in a frontal impact we understand the limitations of the proposed workflow: despite the solution space method providing a guideline to develop all components independently, this is not always possible. We show to what extent one can use the solution space as a constraint in an optimization problem, hence, quickly finding the best compromise between independent development, mass reduction and crashworthiness.

Keywords: Lightweight optimization · Solution space · Crashworthy design · Efficient global optimization

1 Introduction

Designing new cars is a challenging process, driven by multiple objectives of often conflicting needs; for example, the necessity of reducing the total mass to reduce fuel consumption challenges the safety of the vehicle. Instead of solving these conflicts from a general perspective, a common practice is to cascade the different requirements on a component level and find a solution in a simpler setup. When assembling the entire vehicle, the solutions provided in the simpler cases manage to overcome the general conflicts. For an overview of methods to cascade requirements refer to [1]. We want to re-design the front of the Honda

Accord [2] to find better designs of the components in the front of the car that is lighter and also crashworthy. To do this, we pick the solution space method for cascading the results and individually find an optimal compromise.

The solution space methodology was introduced to help the development in the early stage design and to allow each component to be developed independently of each other [3]. Nowadays it is more and more common to constrain an optimization problem with the solution space. This allows for optimizing multiple components in parallel while fulfilling all general requirements. Most of these applications involve linear problems: designing the drivetrain of a new electric vehicle [4, 5], or engineering a robotic arm [6].

The success of these applications inspired us to attempt a similar scheme for designing new crashworthy and lightweight components. This involves using the methodology for a non-linear problem. Despite the developments in the solution space methodology for crashworthiness [7, 8], the non-linearity of the problem has limited the practical applications. An early example can be found in [9]. However, it is limited. In it, only one component is optimized and both the objective and the constraints are oriented to fulfil only the solution space. Therefore, understanding from it whether or not the methodology can handle the problems of the development for crash and solve the conflicts originating from opposing requirements is difficult. In this work, we better explore this field of application by re-designing all the components of the Honda Accord [2] that dissipate most of the energy in a crash. This reveals to us the capabilities of applying the solution space method for optimizing crash components under conflicting requirements.

The paper is structured to first introduce in Sect. 2 the solution space methodology and, in Sect. 3, the algorithm chosen to perform the optimization. In Sect. 4, we present how we define our optimization problem. Finally, in Sect. 5, we showcase the results and reflect on them.

2 Defining the Solution Space

To use the solution space to constrain an optimization problem, we first need to compute the space itself. In literature, two different methods are available: the direct [7] and the indirect method [9]. We work with the direct method. More specifically, we follow the steps of the example presented in [10].

The direct method requires a simplified model that captures the loadcase and the requirements of crashworthiness. To set up the necessary model we use the Deformation Space Method described in [11]. The Deformation Space Model we consider—corresponding to the Honda Accord of 2013 [2]—is composed of 7

components divided into two loadpaths, as shown in Fig. 1. The loadpaths are divided into a total of 31 sections, each one of a fixed deformation length. Each component can, therefore, deform the length pre-defined in the Deformation Space Model.

The second element needed to compute the solution space is the definition of crashworthiness. In our case, we borrow the definition provided by NHTSA [12]:

- The vehicle must absorb a minimum quantity of energy corresponding to its kinetic energy at the speed of 56 km/h;
- The vehicle must decelerate at a maximum rate of 300 m/s²;
- The components must deform in a specific order, from the front to the back.

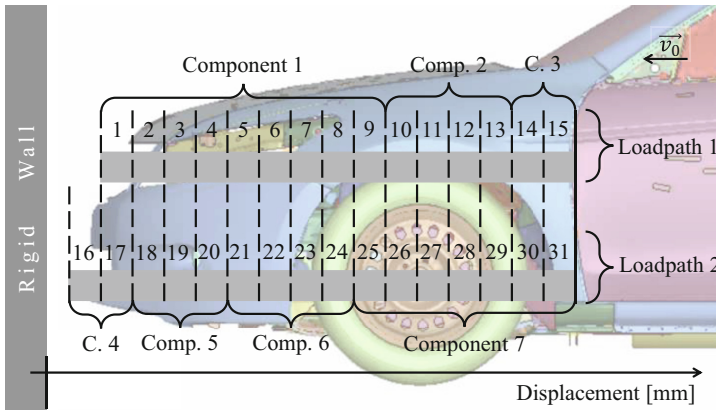


Fig. 1. Geometry Space Model computed according to the method presented in [11]

With both the Deformation Space Model and the crashworthiness definition we compute the solution space. Since the details are available in [10], we present in Fig. 2 only the final results. In this figure, the white area represents the solution space, whereas the grey area represents the space where the solution is not crashworthy.

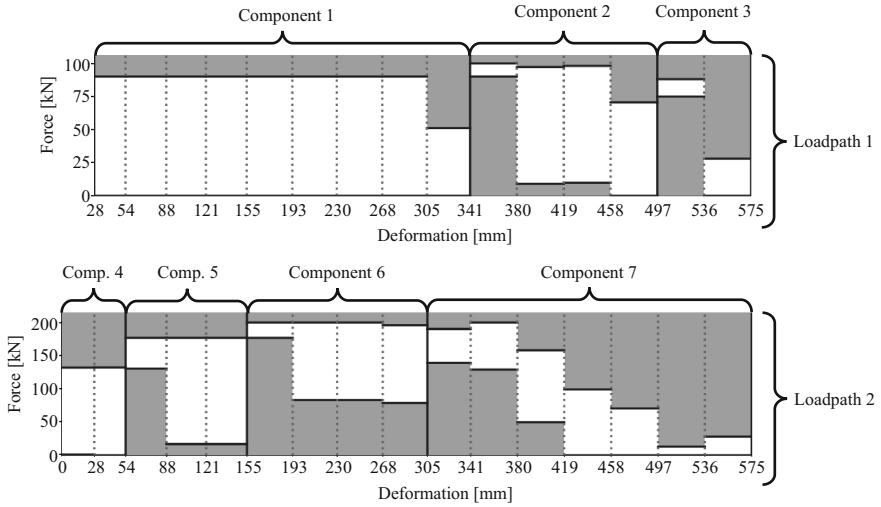


Fig. 2. Solution space computed according to the methodology described in [10]

3 Efficient Global Optimization

As we stated at the beginning, we want to optimize the new components using the constraints from the solution space. Our choice for the optimization algorithm is the Efficient Global Optimization (EGO) one. This approach is ideal when the number of affordable evaluations for the optimization itself is limited. EGO was initially proposed in [13] for constrained and in [14] for unconstrained, single objective optimization. It is a response surface method with adaptive sampling, which is well-suited for the optimization of expensive black-box functions, like finite element simulations. It is designed such that it approximates the response surface and finds the optimum with a low number of sample points. This is possible by identifying promising regions on the response surface and sampling selectively only in these areas. To do so, the algorithm utilizes a Gaussian Process Regression. It takes advantage of the fact that a stochastic process model predicts the response surface and the uncertainty of this prediction. On top of this, an adaptive sampling scheme is used to locate promising regions where to find the minimum of the objective function.

4 Problem Formulation

Let us now look at our optimization problem and how we constrained it with the solution space. In this section, we define an objective function compatible with the solution space methodology, how we are evaluating it, and how to define the constraints.

The solution space is represented on a force-deformation plane in Fig. 2. It is, thus, convenient to relate the objective function to at least the force or the deformation (to explicit the relation to the solution space), and the mass of the component (to find a lightweight component). We use the Specific Energy Absorption (SEA), which is a function of the mass of the component m , the total deformation of the component s , and the force absorbed F :

$$SEA = F \cdot s/m. \quad (1)$$

To evaluate this function we, therefore, need a way to test how much force each component absorbs, how much it deforms, and how much it weighs. If on one hand the weight of the component can be easily retrieved, on the other hand, the force and deformation need to be measured with an experiment. The test of our choice is the drop-tower setup. In this setup, a component is fully locked at one end, meanwhile the other end is crushed by a heavy impactor, as showcased in Fig. 3. We run this experiment in a virtual environment: a finite element simulation. From the simulation, we can measure and plot the force against the deformation. The area under this curve is the numerator of the SEA function.

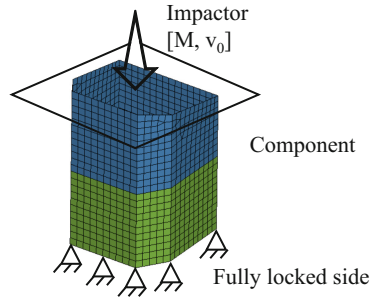


Fig. 3. Example of drop-tower test used to measure the force-deformation curve from the components; in this figure component 4 is represented.

Lastly, we need to define the constraints linked to the solution space methodology. As it can be seen in Fig. 2, the solution space is defined by an upper force limit F_{upper}^i and a lower force limit F_{lower}^i at each i -th section. We can use them to set a constraint on the force measured during the drop-tower test. To ease the problem, we consider the average absorbed force over the i -th section. On top of this, we need to set an equality constraint on the total deformation length because it is fixed in the Deformation Space Model. The last constraint is on the thicknesses of the walls of the components. These can vary between 0.5 mm and 3.0 mm for manufacturability reasons. Therefore, also the mass of the component is indirectly constrained by these manufacturability limits.

We can finally formulate our optimization problem:

$$\left\{ \begin{array}{l} \min \quad f(x) = -SEA \\ \text{s.t.} \quad g_1(x) = F^i(u_x) - F_{upper}^i \leq 0, \\ \quad \quad g_2(x) = F^i(u_x) - F_{lower}^i \geq 0, \\ \quad \quad h_1(x) = u_x - u_x^{target} = 0, \\ \quad \quad x_L \leq x \leq x_U. \end{array} \right. \quad (2)$$

where $f(x)$ is the objective function, $g_1(x)$ and $g_2(x)$ are the inequality constraints, $h_1(x)$ is the equality constraint; $F^i(u_x)$ is the average value of the measured force over the i -th section, F_{upper}^i and F_{lower}^i are respectively the upper and lower limit of the solution space in the i -th section, u_x is the measured deformation, and u_x^{target} is the deformation defined in the Deformation Space Model. Lastly, x_L and x_U represent the manufacturability limits imposed on the thicknesses x of the walls

Given the objective function, we can solve this optimization problem per each component in parallel. In other words, we optimize each component independently, thanks to the properties of the solution space method.

5 Results and Discussion

Let us now look at the results so obtained. As shown in the figures below, of the 7 components we optimize only 3 to fulfil the constraints of the computed solution space, see Figs. 4, 7 and 8. These three components are all positioned at the front, while the others are all towards the back. The violations on these other 4 components are, however, not severe, see Figs. 5, 6, 9 and 10.

Consider the solution space formulation. As one can read in [10], the space represented is only the feasible and independent one. Hence, part of the feasible space (i.e. the space where all conditions for crashworthiness are fulfilled) is not represented in the solution space. Since the violations are mild, all components are very likely to be in this feasible space. We, however, still do not have a consistent method to test just for the feasibility of the solution.

Moreover, the fact that the components violating the constraints are towards the rear can be related to the fact that the inter-dependencies between different components are nearly not considered. On one side, the Deformation Space Model captures the influences between different components only if related to the order of deformation. On the other side, the drop-tower test was designed for components at the front (e.g. crashboxes like the one shown in Fig. 3), and not for bigger components like number 7 or 3. It is well known that components like these are affected by the surrounding parts. Nevertheless, for these components, there is still no commonly used test for properly measuring the force-deformation curves. The work in [15] and further developed in [16] attempts to address this problem. They propose a methodology to better represent the conditions under which these bigger components deform. However, the method is still too young for us to use it in the work here presented.

We are not able, as of now, to assess if changing the test would positively benefit the solution found. It is too early to conclude if the violations are due to the test performed or to the independence condition imposed by the solution space methodology.

6 Conclusion

All in all, the development of a new car is a complicated process. The key factor to success is finding proper compromises between opposing requirements. The solution space methodology can help the development to find these tradeoffs. However, the application in the crashworthiness field is still full of difficulties. In this work, we tackle one of these conflicts: we optimize the components at the front of a car to find a lightweight and crashworthy design. To this purpose, we define an objective oriented at reducing the weight of the component, while we use the solution space to constrain the problem and ensure the crashworthiness. The results of this approach are not completely positive: out of 7 components, 3 are successfully optimized inside the solution space. These 3 components are all positioned at the very front of the car. At this point in time, we can say that the solution space methodology can help to develop all components with a limited amount of interactions with the neighboring systems (i.e.: the components at the front).

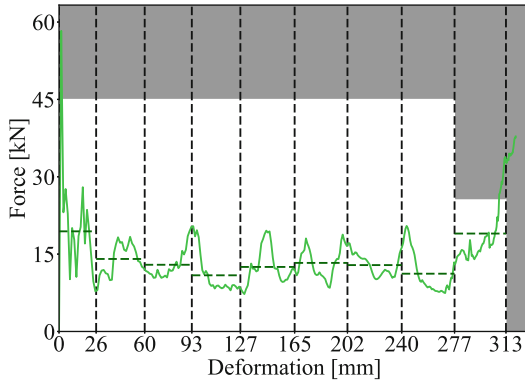


Fig. 4. Force-deformation curve measured from the successfully optimized component 1: in light green the measured signal, in dark green the average value over each section ($F^i(u_x)$).

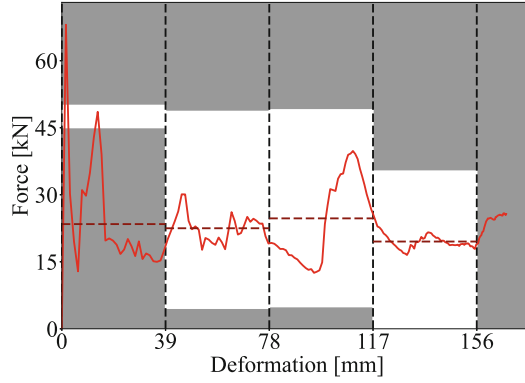


Fig. 5. Force-deformation curve measured from the failed optimized component 2: in light red the measured signal, in dark red the average value over each section ($F^i(u_x)$).

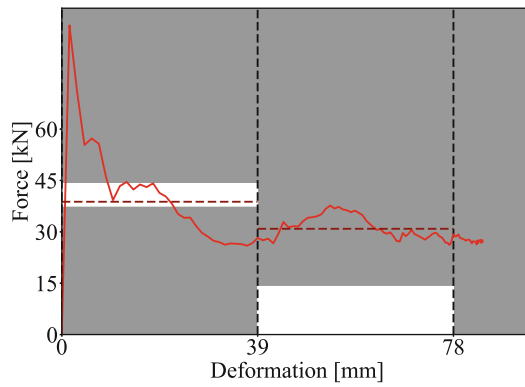


Fig. 6. Force-deformation curve measured from the failed optimized component 3: in light red the measured signal, in dark red the average value over each section ($F^i(u_x)$).

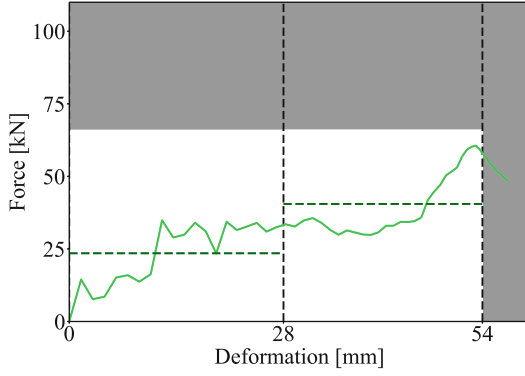


Fig. 7. Force-deformation curve measured from the successfully optimized component 4: in light green the measured signal, in dark green the average value over each section ($F^i(u_x)$).

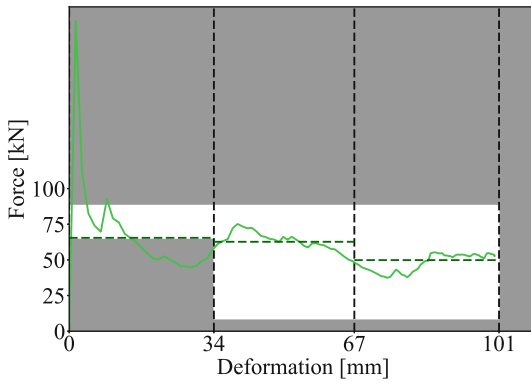


Fig. 8. Force-deformation curve measured from the successfully optimized component 5: in light green the measured signal, in dark green the average value over each section ($F^i(u_x)$).

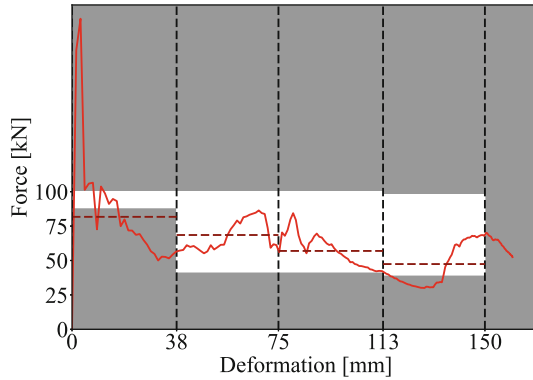


Fig. 9. Force-deformation curve measured from the failed optimized component 6: in light red the measured signal, in dark red the average value over each section ($F^i(u_x)$).

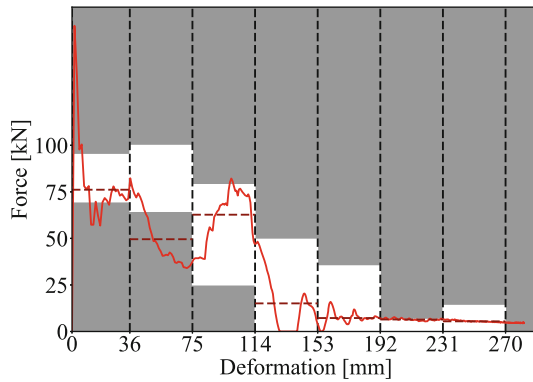


Fig. 10. Force-deformation curve measured from the failed optimized component 7: in light red the measured signal, in dark red the average value over each section ($F^i(u_x)$).

Acknowledgment. This paper summarized the results of the thesis [17] completed at the School of Engineering and Design of the Technical University of Munich (TUM), Germany.

The project leading to this application has received funding from the European Union's Horizon 2020 research and innovation program under the Marie Skłodowska-Curie grant agreement No 955393.

References

1. Zimmermann, M., Weck, O.d.: Formulating engineering systems requirements. In: Handbook of Engineering Systems Design, pp. 1–52. Springer (2022)
2. NHTSA.: Crash simulation vehicle models. <https://www.nhtsa.gov/crash-simulation-vehicle-models> (2022)

3. Zimmermann, M., Hoessle, J.E.v.: Computing solution spaces for robust design. *Int. J. Num. Methods Eng.* **94**(3), 290–307 (2013)
4. Rötzer, S., Berger, V., Zimmermann, M.: Cost optimization of product families using solution spaces: application to early-stage electric vehicle design. *Proc. Des. Soc.* **2**, 583–592 (2022)
5. Lopez, J.G.C., Stumpf, J., Freitag, H.-G.: Robust design optimization of nonlinear powertrain mounting systems with solution space engineering. In: Desmet, W., Pluymers, B., Moens, D., Neeckx, S. (Eds.) *Proceedings of ISMA2022 International Conference on Noise and Vibration Engineering and USD2022 International Conference on Uncertainty in Structural Dynamics*. KU Leuven, , Belgium, pp. 4788–4802. ISBN: 9789082893151. *Optimization of Lightweight Components with Solution Spaces 11* (2022)
6. Krischer, L., Zimmermann, M.: Decomposition and optimization of linear structures using meta models. *Struct. Multidiscip. Optim.* **64**(4), 2393–2407 (2021)
7. Fender, J., Duddeck, F., Zimmermann, M.: Direct computation of solution spaces. *Struct. Multidiscip. Optim.* **55**(5), 1787–1796 (2017)
8. Daub, M., Duddeck, F., Zimmermann, M.: Optimizing component solution spaces for systems design. *Struct. Multidiscip. Optim.* **61**(5), 2097–2109 (2020)
9. Fender, J.: *Solution Spaces for Vehicle Crash Design*. PhD thesis. Technische Universität München (2013)
10. Daub, M.: *Optimizing Flexibility for Component Design in Systems Engineering under Epistemic Uncertainty*. PhD thesis. Technische Universität München (2020)
11. Lange, V.A., Fender, J., Song, L., Duddeck, F.: Early phase modeling of frontal impacts for crashworthiness: from lumped mass-spring models to deformation space models. *Proc. Inst. Mech. Eng. Part D: J. Automob. Eng.* **233**(12), 3000–3015 (2019)
12. NHTSA.: *Laws and regulations*. <https://www.nhtsa.gov/lawsregulations> (2022). Accessed 23 Dez 2022
13. Schonlau, M.: *Computer Experiments and Global Optimization*. PhD thesis. University of Waterloo (1997)
14. Jones, D.R., Schonlau, M., Welch, W.J.: Efficient global optimization of expensive black-box functions. *J. Global Optim.* **13**(4), 455–492 (1998)
15. Mierlo, C. v., Burmberger, L., Daub, M., Duddeck, F., Faes, M.G.R., Moens, D.: Interval methods for lack-of-knowledge uncertainty in crash analysis. *Mech. Syst. Signal Process.* **168**, 108574 (2022)
16. Barzanoi, R., van Mierlo, C., Pabst, M., Boegle, C., Faes, M.G.R., Moens, D., Duddeck, F.: Evaluation of uncertain boundary conditions for analysis of structural components with respect to crashworthiness. In: Desmet, W., Pluymers, B., Moens, D., Neeckx, S. (eds.) *Proceedings of ISMA2022 International Conference on Noise and Vibration Engineering and USD2022 International Conference on Uncertainty in Structural Dynamics*. KU Leuven, Belgium, pp. 4812–4824. ISBN: 9789082893151 (2022)
17. Lin, Y.: *Optimization of vehicle components for crashworthiness*. Master’s thesis. Arcisstrasse 21, 80333. Technische Universität München, München (2022)
18. Desmet, W., Pluymers, B., Moens, D., Neeckx, S. (eds.): *Proceedings of ISMA2022 International Conference on Noise and Vibration Engineering and USD2022 International Conference on Uncertainty in Structural Dynamics*. KU Leuven, Belgium. ISBN: 9789082893151 (2022)

Author Index

A

Alber-Laukant, Bettina, [109](#)
Alsayed Ahmad, Moustafa, [120](#)
Ascia, Paolo, [134](#)

B

Blandl, Markus, [40](#)
Bletzinger, Kai-Uwe, [120](#)
Bold, Jens, [68](#)
Buchmann, Erhard, [1](#)
Buske, Magnus, [85](#)

C

Carosella, Stefan, [40](#)

D

de Albuquerque, Rodrigo, [51](#)
Dickhut, Tobias, [97](#)
Duddeck, Fabian, [134](#)

E

Ehrlich, Ingo, [15](#)
Erber, Maximilian, [109](#)

F

Fink, Frieder, [28](#)
Fuhr, Jan-Philipp, [28](#)

G

Gerster, Nico, [97](#)
Gude, Maik, [85](#)

H

Hartmann, Christoph, [109](#)
Höfer, Philipp, [1](#), [15](#), [68](#)
Hojjat, Majid, [120](#)
Holtmannspötter, Jens, [15](#)

Hübner, Fabian, [51](#)
Hüls, Alexander, [68](#)

J

Judenmann, Anna, [15](#)

K

Kliewe, Maike, [40](#)
Kolbe, Björn, [85](#)
Kopp, Fabian, [28](#)
Korte, Nikolas, [68](#)
Koshukow, Wikentij, [85](#)
Krischler, Ruben, [40](#)
Kupfer, Robert, [85](#)

L

Liebsch, Alexander, [85](#)
Lin, Ying, [134](#)
Luik, Marius, [51](#)

M

Mesarosch, Felix, [28](#)
Meschut, Gerson, [85](#)
Middendorf, Peter, [28](#), [40](#)
Musil, Bruno, [1](#), [68](#)

O

Ort, Sascha, [68](#)

P

Prestes, Isabel, [1](#)

R

Rosnitschek, Tobias, [109](#)
Ruckdäschel, Holger, [51](#)

S

Schlotthauer, Tristan, [28](#)
Schönl, Florian, [51](#)

T

Thomas, Jeremias, [51](#)
Tremmel, Stephan, [109](#)
Troschitz, Juliane, [85](#)

V

Volk, Wolfram, [109](#)

W

Westerhoff, Bernd, [68](#)
Wippermann, Jan, [85](#)